1. Introduction

Considerable research has been done on recent climate changes that have been observed over the Arctic and parts of the Antarctic (Serreze et al., 2000; Turner et al., 2006; Comiso, 2003; Polyakov et al., 2003 etc.). Observations over the past few decades indicate that temperatures over the Arctic and parts of the Antarctic have risen significantly (Comiso, 2003; Turner et al., 2006) and that cyclonic activity over the Arctic and seas near the Antarctic have also increased (Zhang et al., 2004; Fyfe, 2003). Furthermore, there has been a dramatic decrease in sea ice coverage over the Arctic and parts of the Antarctic (Lindsay and Zhang, 2005; Jacobs and Comiso, 1997) and changes in atmospheric circulation patterns over the Arctic and Antarctic, with shifts in the AO (Arctic Oscillation) and AAO (Antarctic Oscillation) to a more positive phase (Holland, 2003; Thompson and Solomon 2002). A major tool used to diagnose climate changes over the polar regions is the reanalysis products of NCEP/NCAR and ECMWF (ERA-40). These data have been shown to have reasonably accurate temperature fields(Uppala et al., 2005), however, it has been shown that the reanalyses have relatively significant errors in their wind fields over the polar regions (Francis, 2002) due to the paucity of wind observations over the Arctic and Antarctic. Due to the low number of radiosonde stations over the polar regions, the reanalysis wind fields are less accurate. Therefore, there needs to be a way to improve the wind fields over the polar regions.

Because polar orbiting satellites have been used to improve weather forecasts (Key et al., 2003), they could also be used to improve the reanalysis wind fields. For long term reanalyses, the Advanced Very High Resolution Radiometer (AVHRR) on board NOAA satellites would be suitable due to it's relatively long record going back to 1981, nearly 17 years longer than the Moderate Resolution Imaging Spectroradiometer (MODIS) dataset. Therefore, a dataset of AVHRR wind vectors over the polar regions was created, spanning more than 20 years (January 1982 to August 2002). Wind speed, direction, and height are estimated for the Arctic and Antarctic, poleward of approximately 60 degrees latitude, by tracking the movement of cloud features in the 11 μm window channel.

A detailed description of the methodology involved in producing this dataset will be discussed in Chapter IV. Also discussed are potential sources of error in the satellite-derived winds technique over the poles that could produce erroneous wind vectors. A statistical validation of the AVHRR winds is conducted in Chapter VI by first comparing them to the background field (ERA-40), and then through comparison with radiosonde winds (rawinsondes). In addition, a qualitative comparison to TIROS Operational Vertical Sounder (TOVS) winds will be shown. The AVHRR and ERA-40 winds are compared to rawinsondes not assimilated into the reanalysis to gauge the accuracy of the two products. Next, in Chapter VI a comparison of AVHRR versus ERA-40 winds over locations with and without radiosonde data is investigated.

The kinematic reasoning behind differences between ERA-40 and AVHRR is explored in Chapter VII. First, an investigation of where in the atmospheric flow do AVHRR winds occur most frequently will be shown. A few case studies in Chapter VII will be investigated to show where significant differences between the wind fields at synoptic to subsynoptic scales tend to occur. Next, a long term statistical comparison of the speed differences between ERA-40 and AVHRR in jet streams with wind speeds greater than 25 m/s is computed. A statistical comparison of speed and direction differences in kinematic flow types is then investigated in Chapter VII. Finally, the potential impacts of assimilating AVHRR winds into the reanalysis field of ERA-40 are discussed further in Chapters VII and VIII.

2. BACKGROUND

This chapter provides a brief history of estimating atmospheric motion from space. The technological development of Atmospheric Motion Vectors (AMV) is discussed. Next, due to the possible implication that this research may have on climate research over the polar regions during the last twenty years, an overview of observed climate change in the polar regions during the past few decades is discussed. The motivation for doing the AVHRR CMV archive and associated research is then discussed.

2-1. History

In the early 1960s, Tetsuya Fujita developed the first analysis techniques to use cloud pictures from the first TIROS polar orbiting satellite for estimating the velocity of tropospheric winds (Key et al., 2003). With the advent of geostationary remote sensing in 1966 it was shown that the animated satellite images had the potential to reveal atmospheric motions that would be useful in scientific research (Menzel, 2001). During the late 1960s Fujita used cloud motion analysis to investigate the formation and structure of atmospheric circulation on all scales (Menzel, 2001). Fujita further pursued an understanding of the relationship between cloud motions and the actual wind with a set of cloud truth experiments during most of his career (Menzel, 2001). The validation work of Fujita with careful analysis of mesoscale cloud motions from a combination of ATS-1 (Animated Time Series) and terrestrial photographs was able to confirm that atmospheric motions could be correctly determined from properly navigated geostationary images (Menzel, 2001). The development of Suomi's spin-scan camera and the work of Fujita led to the new field of inferring atmospheric motions from remotely based instruments that produced image sequences (Menzel, 2001). Additional research studies by Fujita provided independent measurements of cloud height and motion that could be used for validation of both satellite and rawinsonde wind data (Menzel, 2001). Furthermore, Fujita's research on cloud size and persistence led to the proper selection of targets and tracking for producing satellite winds (Menzel, 2001). Fujita's research experience in this field led to NASA (National Aeronautics and Space Administration) using his advice on sensor design characteristics that covered horizontal resolution, temporal resolution and radiance enhancement (Menzel, 2001).

Throughout the 1970s and early 1980s, cloud motion winds were produced from geostationary satellite data using a combination of automated and manual techniques (Menzel, 2001; Key et al., 2003). For example, Fujita and his staff at Chicago developed the Meteorologists Tracking Computer in the early 70s, which is an interactive computer system for manual gridding of the registered pictures and estimating atmospheric velocities from cloud displacements in a sequence of navigated and timed satellite images (Menzel, 2001). The evolution of ATS into the GOES (Geostationary Operational Environmental Satellites) made it possible to routinely track high resolution targets with infrared imagery (Menzel, 2001). The infrared (IR) imagery made it possible to produce winds overnight and to determine height assignments with the use of brightness temperatures. Winds derived from a sequence of infrared window images have been used to determine atmospheric circulation over regions that have limited ground-based data (i.e., radiosonde data), particularly over the oceans. In 1989 J. Turner and D.E. Warren from the British Antarctic Survey developed manual and automatic techniques for deriving Infrared (IR) cloud track winds in the polar regions from sequences of AVHRR (Advanced Very High Resolution Radiometer) images from the polar orbiting TIROS-N series of satellites (Turner and Warren, 1989). The AVHRR was launched into Low Earth Orbit (LEO) on board the TIROS-N and was on subsequent polar orbiting NOAA class satellites in the 1980s, 90s and 2000s.

During the late 1970s Cloud Motions Wind Vectors (CMV) from IR were generated daily to assist the study of global atmospheric circulations (Menzel, 2001). With the advent of water vapor (WV) images in 1979, it became possible to use these images to derive upper-level atmospheric motion vectors in cloud free regions, and in 1996 water vapor motion vectors became fully operational with the use of geostationary satellite WV imagery. In 1992, the National Oceanic and Atmospheric Administration (NOAA) began using an automated winds software package developed at the University of Wisconsin Space Science and Engineering Center that made it possible to produce a full-disk wind set without manual intervention (Menzel, 2001; Key et al., 2003). By 1998, the National Environmental Satellite, Data, and Information Service (NESDIS) operational GOES AMV production increased to every 3 hours with spatial density vectors derived from visible, infrared and water vapor images (Menzel, 2001). By the beginning of the 21st century, GOES derived wind vectors became routinely used in operational numerical models of the National Centers for Environmental Prediction (NCEP), European Center of Medium-Range Weather Forecasting (ECMWF) and Japanese Meteorological Agency (JMA). However, this left a gap in the observing system over the polar regions. This led to the use of polar orbiting satellites, such as the Moderate Resolution Imaging Spectroradiometer (MODIS) on board the Terra and Aqua satellites and the Advanced Very High Resolution Radiometer (AVHRR) on board the NOAA satellites to derive winds in the polar regions to fill the gaps. Currently, ECMWF and NCEP use MODIS-derived wind vectors in the polar regions for operational numerical models. Model impact studies have shown that the inclusion of satellite derived winds from MODIS in the polar regions have had positive model impacts by increasing the anomaly correlations of the 5-day forecasts[1] (Key et al., 2003).

2-2. Climate Change

Many recent studies have shown that the Arctic climate has changed significantly over the past 25 years (Polyakov et al., 2003; Lindsay and Zhang, 2005; Overpeck et al., 1997; Overland et al., 2002; Rigor et al., 2000; Rigor et al., 2002; Serreze et al., 2000; Comiso, 2003). For example, over the Arctic Ocean there has been a noticeable decrease in sea-ice concentration (Parkinson and Cavalieri, 2002; Lindsay and Zhang, 2005; Serreze et al., 2000; Deser et al., 2000; Belchansky et al., 2004; Zhang et al., 2004; Rigor et al., 2002; Comiso, 2002). The National Snow and Ice Data Center reported that a new record was established in September 2005 for the lowest Arctic sea ice extent since satellite monitoring began in the late 1970s. In addition to the Arctic, the atmosphere of the Southern Hemisphere high latitudes has undergone pronounced changes over the past few decades (Thompson and Solomon, 2002; Vaughan et al., 2001). A study of tropospheric temperature trends over the Antarctic done by the British Antarctic Survey using 30 years of radiosonde data indicated a

---

1 Figures 8 and 9 in “Cloud-Drift and Water Vapor Winds in the Polar Regions From MODIS” Key etc. 2003. IEEE Transactions on Geoscience and Remote Sensing.

significant warming trend that is greatest at mid-levels (around 500 hPa) during the Austral winter (Turner et al., 2006). Additional studies indicate that the greatest surface warming trends over the Antarctic have been observed over the Peninsula (Thompson and Solomon, 2002; Vaughan et al., 2001).

Over the Antarctic there has been observed decreases in the extent of sea ice in the Amundsen and Bellingshausen Seas (Figure 1) that is the result of changing surface wind stresses (Jacobs and Comiso, 1997). The changing wind stresses over the Amundsen and Bellingshausen Seas have become more poleward and westerly, that has been a result of increased positive polarity of the SAM (Southern hemisphere Annular Mode) or AAO (Antarctic Oscillation), where anomalously strong north westerlies over the Antarctic Peninsula and Amundsen-Bellingshausen Seas should act to decrease the incidence of cold air outbreaks from the south and lead to overall greater warm air advection from the Southern Ocean that has caused the melting of sea ice over the region (Thompson and Solomon, 2002; Jacobs and Comiso, 1997). Changes in these properties are a function of large-scale circulation patterns that affect surface-atmosphere interactions and feedback mechanisms. For example, between 1989 and 2001 there has been a dramatic shift in the Arctic Oscillation (AO), from negative to positive phase resulting in a prevailing low-pressure systems over the Arctic that has promoted the decrease and thinning of sea ice concentration by changing the surface wind stresses (Rigor et al., 2002; Serreze et al., 2000; Belchansky et al., 2004; Polyakov et al., 2003; Lindsay and Zhang, 2005). The AO (AAO) is characterized as an exchange of atmospheric mass between the Arctic (Antarctic) and the mid-latitudes around

45° N (45º S) that results in differing geopotential height field anomalies between the poles and the mid-latitudes (Rigor et al., 2002; Thompson and Solomon, 2002). The positive phase is associated with lower than normal sea-level pressures and geopotential heights over the Arctic Ocean (Antarctic) and the negative phase is associated with higher than normal sea-level pressures and geopotential heights over the Arctic (Antarctic) Ocean (Thompson and Solomon 2002; Walsh et al., 1996; Deser et al., 2000; Belchansky et al., 2004). The positive phase shift in AO (AAO) has been associated with a lowering of atmospheric pressures, or increase in the cyclonic activity, and a poleward shift of the storm tracks into the Arctic and Southern Oceans surrounding the Antarctic (Rigor et al., 2002; Walsh et al., 1996; Deser et al., 2000; Fyfe, 2003; Belchansky et al., 2004; Zhang et al., 2004, Polyakov et al., 2003). The cyclonic activity has resulted in an increased amount of sea ice being exported out of the eastern and central Arctic out of the Fram Strait into the North Atlantic. The cyclonic activity increases Ekman transport of sea-ice mass. Sea-ice is transported to the right of the geostrophic wind stress with a speed about 1% of and 5º to the right of the geostrophic wind (Rigor et al., 2002) in the Northern Hemisphere. In addition, the increased cyclonic activity over the eastern Arctic has moved the Transpolar Drift Stream farther to the west, where it is over the central Arctic Ocean and has increased the amount sea ice being transported out of the interior Arctic Ocean (Rigor et al., 2002, Lindsay and Zhang, 2005). Moreover, there has been a significantly longer melt season, with earlier dates of first melting and later dates of first freezing of the sea ice that has been observed over the Arctic (Belchansky et al., 2004) Decrease in sea ice concentrations across the Arctic has resulted in a decreased surface albedo, increased solar absorption and an increase of heat fluxes from the surface, and as a result, there has been noticeable increases in surface temperatures across the Arctic (Rigor et al., 2000 and 2002; Serreze, 2000; Overland et al., 2002; Comiso, 2003; Polyakov et al., 2003). Changes in surface fluxes of heat, moisture and momentum can also affect the atmospheric circulation (Deser et al., 2000).

In addition to changes in surface temperature, atmospheric circulation and pressure, there have been observed decreases in cloud cover over the central Arctic during the winter and increased cloud cover during the summer (Wang and Key, 2003 and 2005). This has modulated the net surface radiative fluxes by decreasing the atmosphere to surface longwave forcing during the winter and decreasing the sky to surface shortwave forcing and increased longwave forcing during the summer (Wang and Key, 2003 and 2005). This has to a certain extent modified the positive feedbacks (i.e., decreased surface albedo, increased solar absorption, increased sensible and latent heat fluxes) that have led to the warming trends in the Arctic over the past few decades. Changes in the above properties are related to the large-scale atmospheric and oceanic circulation patterns that affect the surface and atmosphere interactions.

The 22 year dataset (1979-2001) of derived winds from TOVS (TIROS Operational Vertical Sounder) indicates trends in zonal and meridional wind components, and in the positioning of the polar vortex (Francis et al., 2005). The polar vortex has shifted toward northern Canada, offshore winds in the East Siberian Sea and Barents Sea have increased, with positive trends in the zonal wind component over Eurasia, but negative trends in the eastern Arctic Ocean (Francis et al., 2005). In addition, there has been increased southerly flow at 700 hPa that corresponds with decreased ice concentrations in the East Siberian and Barents Seas, and increased northerly flow occurs where ice has increased north of the Canadian Archipelago (Francis et al., 2005). Moreover, winter meridional winds have been moderately correlated to the winter North Atlantic Oscillation (NAO) index (Francis et al., 2005). The North Atlantic Oscillation (NAO) is the dominant mode of variability in the North Atlantic region and represents a redistribution of atmospheric mass between centers of action located near the Azores high and the Icelandic low (Holland, 2003). A positive phase NAO is associated with a higher than normal mean sea-level pressure (MSLP) over the Azores and a lower than normal MSLP over the vicinity of Iceland. A negative phase of the NAO is associated with lower than normal MSLP over the Azores and a higher than normal MSLP over the vicinity of Iceland. In addition, there is an observed close relation between the NAO and the AO, with the increased positive phases of AO closely linked with the increased positive phase of the NAO (Holland, 2003). NAO anomalies in the eastern (western) Arctic are positively (negatively) correlated, leading to an increase in sea ice concentration over the Canadian Archipelago and a decrease of sea ice over the Barents-Kara Seas with the current positive trend in the NAO index being observed (Francis et al., 2005; Deser et al., 2000).

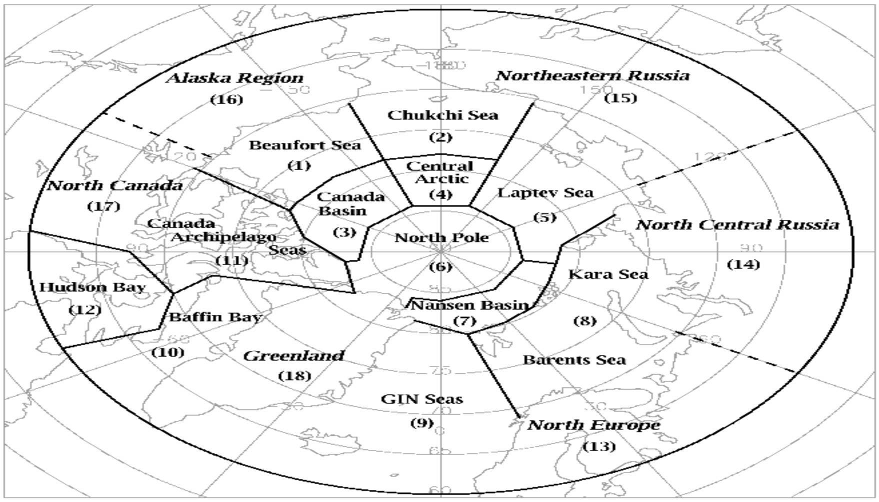

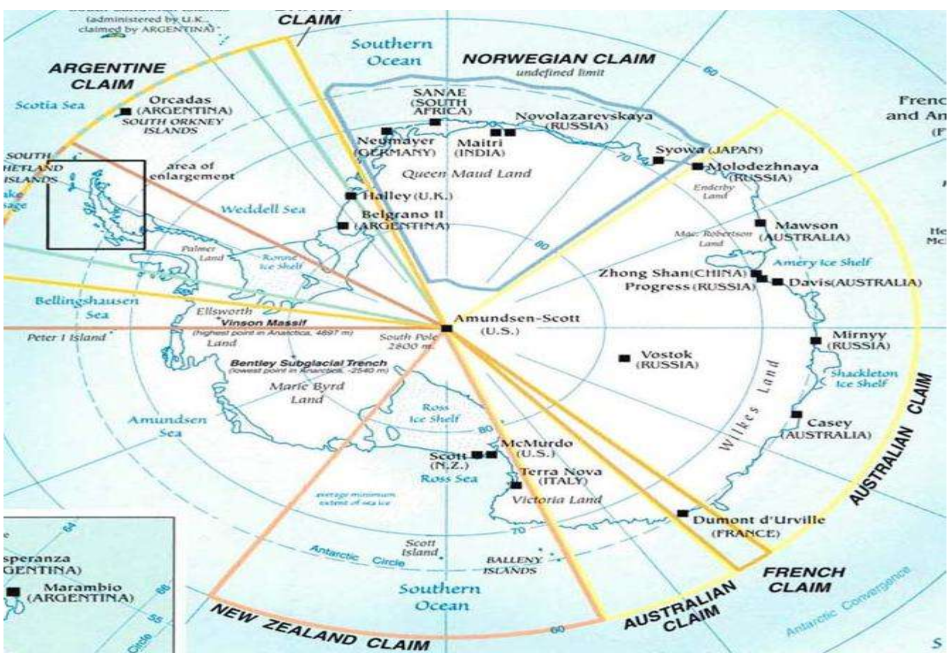

Figure 1. Top is a map of regions over the Arctic. Bottom is a map of the Antarctic Region.

2-3. Motivation

Previous studies have shown that there have been relatively large errors in the reanalysis wind fields over the Arctic where there is little or no radiosonde data available for assimilation. Francis (2002) examined differences between NCEP/NCAR (National Centers of Atmospheric Research) and ERA-40 (ECMWF Reanalysis of 40 years) reanalysis winds and RAOB (Radiosonde Observations) winds that were not assimilated in the reanalysis field, from the LeadEx (1992) and CEAREX (1988-89) experiments. It was found that both reanalyses (NCEP and ERA-40) exhibit large biases in zonal and meridional wind components, being too westerly and too northerly by 25-65% (Francis, 2002). It is not surprising that both NCEP/NCAR and ERA40 exhibit similar biases due to both reanalyses are assimilating the same rawinsonde data sets. These results have serious implications for using the reanalysis wind fields for Arctic climate research. Overly strong westerlies suggest that the magnitude of the meridional temperature gradients near the experiment sites are too high (Francis et al., 2005). The reanalysis fields could have overly intense, narrow jet streams and/or cyclonic disturbances and semi-permanent features in the upper-level circulation may be misplaced and the reanalysis may not properly capture the synoptic-scale feature that tend to cause these fluctuations. Importantly, poleward transport of energy and moisture by the reanalysis winds would be too small. Finally, models using these winds to calculate the surface fluxes or to force sea ice motions may produce patterns with unrealistic features (Francis et al., 2005).

A reason for the large errors in the reanalysis wind fields over the Arctic and

Antarctic is due to the sparse observing network of rawinsonde (winds from radiosonde) data (Figure 2). There are noticeable gaps in the observing network over the central Arctic (Arctic Ocean) and Greenland with a bias of observing stations toward the lower latitudes over the North American and Europe-Asian Continents. There is also a lack of observing stations over the Antarctic Continent and the surrounding oceans, where one would expect the same lack accuracy in the reanalysis wind field.

It has been shown that data assimilation of the MODIS winds (WV, and cloud-drift IR) have significantly improved forecasts of geopotential height over the Antarctic and therefore show that the reanalysis fields without satellite-derived winds assimilated into them suffer from the same lack of surface based observation stations (Key et al., 2003) . With a lack of observational data, numerical weather prediction model forecasts and climate reanalysis products become less accurate. Therefore, a more accurate upper-level wind field over the polar regions is needed. The inclusion of satellite-derived wind fields from polar orbiting satellites in the background analysis fields become a valuable data set to improve the above products. For the climate reanalysis fields, with recent studies that use the reanalysis fields showing the Arctic climate changing significantly over the past 20 years and regional changes over the Antarctic occurring over the same time, it becomes very important to improve any possible deficiencies in the reanalysis fields that are used for such climate studies. Furthermore, with the potential of improving wind reanalyses from the satellite-derived winds, there is a potential to improve future short-term climate studies on trends in regional atmospheric winds and circulation patterns over the polar regions.

With a gap in the observing systems over the polar regions that cannot be filled by geostationary satellites (i.e., Meteosat and GOES) because of poor viewing geometries and therefore poor spatial resolution that leads to large uncertainties in the derived wind vectors, polar orbiting satellites are needed. Polar orbiting satellites provide excellent spatial resolution of 1 km for MODIS on board Terra and Aqua satellites and 1.1 km for AVHRR NOAA TIROS-N (Television Infrared Observation) satellites at nadir over the polar regions, with MODIS having been shown to be useful for estimating high-latitude tropospheric winds (Key et al., 2003). Therefore, satellite-derived wind fields from polar orbiting satellites, such as MODIS on board Terra and Aqua and AVHRR Radiometer on board the NOAA TIROS-N based series are most valuable. In fact, ten numerical weather prediction centers worldwide have demonstrated that polar winds derived from MODIS have had a positive impact in improving global weather forecasts. In addition to the polar regions, satellite-derived winds (CMV and WVMV) from geostationary satellites and sea-surface winds from the Scanning Multichannel Microwave Radiometer (SMMR) and Special Sensor Microwave Imager (SSM/I) have had positive impacts on improving analysis and weather forecasts over data void oceanic regions of the globe (Atlas et al., 1996; Velden et al., 1997; Tomassini, 1999).

An attempt to improve the three-dimensional wind field in climate reanalysis products has been undertaken by Francis, Hunter and Zou (2005) with the use of satellite-derived temperature profiles from the TIROS Operational Vertical Sounder (TOVS) and using the thermal-wind relationship (equation 1).

$$\mathbf{V}_T = (g/f_o)\nabla[(RT_V/g)\ln(p_2/p_1)] \qquad (1)$$

This is done by retrieving temperature profiles from an inversion algorithm, taking the daily mean surface wind and pressure fields and using the relationship given by the thermal wind equation that uses the average temperature in a layer bounded by two pressure levels to calculate a thermal wind field. The surface wind field is needed to calculate the actual geostrophic wind at subsequent levels above the surface, and the mass conservation technique developed by Zou and Van Woert (2002) is used to force the first guess wind field to conserve mass in a vertical column of air in both the meridional and zonal directions. TOVS includes a microwave sounding unit that allows for satellite-derived temperature data to be taken through clouds. However, one problem with the TOVS winds is that it is not able to calculate winds over Greenland and that Greenland itself acted as a mass barrier below 700 hPa that probably had a significant negative impact on the mass conservation technique used for the zonal direction at lower levels (Francis et al., 2005). An additional problem was that in using the thermal wind relationship in calculating the actual wind field, the resultant wind field would be nearly geostrophic and not taken into account any significant ageostrophic motions in the flow (Zou and Van Woert, 2001).

In the real atmosphere flows are ageostrophic under certain conditions (friction, accelerations and decelerations of the flow), so the thermal wind product would be less accurate in regions of large ageostrophic flow, such as near the surface and entrance/exit regions of jet streaks and strongly curved flows. The geostrophic balance only occurs when there is no curvature in the flow (Holmlund, 1998). Taking the curvature into account, the gradient wind in a frictionless environment can be defined as in equation 2, where R_c is the radius of curvature, f is the Coriolis parameter (equation 2 where Ω is the angular velocity of rotation of the earth and Θ is the latitude) and $\partial\Phi/\partial n$ the local derivative of geopotential height (Holton, 1992).

$$V = -f_o R_c/2 \pm [(f_o^2 R_c^2)/4 - R_c(\partial\Phi/\partial n)]^{1/2} \quad (2)$$

In general, the gradient flow is a three-way balance between the Coriolis force (equation 3), the centrifugal force, and the horizontal pressure gradient force (Holmlund, 1998).

$$f_o = 2\Omega\sin\Theta \quad (3)$$

The ratio of the geostrophic and gradient flows is defined in equation 4 and the Rossby number is defined in equation 5 (Holton, 1992).

$$V_g/V = 1 + R_o \quad (4)$$

$$R_o = U/(f_o L) \quad (5)$$

In typical synoptic cases at 1000 km, 10 m/s and over the high latitudes, the geostrophic approximation deviates from the gradient wind by about 7% in speed. For example, in one case study done on March 2, 1979 off the coast of Baja California, it was found that the speed of the 300 hPa cross-height contour ageostrophic wind component in the left exit region of a jet streak in a highly curved flow around the back end of an amplified upper level trough of low pressure exceeded 20 m/s (Shapiro and Kennedy, 1981).

Another source of error in the geostrophic approximation is the neglecting of the acceleration term (dV/dt) in horizontal momentum equations (equations 6a and 6b).

$$Dv/Dt = -f_o u - 1/\rho(\partial P/\partial y) \quad (6a) \qquad Du/Dt = -f_o v - 1/\rho(\partial P/\partial x) \quad (6b)$$

This becomes a major factor in regions where the flow rapidly accelerates or decelerates, such as the entrance and exit regions of jet streams or in significantly curved flows with significant centripetal acceleration, such as the base of a trough of low pressure. However it should be expected that any deviations from the straight flow be within 10%-20% of the continuous straight flow (Holmlund, 1998). Moreover, the observed inaccuracies of the reanalysis wind fields are expected to occur in regions of ageostrophic flow and the satellite-derived thermal wind field would not improve the reanalysis deficiencies in those regions. However, when compared to rawinsonde data not assimilated into the reanalysis field, the v-component of the satellite-derived thermal winds from TOVS did produce biases that were only 10% of the normalized wind speed, while the NCEP-NCAR and ECMWF reanalyses v-component of the winds exhibited biases that were over half of the normalized wind speed (Frances et al., 2005). Above 600 hPa the zonal or u-component of TOVS winds had smaller biases than NCEP-NCAR zonal wind components. However, below 600 hPa the TOVS thermal u-component wind biases were larger than NCEP-NCAR reanalysis. The reason for this was the effects of Greenland as a zonal barrier in the mass-conservation correction scheme (Frances et al., 2005).

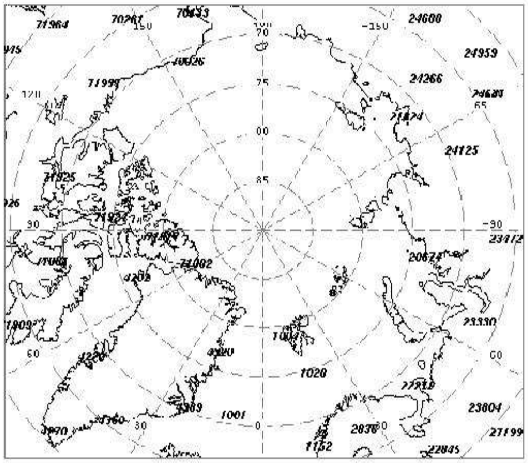

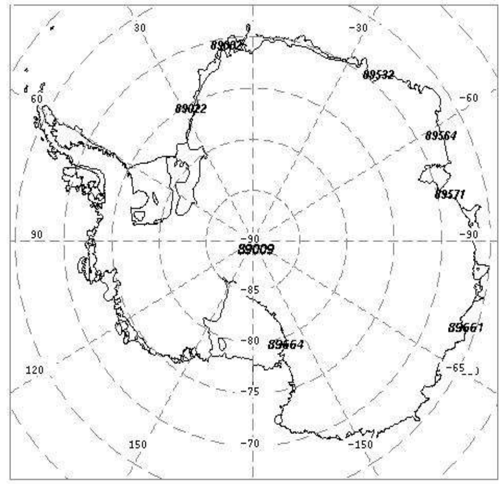

Figure 2. Rawinsonde observing network over the Arctic(left), and over the Antarctic(right).

Unlike AVHRR, MODIS has a water vapor channel, and therefore produces many more wind vectors at mid and upper levels over the Arctic and the Antarctic than AVHRR, given that the majority of water vapor features are from mid and upper levels in the troposphere. Therefore, MODIS is more useful in improving the analysis fields in the numerical models. However, MODIS data goes back to only 1998, while AVHRR data goes back to 1978 (Table 1). The longer data set of the AVHRR NOAA satellite data makes it more useful in improving any possible deficiencies in the climate reanalysis fields of the ECMWF and NCEP reanalyses. Therefore, a polar wind data set spanning more than 20 years has been generated using the AVHRR Global Area Coverage (GAC) data from NOAA satellites. Wind speed, direction, and height are estimated for the Arctic and Antarctic, poleward of approximately 65 degrees latitude, by tracking the movement of cloud features in the 11 ųm infrared window channel. Overall, the goal of this research is to demonstrate how AVHRR data will improve future reanalysis wind field products with the inclusions of derived wind vectors from AVHRR. This has the potential to lead to improved wind reanalysis products and future climate research on atmospheric circulation trends in the polar regions.

3. DATA

The Datasets used in this research project are the Advanced Very High Resolution Radiometer (AVHRR), the 40-year reanalysis from ECMWF (ERA-40), the Integrated Global Radiosonde Archive (IGRA) and rawinsonde observations from the Arctic Leads Dynamic Experiment (LeadEx) and the Coordinated Eastern Arctic Experiment (CEAREX). An overview of each dataset product is given with some details on the development and quality of the data products used.

3-1. AVHRR and the Development of Cloud-Drift Winds

The AVHRR on board the NOAA polar orbiting satellites makes 14 orbits per day over the Arctic and Antarctic. In total AVHRR has 6 channels that include one visible, two near IR, and three thermal IR channels (Table 2). The entire AVHRR dataset covers the years 1978 (NOAA-5) through the present (NOAA-18) and is summarized in Table 1. The AVHRR historical winds dataset goes from January 1, 1982 to August 31, 2002. The winds dataset does not include the years before 1982 because of either navigation and calibration problems or AVHRR data was not available from SAA (Satellite Active Archive) and does not include wind data after August 31, 2002 becuase there was no ERA-40 (background used in the AVHRR winds derivation) data produced after this date. Even though AVHRR has a visible channel, it is not useful to apply this channel for winds derivations in polar regions, because of the long winter darkness and low sun angles during the summer that make it difficult to track targets in the visible channel over the polar regions. With the monthly average cloud amounts over the Arctic and Antarctic ranging from 50% to 90%, with an annual mean cloud coverage that is about 70% over the Arctic (Wang and Key et al., 2005) potential cloud targets are numerous (Key et al., 2003). The orbital period is about 101 minutes with the highest frequency of coverage over the poles (Figure 3), which allows for cloud targets to be tracked and wind vectors to be calculated above about 70º North and South latitudes. At 60º latitude, there are two overpasses of a single satellite separated by about ten hours. In order to accurately derive a wind vector for quality control purposes, three overpasses are needed and a target cannot be tracked for an inordinate amount of time.

The first attempt at cloud track winds from AVHRR over the polar regions began with Turner and Warner (1989), when the registration and re-mapping of the imagery with variations in viewing angles between polar orbiting overpasses became possible. The varying viewing angles is caused by the rotation of Earth between passes (Turner and Warren, 1989). By using three consecutive re-mapped AVHRR channel 4 (11 μm) IR images onto a polar stereographic projection, and tracking cloud features in a sequence of the three images in time consecutive order made it possible to derive wind vectors from a manual and automatic schemes. The manual approach uses a experienced operator to track cloud elements on an IR image display system and assigns the winds to particular levels using the cloud-top temperature and available in-situ data (Turner and Warren, 1989). If no nearby in-situ data is available, the user uses climatological data to determine the pressure height of the calculated vectors. Next, for quality control purposes, the two vectors calculate are checked for consistency, and if found to be consistent, an average wind vector is calculated that is centered at the middle image (Turner and Warren, 1989). The problem with the manual technique is that is labor intensive and time consuming, and is subjective when it comes to tracking the target and determining the consistency quality of the vector. The manual technique does not allow for routine production of wind vectors for assimilation into analysis fields of forecast models or climatological reanalysis.

The automatic scheme used by Turner and Warner (1989) used quality control that was carried out by computer that selects a pixel segment (7 X 7 pixels) that has a standard deviation greater than or equal to 0.3 K. A cross-correlation technique is used to track the segment in the subsequent images. The first segment with a correlation above a selected threshold which has a clear drop in correlation values in the surrounding 3 by 3 pixel box and has a maximum difference less than 5º K is selected (Turner and Warner, 1989). If a target segment is found and is tracked for three images, two vectors are calculated for the first to second image and the second to third image in the triplet loop to check for consistency and to determine quality of the vectors (Turner and Warner, 1989). Once the vectors pass a quality control, with wind speed differences less than 50 percent and wind directions within 30°, the pressure height of the wind vectors are determined. The height determination is done by a best fit with a climatological profile or a nearby radiosonde (Turner and Warner, 1989). The automatic scheme proved to be much more successful than the manual technique at tracking textural features on top of cloud sheets (Turner and Warner, 1989) . However, the automatic technique had a noticeable negative speed bias when compared to manual technique and the model analysis fields, which are unreliable themselves due the lack of radiosonde data over the Antarctic (Turner and Warner, 1989).

Even though Turner and Warner were able to calculate wind vectors over the polar regions with the use of AVHRR, they were not able to validate the data. Later, cloud drift wind vectors calculated from AVHRR over the Arctic were found to be comparable to gradient winds from High-Resolution Infrared Sounder (HIRS), with a RMS (root mean squared) difference less than 5 m/s (Herman and Nagle, 1994). When compared to rawinsondes the RMS difference of the AVHRR winds were found to be 6 m/s (Herman, 1994).

Since the automatic technique developed by Turner and Wallace in 1989 there have numerous advances in the cloud motion wind derivation procedures. In 1992, NOAA began using an automated winds software package developed at the University of Wisconsin at Madison, Space Science Engineering Center that made it possible to produce a full-disk wind set without manual intervention. A satellite-derived wind algorithm developed at the the Cooperative Institute of Meteorological Satellite Studies (CIMSS) called Windco was able to automatically calculate wind vectors from three consecutive geostationary satellite images. This was done by taking the consecutive triplet of satellite images and background analysis Gridded Binary (GRIB) fields of temperature, wind, dewpoint, mean sea level pressure, and 1000 hPa geopotential height, and sending them through multiple subroutines. These subroutines identified cloud or water vapor features (targets), tracked them and calculated the associated wind vectors, and assigned pressure heights. The Windco software package would be used in this research project to calculate wind vectors over the polar regions north (south) of 60° N (60° S) latitudes.

Table 1. Letter code, number, ID and dates of operational use of the NOAA satellites with the AVHRR instrument aboard.

Code	NUM	ID	Operational
TN	5	1	1978-06-11 to 1980-11-01
A	6	3	1979-07-17 to 1986-07-09
C	7	7	1981-06-24 to 1985-10-07
E	8	13	1981-06-24 to 1985-01-08
F	9	11	1984-12-17 to 1995-01-19
G	10	15	1986-10-08 to 1994-10-06
H	11	1	1988-10-21 to 1994-09-15
D	12	9	1991-07-16
J	14	5	1995-01-19
K	15	7	1998-05-13 to 2000-07-10
L	16	3	2000-09-21
M	17	11	2002-06-24
N	18	13	2005-05-20

Table 2. Channels, Wavelengths and uses of the AVHRR channels. Entry taken from: Rao, P.K., S.J. Holmes, R.K. Anderson, J.S. Winston, P.E. Lehr, Weather Satellites: Systems, Data, and Environmental Applications, American Meteorological Society, Boston, 1990. ISBN 0-933876-66-1

Channel	Wavelength(microns)	Primary Use
1	0.58 - 0.68	Daytime cloud/surface mapping
2	0.725 - 1.10	Surface water delineation, ice and snow melt
3A	1.58 - 1.64	Snow / ice discrimination (NOAA K,L,M)
3 (or 3B)	3.55 - 3.93	Sea surface temperature, nighttime cloud mapping
4	10.30 - 11.30	Sea surface temperature, day and night cloud mapping
5	11.50 - 12.50	Sea surface temperature, day and night cloud mapping

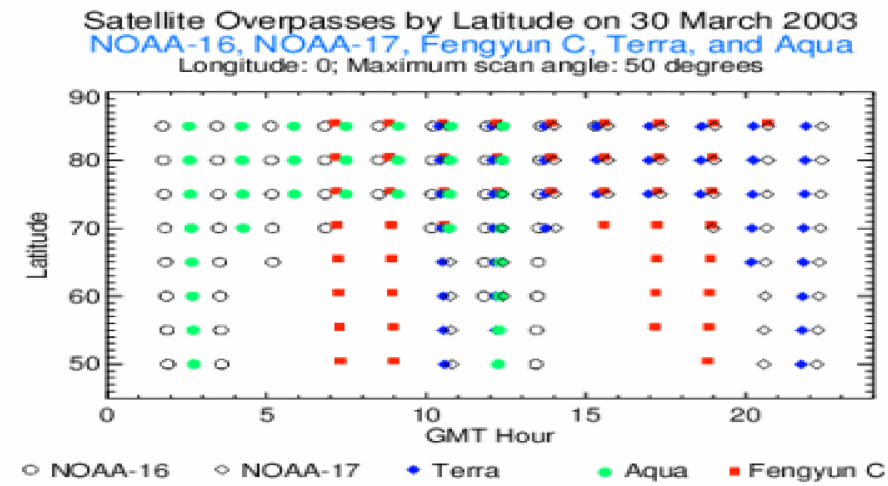

Figure 3. The figure above shows the times of successive overpasses at a given latitude-longitude point on a single day with a sampling of five satellites. Black/White dots are for AVHRR NOAA satellites.

3-2. Overview of the ERA-40

The ERA-40 is a re-analysis of meteorological observations from September 1957 to August 2002 produced by the ECMWF in collaboration with other institutions, including NCEP and NCAR (Uppala et al., 2005). The data assimilation uses analysis steps that are usually 6 hours, and combines observations over the period with background information to produce an estimate of the state of the atmosphere at a specific time (Uppala et al., 2005). The assimilating model used for the ERA-40 has a reduced Gaussian grid with uniform spacing of 125 km and 60-level vertical resolution (Uppala et al., 2005). The background information used in the re-analysis that was required for each analysis time is a short-term forecast out to 9 hours ahead of the initialization (Uppala et al., 2005). The forecasts were initialized from the most recent previous analysis and a spectral T159 model resolution and time step of 30 minutes was used to run the forecasts (Uppala et al., 2005). The background forecasts and observations are combined by statistically minimizing their errors in a 3D-variational assimilation scheme (Uppala et al., 2005). A problem for 3D-Var is that it does not treat differences between observations and analysis time as consistently as 4D-Var (Uppala et al., 2005). However, due to the significant computational costs of 4D-Var, the ECMWF decided to use 3D-Var instead (Uppala et al., 2005). Moreover, the observations and background forecasts are combined by minimizing the sum of error-weighted measures of the deviations of analyzed values from the observed and background values (Uppala et al., 2005). The background forecasts carry forward in time the observations used in the previous assimilation cycles (Uppala et al., 2005). In addition, the background fields instead of radiosonde measurements were used as predictors of air-mass-dependent biases (Uppala et al., 2005).

Upper-air wind observations in the ERA-40 come from radiosondes, dropsondes, pilot balloons, profilers, aircraft and tracking features (cloud and water vapor) from geostationary satellites (Uppala et al., 2005). It is important to note that there are no geostationary satellite derived winds over the polar regions, and that winds over the polar regions from low earth orbiting satellites are not assimilated into the re-analysis. The accuracy of radiosonde observations improved over the period; however, the geographical and temporal coverage has declined since 1979 (Uppala et al., 2005). To compensate for the decline of radiosonde observations since 1979, there has been an increase in the use of satellite observations[2], such

2 Table 1 in "The ERA-40 re-analysis" Uppala etc. 2005. Quarterly Journal of the Royal Meteorological Society.

as AMVs from geostationary satellites and the assimilation of raw radiances from VTPR, HIRS, MSU SSU and AMSU-A instruments that were used in constructing temperature fields (Uppala et al., 2005). The satellite observations can have significant impact on the performance of the re-analysis. Observations are rejected by the re-analysis if they differ significantly from the background forecast (Uppala et al., 2005).

It has been observed that there has been a marked improvement in the observing system over the past four decades (Uppala et al., 2005). This is indicated by significant reduction over time in the general magnitude of analysis increments[3] (Uppala et al., 2005). The analysis increment is the magnitude of the analysis minus background difference, and is a measure of the extent to which the background forecast is changed by the observations assimilated at a particular analysis time (Uppala et al., 2005). This means that observations influence the assimilation more through relatively small adjustments that provide better background forecasts for subsequent analyses (Uppala et al., 2005). Furthermore, improvements in the re-analysis are a result of better data assimilation from both improved forecast models and analysis components, such as 3D-Var instead of optimal interpolation used in the ERA-15 (Uppala et al., 2005). Improvement in data assimilation allows for more information to be extracted from observations. In addition, it has been found that ERA-40 analysis increments and background forecast RMS differences to radiosonde data are smaller in ERA-40 than the previous ERA-15 product[4]. It is also important to note the improvement

3 Figure 11 in "The ERA-40 re-analysis" Uppala etc. 2005. Quarterly Journal of the Royal Meteorological Society.
4 Figure 13 in "The ERA-40 re-analysis" Uppala etc. 2005. Quarterly Journal of the Royal Meteorological Society.

of the ERA-40 analyses used in medium-range forecast accuracy over the operational forecasts before the late 1990s, especially over the Southern Hemisphere[5]. The reason for the dramatic improvement over the Southern Hemisphere is the inclusion of much better satellite, aircraft and buoy data (Uppala et al., 2005). The operational forecast outperforms the ERA-40 in the late 1990s and afterwards due to the advent of 4D-Var assimilation in operational forecasts. Overall, the ERA-40 is an improvement over the ERA-15 product and produces fairly accurate medium-range forecasts. However, any deficiencies in the analysis method or assimilating model could introduce significant biases in the resulting analyses and invalidate conclusions drawn from them (Uppala et al., 2005).

Biases in the wind field are observed over the Arctic by Francis (2002) in which the ERA-40 winds were observed to have a positive speed bias and northerly direction bias. The successful modeling of the evolving state of the atmosphere depends on the utilization of observations, dynamics and physics of the background forecast model or any dynamical or physical relationships built into the error statistics (Uppala et al., 2005). The degree of dependence on the model varies with density and relative accuracy of the observations, and in general can vary from place to place, and from one variable to another (Uppala et al., 2005). Some deficiencies in the model dynamics or physics, background or observation error statistics, interactions between the forecast background and observations in the assimilation, and bad observations assimilated into the re-analysis could lead to the biases observed by Francis (2002) in the ERA-40 Arctic winds.

5 Figure 14 in "The ERA-40 re-analysis" Uppala etc. 2005. Quaterly Journal of the Royal Meteorological Society.

3-3. Integrated Global Radiosonde Archive

The radiosonde winds used for validation come from the Integrated Global Radiosonde Archive (IGRA). The IGRA dataset is quality controlled, with assurances that the wind vectors have plausible values of wind speed (0 to 150 m/s) and direction (0 to 360 degrees), dates and times of the observation are correct, without vertical value repetition runs, that the geopotential height values are within a certain number of standard deviations from their respective long term mean (climatology check), that a station has at least 100 soundings, and within the sounding the wind speed and direction must always appear together (Durre et al., 2006). It was found that the IGRA dataset had radiosonde observations in their archive that are not included in the ERA-40 radiosonde observations archive (Haimberger, 1995). Therefore, not all radiosonde observations in the IGRA dataset are assimilated into the ERA-40 reanalysis, because the IGRA had a more expansive radiosonde dataset that became available after the development of the ERA-40 reanalysis and that ERA-40 had a more stringent quality control testing of radiosonde observations than IGRA. It has been noted by Kitchen (1989) that radiosonde wind speeds are of good quality with total radiosonde error between about 0.9 m/s at 900 hPa to about 2.1 m/s at 100 hPa, and that mean directional differences of radiosondes are about 1 degree (Schmetz et al., 1993). However, beyond a distance separation of 52 km from the observation, the vector RMS is about 2.5 m/s at 850 hPa and 4 m/s at 300 hPa, while at a time separation from 2 hours of the observation, the vector RMS is about 2.2 m/s at 850 hPa and 5.1 m/s at 300 hPa (Kitchen, 1989). Furthermore, winds from aircraft can also be used for validation, but due to the lack of aircraft wind observations over the polar regions, only radiosonde winds observations are used as verification.

3-4. LeadEx and CEAREX

The Coordinated Eastern Arctic Experiment (CEAREX) was a multinational field project that occurred northeast of Spitsbergen, Norway off the coast of Svalbaard from September 1988 to May 1989. During the project, bathymetry, biophysical, hydrography, meteorological (including rawinsonde data), noise, sample position, and sea ice data were collected on a multi-platform ship Polarbjorn as it drifted southward from within the pack ice, east of Svalbard, and ultimately into open water (Francis, 2002).

The Arctic Leads Dynamic Experiment (LeadEx) was a field experiment that occurred in the Beaufort Sea at a camp on the pack ice approximately 270 km north of Prudhoe Bay, Alaska (Francis, 2002). The purpose of the experiment was to determine the impact of leads – linear fractures in the sea ice - on local meteorology and climatology, such as contributions to the atmospheric heat fluxes. During the LeadEx experiment rawinsondes were launched from the camp site from March 19th to April 22nd 1992 (Francis, 2002).

CEAREX and LeadEx (Figure 4) combine to provide 9 months of rawinsonde data that is used for validation of AVHRR versus ERA-40. Rawinsondes in CEAREX were launched from Polarbjorn using a VIZ Corporation system (Francis, 2002). Rawinsondes from LeadEx were launched used a Marwin Mini-Rawin System (Francis, 2002). Winds from both experiments were measured using Omega tracking, whose accuracies are approximately 4 m/s for a single wind value (Francis, 2002).

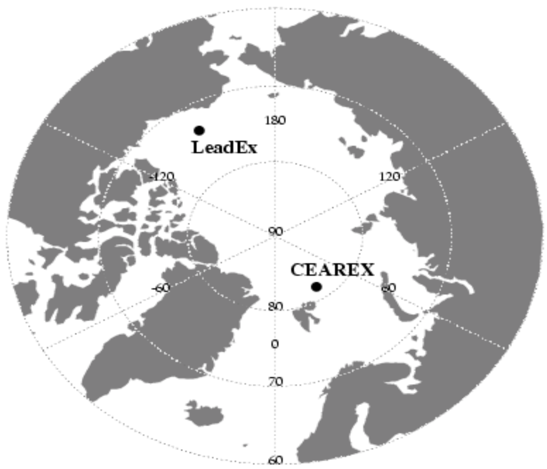

Figure 4: General locations of LeadEX and CEAREX experiment sites.

4. Methodology

In this section the procedures involved into producing AVHRR CMVs will be discussed. Included is an overview of the target selection, tracking and height determination processes, and a discussion of the preprocessing and post-processing involved. The post-processing includes the formation of quality indicators, recursive filtering, and speed, direction and height adjustments of the wind vectors.

4-1. Preprocessing

The Windco software package consists of multiple subroutines that determine potential targets, determine the pressure height of the target, track the targets, calculate wind vectors and determine a quality indicators (Figure 5). However, before the data is sent through the multiple subroutines to calculate wind vectors, there are a number of pre-processing steps. First, background climate re-analysis in gridded binary format (GRIB) from 1981 through 2002 were acquired from the European Center for Medium Range Weather Forecasts (ECMWF). The GRIB files include 13 pressure levels of temperature (surface, 1000, 850, 700, 500, 400, 300, 250, 200, 150, 100, 70 and 50 hPa), 6 pressure levels of relative humidity (1000, 850, 700, 500, 400, 300), 10 pressure levels of the u and v components of the wind (1000, 850, 700, 500, 400, 300, 250, 200, 150, 100), the mean sea level pressure, and 1000 hPa geopotential heights. These were interpolated from the standard 2.5 degree format to a 1 degree format for use in Windco. In addition, Windco does not accept relative humidity GRIB data, and therefore the relative humidity was converted into dewpoint depression with the use of the temperature GRIB data at the same level and time.

Second, AVHRR Global Area Coverage (GAC) satellite files from NOAA's Satellite Active Archive (SAA) and Comprehensive Large Array-data Stewardship System (CLASS) were used in this project. These files contained a visible, three near IR and two thermal IR channels. In addition, scanning times, satellite and solar zenith angle information were included in these files.

For the purpose of this project only the channel 4 (10.30 to 11.30 μm) and time files were used. The channel 4 datasets were calibrated into flat binary files (2 bytes per pixel) from software provided by CCAR (Colorado Center for Astrodynamics Research) and navigated into a stereographic projection at a 4 kilometer resolution. The channel 4, or clear-window Infrared channel data in stereographic projection was converted into MCIDAS (Man-computer interactive Data Access System) AREA format files, so that it could be read in by Windco. The resultant images are 1600 by 1600 pixels in size mapped onto a polar stereographic projection.

4-2. Targeting and Wind Vector Determination

The first subroutine is the targeting initial height assignment routine, that obtains inputs, such as the consecutive triplets of satellite images and associated background GRIB analysis fields. The routine next reads in data from a predetermined sized search box (11 X 11 pixels for AVHRR) in the first satellite image in the triplet, then locates any potential targets in the search box. This is done by calculating local gradients (around a single pixel with the lowest brightness temperature) in the search box and determining whether there are any gradients that exceed a specific threshold (7° K the default value used for AVHRR).

Next, the routine determines whether there are any search errors; if there are, it reads in the next search box. If there aren't, it goes on to determine the height of the target.

To determine the pressure heights of the targets, the Infrared Window Channel (WIN) method was used. This method uses a singular satellite band, the clear window infrared channel to come up with the brightness temperature values and compares them to the temperature profiles given by the background analysis fields. Cloud heights are determined by interpolating the cloud temperature, which is an average value over a set number of pixels, to the interpolated analysis background field temperatures at certain location (Olander, 2001). However, problems can arise when the clouds are semitransparent, like cirrus clouds, that cause difficulties in estimations of the pressure level of clouds, because brightness temperatures are affected by an unknown cloud emissivity or the percentage of cloud versus clear sky. This can lead to positive biases in brightness temperature and assigned pressure heights that are too low in altitude and therefore an underestimation of the wind speed (Olander, 2001).

The second subroutine is the wind vector derivation routine that utilizes the inputs (satellite images, background fields, user inputs) to calculate the wind vector. The times between the consecutive images in the triplet is assumed to be the same. First, target locations are read and the scene is determined to be cloudy or clear. Next, guess positions of the target being tracked are calculated with the use of the background wind vectors near the position of the target to calculate displacements of the target over the 101 minute interval between overlapping images. Next, a search box is read in with a box size of 32 by 32 pixels around the guess position of the target being tracked. The target is then searched for in the box. This is done by a statistical analysis of both search boxes, determining the highest correlated point between the initial target location and the ensuing search box region (Olander, 2001). In detail, the tracking method searches for the minimum of the sum of squared radiance difference between the target location and the region inside the search box. The above steps are repeated between images two and three in the triplet to produce another sub-vector for quality control. The sub-vectors are then compared to each other and the background field to determine the initial quality of vectors. Thereafter, an average is computed between the sub-vectors to come up with a final wind vector that is assigned the time of the middle image of the sequence. Finally, acceleration checks are performed to determine the physical validity of the wind vector. If the wind vector is determined to be physically invalid, for example, the wind vector has a large acceleration or departures greatly from the background guess vector, it is given an error flag.

4-3. Post Processing

The next two subroutines are part of the rigorous post wind derivation processing. These processes are used in conjunction to produce the best possible quality satellite-derived wind field. The first post processing subroutine was developed at EUMETSAT (European Organization for the Exploration of Meteorological Satellites) in 1997. This first post processing subroutine provides a quality indicator of the wind vectors, and with accordance with the next post processing subroutine, the recursive filter, have been found to produce the best results for satellite-derived wind fields (Holmlund et al., 2001). This second post process, developed at CIMSS in 1993, is a recursive filter that acts as a quality control of the cloud motion vectors.

Initially, during the 1990s the wind vectors produced by NOAA/NESDIS (National Environmental Satellite, Data and Information Service) only used the Recursive Filter as a means of quality control, and EMETSAT only used their own quality control algorithm. Comparisons to rawinsondes supports that both the Recursive Filter (RF) and EUMETSAT 's quality control algorithm or QI are good indicators of vector quality. However, it was later found that the QI retains more winds in jet stream areas with large speed accelerations, while the RF retains more winds in regions of slower and higher curvature in the atmospheric flow (Holmlund et al., 2001). Therefore, there are winds that are accepted (rejected) by the QI and rejected (accepted) by the RF. In order to have wind fields that retains winds in regions of large acceleration and high curvature, it was appropriate to combine both techniques for a wind field of higher density and acceptable quality that would be beneficial to both EUMETSAT and NOAA/NESDIS. It was noted that for the low-level IR winds, the RF technique outperformed the QI scheme, because winds accepted by the RF technique had a NRMS (Normalized Root Mean Squared – lower values are indication of better quality) of 0.51 whereas the winds accepted by QI and rejected by RF had a NRMS 1.48 (Holmlund et al., 2001). It was determined that a combined scheme would be able to extract more winds, and the use of the QI as a prefilter of the raw wind field before submitting to the RF would be the appropriate steps in determining the best wind field for data assimilation (Holmlund et al., 2001). The reason for this is that the QI is used as a consistency check, and throws away any wind vectors in obvious error and retaining a field that is utilized by the RF to reassign wind vector heights that are closest to the background field. It was found that the combined quality control algorithm technique (RFFQ160) outperformed the RF-only and QI-only techniques in a forecast impact study done in the NORPEX (North Pacific Experiment) in 1998 on the ECMWF forecasted geopotential height fields over North America (Holmlund et al., 2001). This was the motivation for the use of the combined quality control algorithm technique in current satellite-derived wind algorithms, such as is used in the production of the AVHRR winds.

The third subroutine is the the automatic editing and quality control (QI routine), that analyzes the consistency of the wind vectors in time and space. The goal of Quality Control (QC) is to extract those vectors that display an accuracy similar to rawinsonde measurements and filter out vectors with gross errors (Holmlund, 1998). This routine acquires the wind vectors and checks to the see whether the vectors have an error flag. If the flag value is less than 100, the wind vector is compared to its nearest neighbor, and a quality index value is calculated. The quality index value is calculated by putting each vector through a set of tests (Holmlund, 1998). There are five tests that are functions that check for consistency of the wind field in direction, speed, time (sub-vectors derived between the two pairs of images) and consistency of the wind field in space (in a 100.0 hPa pressure range) over the image and in comparison to background field (Table 3, Holmlund, 1998). Each individual test is normalized by a simple hyperbolic tangent based function where a_i is an exponential factor given to each test and the result lies in a specific range (equation 7).

$$\Phi_i(x) = 1 - \{\tanh[f_i(x)]\}^{a_i} \quad (7)$$

The reason for the tangent based function is that the distributions of the individual test results applied in the quality control algorithm will be non-Gaussian, and in order to combine results from different consistency functions, the results have to be normalized into a specific range (Holmlund, 1998) . Next the normalized result from each test function $\Phi_i(x)$ are weighted w_i averaged to come up with a final Quality Index (QI) value (equation 8).

$$QI = (1/\Sigma w_i)\Sigma w_i \Phi_i(x) \quad (8)$$

The result of the normalization is a value that is in between zero and one, with values closest to one representing the best quality vectors, and values close to zero representing poor quality vectors. If it is determined that a wind vector has a gross error, it is thrown out. The quality control scheme does not only supply flags and QI, but also provides information on the reliability of the tracking and the accuracy of the height determination. Any gross errors in the derivation of the wind vectors is usually caused by correlation procedures in deriving the displacements, the determination of the height of the vectors or orographic effects (Holmlund, 97).

One importance of quality indicators is for the purposes of the end users, the numerical weather prediction (NWP) centers, such as NCEP, the CDC (Climate Data Center), ECMWF and the JMA (Japanese Meteorological Agency). The end user would use the QI for determining observational weights and error characteristics of the satellited-derived winds being assimilated into the reanalysis fields. For the purposes of this project, the calculated quality indexes are useful in the subsequent RF routine for filtering out vectors in obvious error (QI values of 0.6 and higher are included into the RF analysis) and to determine weights given to the observations in the three-dimensional objective analysis.

The fourth subroutine is the recursive filter analysis that uses the background fields, user inputs, and results from the QI to calculate a final quality flag value. The Recursive Filter (RF) analysis is based on the two staged, three-dimensional objective analysis from Hayden and Purser (1995). It is useful in editing the datasets before dissemination and also for quantifying the probable utility of the data (Hayden and Purser, 1995). The RF is suitable for datasets with large density of coverage with a high degree of spatial non-uniformity, as is typical of satellite-derived wind products (Hayden and Purser, 1995). The reason for this is that the RF has the ability to vary the local scalings, which give it flexibility in areas of inhomogeneous data (Hayden and Purser, 1995). First, initial height assignment fields are acquired and a successive approximation 3-D objective analysis is applied using the background analysis and satellite derived wind fields. The objective analysis method analyzes data quality in two ways: deviation from the background field and consistency with neighboring datasets (Hayden and Purser, 1995). The first pass employs only the former, while the second pass employs the latter. After applying certain biases (i.e., a factor of .08 is multiplied and added to cloud drift winds at and above 300 hPa) , an adjustment of the pressure altitudes of the wind vectors is made by minimizing a variational penalty function (Olander, 2001). In the penalty function below (equation 9), V is velocity, T is temperature, P is pressure, dd is direction, s is speed and F represents the relative weight applied to each of the quantities (Nieman et al., 1997). Subscripts i, j and k identify the three dimensional location and subscript m represents the closest satellite-derived wind measurement (Nieman et al., 1997). The maximum permitted value of the penalty function is given by equation 10 (Olander, 2001). The value of M_v is a default gross error limit weighting factor for the velocity. After the vector is reassigned to a new pressure height and location that agrees closest to the background analysis field, a new quality flag is calculated called the RFI given by equation 12 (Olander, 2001). The final 3-D objective analysis is applied after height adjustments are applied to the targets. The final objective analysis checks for consistency between neighboring vectors and the fit of the observation to the analysis (Olander, 2001). Lastly, the final quality flag values (RFF) are calculated where vectors that do not obtain a final quality value exceeding an empirically defined threshold are flagged and rejected (Olander, 2001). For the AVHRR winds, the final quantity value was set to the default value of 0.5, and any wind vectors with a value below this value are flagged and rejected. The default value of 0.5 is determined by equation 13, with Q_k is the quality of the observation and W_k is the weight given at each grid point (Hayden and Purser, 1995).

$$B_{m,k} = ((V_m - V_{i,j,k})/F_v)^2 + ((T_m - T_{i,j,k})/F_t)^2 + ((P_m - P_{i,j,k})/F_P)^2 + ((dd_m - dd_{i,j,k})/F_{dd})^2 + ((s_m - s_{i,j,k})/F_s)^2 \quad (9)$$

$$B_{MAX} = 0.75S(M_V)^2 \quad (10) \qquad S = s/30 \quad (11) \qquad RFI = 1.0 - B_M/B_{MAX} \quad (12)$$

$$q_k = (Q_k W_k)^{1/2} \quad (13)$$

The importance of the final quality values is to indicate the quality of the satellite-derived winds when compared to the background field and compared to associated satellite-derived wind vectors in time and space. The final purpose is to assist end users in determining error characteristics and observational weights of the AVHRR winds.

Finally, there are multiple post-routines that modify any gross errors in the wind vector direction, speed or height assignments. First is a routine that modifies wind vectors in two cloud-deck scenes. High-level semitransparent cirrus clouds that were assigned mid-level heights are reassigned to a more reasonable height by checking the values of vectors closest to the vector in question, or “buddy” checking of vectors (Olander, 2001). Second, is a routine that does a gross-error check to flag low- to mid-level wind vectors that differ significantly from their corresponding background analysis vectors in speed and direction. For example, a wind vector greater than or equal to 11 m/s and greater than 8 m/s faster than the guess wind speed will be flagged as an error (Olander, 2001). Lastly, there is a routine to identify wind vectors within strong, high-level jet regions that differ significantly from background analysis wind field and flag them as errors.

In the validation of the AVHRR winds, the RMS (root mean squared) difference (equation 14) and normalized RMS (equation 17) will be used. It has been noted that the RMS difference (equation 14) value of the cloud drift winds compared reasonably to rawinsonde data, and exhibits a monotonic decrease in the RMS with an increase of the quality value indicator of the vector (Hayden and Purser, 1995, Table 4). As seen in Table 4 from Hayden and Purser (RF quality control technique), at the critical quality value between acceptance and rejection the cloud drift or motion vector RMS value is 6.6 m/s with the RMS value decreasing (increasing) with higher (lower) quality values of the wind vectors. Similar results were found with quality indicators calculated from the EUMETSAT AQC technique when compared to values for high-level IR cloud drift winds[6] (Holmlund, 1998). It was found that the QI values increased (decreased) monotonically with a decrease (increase) in the NRMS value (Holmlund, 1998) . However, the results for the mid-level IR winds were poor, with a non-monotonic increase (decrease) of QI with a decrease (increase) of NRMS[7] (Holmlund, 1998). The low-level IR winds showed a similar inconsistency in the NRMS versus QI values, with the inconsistency occurring in the QI region around 0.6[8] (Holmlund, 1998).

$$\text{RMS} = \text{sqrt(error/cases)} \quad (14)$$

$$\text{error} = \text{sum}[(\text{speed\_difference})^2] \quad (15)$$

$$\text{difference}=(\text{AVHRR\_quantity} - \text{Radiosonde\_quantity}) \quad (16)$$

$$\text{NRMS} = \text{RMS}/(\text{MEAN R/S}) \ ; \text{R/S} = \text{Wind Speed of Radiosonde} \quad (17)$$

6 Figure 9 in “The Utilization of Statistical Properties of Satellite-Derived Atmospheric Motion Vectors to Derive Quality Indicatiors”. Holmlund, 1998. Weather and Forecasting.
7 Figure 10 in “The Utilization of Statistical Properties of Satellite-Derived Atmospheric Motion Vectors to Derive Quality Indicatiors”. Holmlund, 1998. Weather and Forecasting.
8 Figure 11 in “The Utilization of Statistical Properties of Satellite-Derived Atmospheric Motion Vectors to Derive Quality Indicatiors”. Holmlund, 1998. Weather and Forecasting.

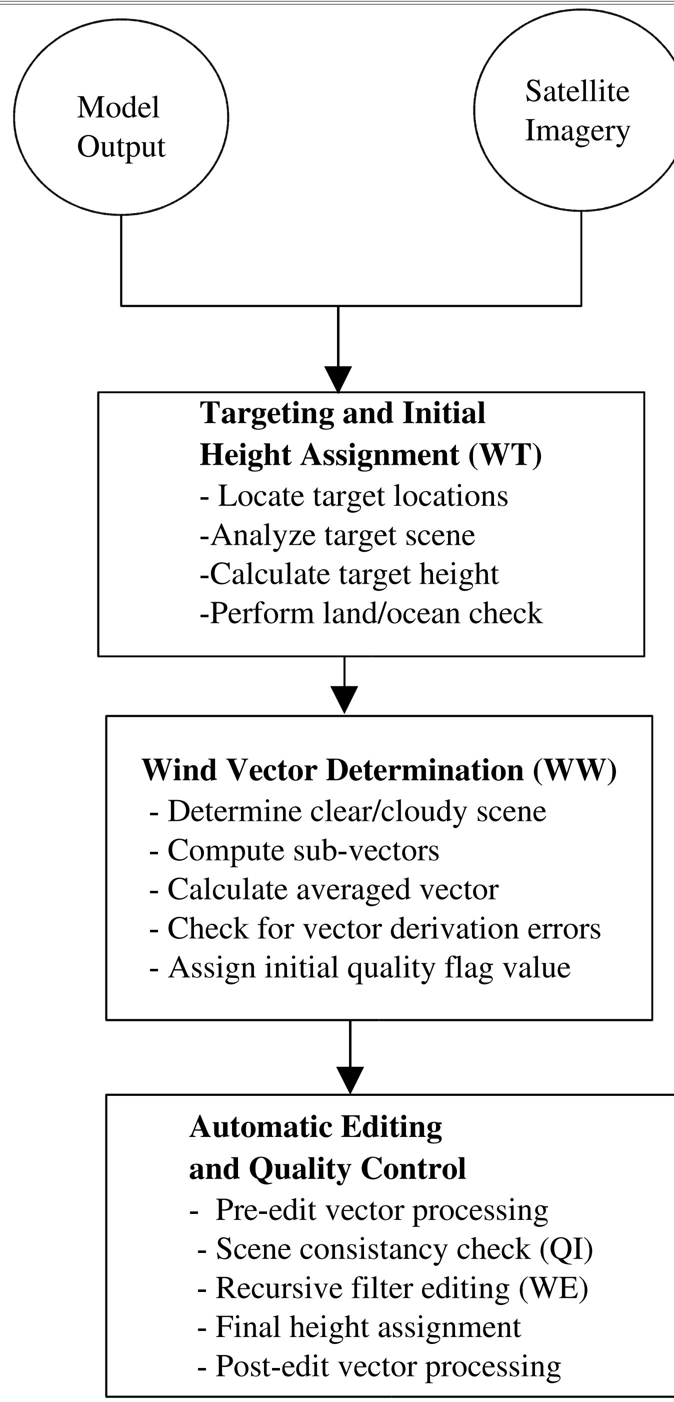

Figure 5. Overview of the satellite winds derivation algorithm.

Table 3. The EUMETSAT AMV consistency tests. From Kenneth Holmlund (1998).

Test name	Function
Direction	$\lvert D_2(x, y) - D_1(x, y)\rvert /$ $< 20\exp^{-\{[V}2^{(x, y) + V}2^{(s, y)/20] + 10} >$
Speed	$\lvert V_2(x, y) - V_1(x, y)\rvert /$ $\{0.1\,[V_2(x, y) + V_1(x, y)] + 1\}$
Vector	$\lvert \mathbf{S}_2(x, y) - \mathbf{S}_1(x, y)\rvert /$ $\{0.1\,[\lvert \mathbf{S}_2(x, y) + \mathbf{S}_1(x, y)\rvert] + 1\}$
Spatial	$\lvert \mathbf{S}(x, y) - \mathbf{S}(x - i, y - j)\rvert /$ $\{0.1\,[\lvert \mathbf{S}(x, y) - \mathbf{S}(x - i, y - j)\rvert] + 1\}$
Forecast(Background)	$\lvert \mathbf{S}(x, y) - \mathbf{F}(x, y)\rvert /$ $\{0.2\,[\lvert \mathbf{S}(x, y) + \mathbf{F}(x, y)\rvert] + 1\}$

Table 4. The accuracy of edited CMW (Cloud Motion Winds) as a function of the RF quality indicator. Vector root-mean square error is derived using rawinsondes collocated within 1 h and 222 km. SPD is the mean speed of the rawinsonde sample. "ALL" refers to all CMVs from the automatic generation and includes those that failed in the height reassignment phase. Other columns represent the sample remaining with quality at least equal to the indicated value. Units are meters per second. From Christopher M. Hayden and R. James Purser (1995).

Quality	ALL	>0	0.45	0.50	0.55	0.60	0.65	0.70	0.75
CMV rms	12.0	9.5	7.0	6.6	6.5	6.4	5.6	5.2	4.1
SPD	23	23	23	22	22	21	19	20	20
Sample	239	170	115	107	98	84	59	42	20

V. Sources of Error

Given that wind vector derivation is a complex process, there are potential sources of error that could have adverse affects on target selection, tracking and height determination. Even though there are post-processing procedures that attempt to abolish wind vectors with errors, it is not guaranteed that all the erroneous wind vectors will be eliminated in the final outputted wind product. Possible sources of error in the automatic techniques are caused by motions that are developmental instead of the actual atmospheric motion, inaccurate registration of the images, the parallax effect due to the rotation of the Earth and pixel resolution variation from nadir to the edges of the swath and from

5-1. Motion Related Sources of Error

One source of error that is mentioned above is Parallax. Parallax is the change in the angular displacement of stationary objects due to changes in position of the observer. The parallax problem is an orbital issue that causes the targets being tracked off nadir to be viewed by the satellite as being displaced farther than are in actuality. The farther the target being tracked is from nadir and from earth's surface, the larger the apparent displacement is compared to reality (Figure 6a and b). The result is a complex parallax effect which gives errors in the location of the cloud tracers. For example, at 500 km from nadir the apparent location of a cloud with a height of 3 km will be approximately 2.1 km further from nadir than its actual position and at a distance of 1000 km from nadir the displacement is 4.5 km (Figure 6b, from Key et al., 2003). This could lead to potentially large errors in winds derived from targets that lie at the along track edges of the overlapping images. The complication of this problem is that the viewing geometries and the actual cloud positions change from one orbit to next, causing in the displacements not to be the same. Correction methods to this problem are still under investigation (Key et al., 2003) .

An additional possible source of error is the navigation or registration of the satellite images. Registration is the identification of landmark locations over a set or loop of images, and errors in this can lead to misplacing the location of a cloud feature and the resultant wind vector. Navigation accuracy is important in the assignment of wind vector location. If the navigation error does not change within a triplet of images, the wind speed and direction errors will be minimal becuase they are calculated from the same relative position. However, any navigation errors for AVHRR, like MODIS, should be minimal compared to the size of the reanalysis field grid boxes (1° by 1° for ERA40).

Another source of error is due to the changing pixel resolutions from nadir to swath path edges. The pixel resolution is at a maximum at nadir and decreases with increased angle from nadir, with the lowest resolution at the edges. A tracer being viewed at varying angles off nadir from one image to the next leads to varying resolutions of the tracer, with a cloud feature that appears to be farther from the the nadir position than it actually is. This adds to the difficulty of determining the tracer location. Additionally, variations in spatial resolution can result in a change in the tracer's shape, further complicating tracking.

The final motion source of error in CMV wind derivation is cloud motions that are developmental and not representative of the actual atmospheric flow. Examples of cloud features that have developmental motions are cumulonimbus, gravity and orographic forced clouds that could lead to spurious derived winds and motions that are not representative of the actual image. However, due to very slow winds (< 4 m/s) being flagged as possible errors, cumulonimbus clouds not being a common feature over the polar regions and rigorous post-processing checking of the wind vectors compared to the background field, this should not be a common problem.

5-2. Height Determination

As mentioned earlier, the relationship between the NRMS value and the QI at mid and and low levels is inconsistent. The reason for this is mainly due to discrepancies in the height assignments (Holmlund, 1998). One such problem is the inaccurate assignment of thin cirrus clouds to lower level pressure heights when they should be assigned to a higher level (Holmlund, 1998). Another problem that can arise in height assignment of cloud targets in the IR is automatically identifying low-level polar clouds versus surface features such as snow and ice. For that above reason, calculated wind speeds under 4 m/s are flagged as possible land features by the winds derivation process. A source of error in the height determination is the location of the top of the boundary layer, which is a spatially (in the vertical) small feature that can be easily misplaced in the background field and lead to incorrect height assignments of low-level winds (Holmlund, 1998). Additional significant problems with height assignments of wind vectors arise from the temperature structure of the Arctic and Antarctic atmospheres, especially with respect to the location of temperature inversions. The atmospheric temperature structure of the Arctic or Antarctic has ubiquitous temperature inversions and significant (depth) isothermal layers (Liu and Key, 2003; Liu et al., 2006) that make height assignments very tricky (Figure 7a and b). With strong wind shear that exist in the boundary layer, incorrect (small in magnitude) height assignments of targets could lead to large differences between the derived and actual wind speed and direction at low levels near the boundary layer. Moreover, the polar atmosphere with respect to wind vectors can be barotropic, which creates significant problems in determining the height of wind vector in a isothermal layer or at two points on either side of a temperature inversion (Figures 7a and b).

The infrared window method used for cloud assignment in the AVHRR winds process is good at determining heights for opaque clouds, but does a poor job in assigning the correct heights for semitransparent clouds, such as cirrus. There are height assignment techniques that do a better job at assigning pressure heights of cloud motion features, such as the CO_2-infrared window ratio or the H_2O-infrared window intercept methods. It has been shown that the infrared window method consistently places the semitransparent cloud elements too low in the atmosphere by 100 hPa or more and is only consistent in determining the heights of opaque clouds (Nieman et al., 1993). However, due to the limitation of the AVHRR in having no CO_2 or water vapor channel, the infrared window method is the only viable method in use to assign pressure heights for this project. For the thin cirrus type clouds, low-level upwelling radiation in the atmosphere contributes significantly to the upwelling radiance (Key et al., 2003). This produces a brightness temperature that is warmer for that target and an associated pressure level that would be to too low in altitude, resulting in wind vectors that are assigned the wrong pressure heights, and have wind speeds that are too low. With the IR window method having potential issues in height assignment of wind vectors, are the AVHRR wind retrievals are accurate enough to be included into reanalysis products?

a)

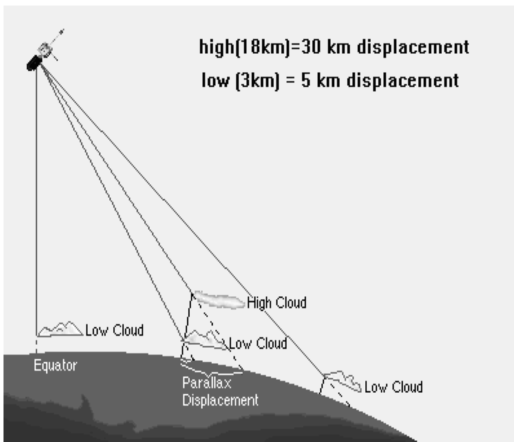

b)

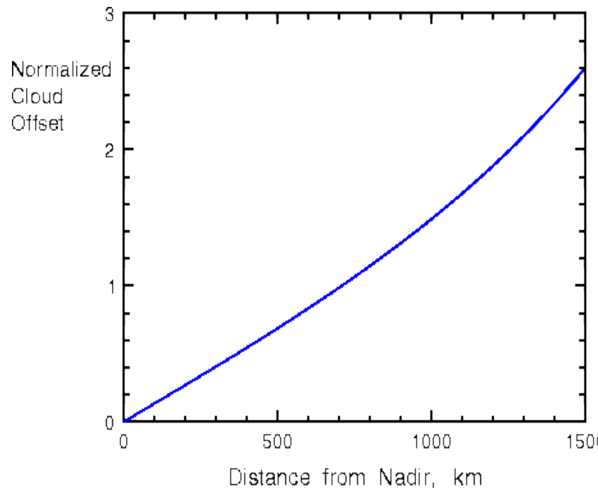

Figure 6. a) (Left) A sketch that shows that parallax causes a satellite to displace the actual location of a cloud. b) (Right) The parallax displacement that is associated with NOAA/POES (Polar Orbiting Environmental Satellites). The displacement is for any arbitrary height by taking the distance from nadir (x-axis) and multiplying the height by the Normalized Cloud Offset (y-axis) to come up with the parallax displacement.

a) b)

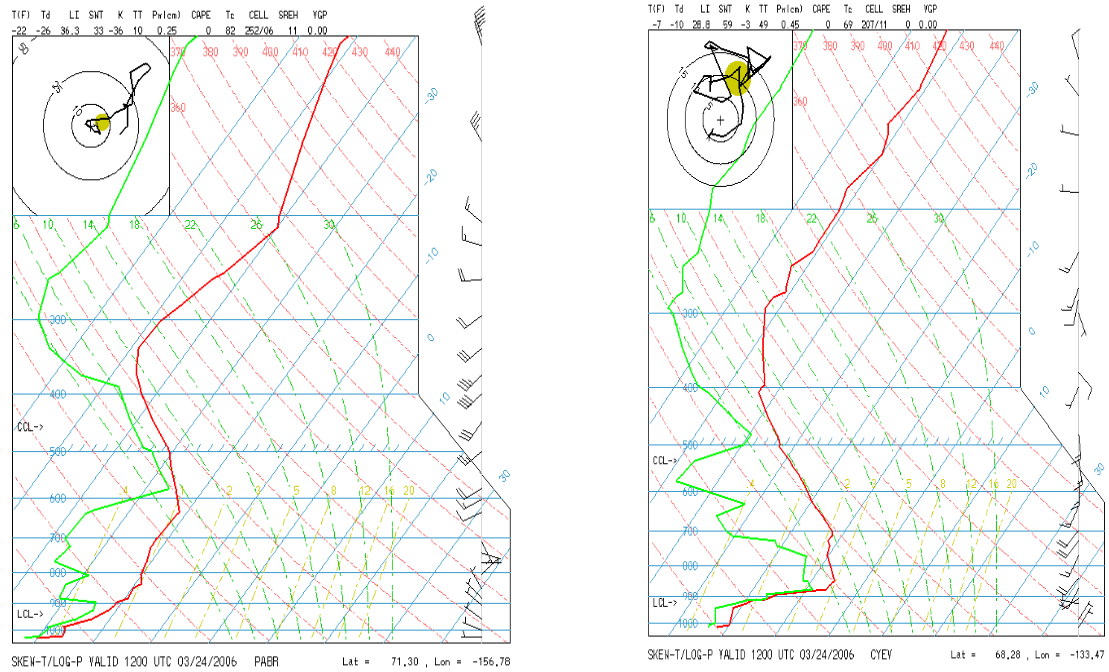

Figure 7 a) (Left) Skew-T/Log-P sounding from Barrow, Ak taken at 1200 UTC March, 24 2006. This sounding has a significant isothermal layer between 800 and 600 hPa pressure levels. b) (Right) Skew-T/Log-P sounding from Inuvik, Canada taken at 1200 UTC March, 24 2006. This sounding has a significant inversion from 950 to 850 hPa pressure levels.

VI. Validation

In order to determine whether AVHRR winds are accurate enough to be assimilated into the climatological reanalysis fields, such as ERA-40, NCEP-NCAR and JMA, validation of the winds is necessary. Validation was done by first comparing the AVHRR winds to the background reanalysis field (ERA40) to determine whether there are any obvious errors in the winds derivation process. Next, the AVHRR winds are compared to rawinsondes (winds from RAOBS) to determine how close the AVHRR winds are to actual observations, assuming that winds from RAOBS represent the actual wind. Finally, the AVHRR and ERA-40 winds are compared to rawinsonde observations that are not assimilated in the reanalysis, providing an assessment of how the AVHRR and ERA-40 winds compare to one another and give final validation on whether AVHRR outperforms ERA40 in regions void of wind data.

After the winds processing, filtering by QI and 3D objective analysis, the final graphical output indicates that the AVHRR winds can depict synoptic features if there are enough cloud features (Figures 8a and b). The Arctic winds example shows a distinct trough over the Canadian Basin into the northern Beaufort Sea and a mid-level jet southeast of the trough over the southern Beaufort Sea into the Canadian Archipelago. The Antarctic example shows a distinct cyclonic circulation over the Ross Ice Shelf and off the coast a mid to upper level jet over the Southern Ocean.

6-1. Comparison with ERA-40

A subjective graphical comparison of the AVHRR with ERA-40 winds (Figures 8a-d) indicates that the AVHRR winds are in fairly good agreement with ERA-40. The ERA-40 and AVHRR are in good agreement with the location of the trough in the Canadian Basin and the jet over the Canadian Archipelago with only small scale differences in speed and direction. For example, there are differences in direction around 80º N and between 150º to 180º W, with AVHRR having the wind direction from WNW compared to the NNW direction indicated by ERA-40. It is notable that this location in the southern Canadian Basin is a region void of wind observations. The Antarctic also has a discrepancy between AVHRR and ERA-40, with the location of the cyclone being displaced farther to the SW by AVHRR. Moreover, this is a location with only one RAOB wind observation station at Mcmurdo, which is in the vicinity of the cyclone, on the extreme northwestern edge of the Ross Ice shelf. On the other hand, the location, magnitude and direction of the jet over the Amundsen and Ross seas are in fairly good agreement between the ERA-40 and AVHRR. Another subjective comparison shown in Figures 9a-d indicates that both the ERA-40 and AVHRR have similar positions of the cyclone at mid-levels over the the central Arctic near 82º N and 160º E and the cyclone off the Antarctic coast near 78º S and 29º W. In addition, the AVHRR and ERA40 are in very good agreement on the location of the ridge over Marie Byrd Land Antarctica (Figure 1b) and the shortwave trough in between the Ross and Amundsen seas of west Antarctica in Figure 9. However, Figures 10a and b, give two examples, one over the Arctic and another over the Antarctic, where the ERA-40 and

AVHRR wind fields disagree. The Arctic example on August 5, 1993 shows that the AVHRR wind vectors are primarily more westerly compared ERA-40 at mid-levels over Ellesmere Island and northwest Greenland at 80-85° N. Overall, the AVHRR mid-level wind field has a more dramatic counter-clockwise shift in wind direction on the east and southeast side of the cyclone north of Ellesmere Island. For the Antarctic example on November 30, 2001 in Figure 10, there is a noticeable difference is wind direction at 70 to 75° south latitude and 170 to 180° E longitude over the Southern Ocean at mid-levels. The wind directions in ERA-40 at 500 hPa and AVHRR at mid-levels east of the cyclone disagree. The AVHRR wind direction is more out of the east, while the ERA-40 wind directions are more out of the north.

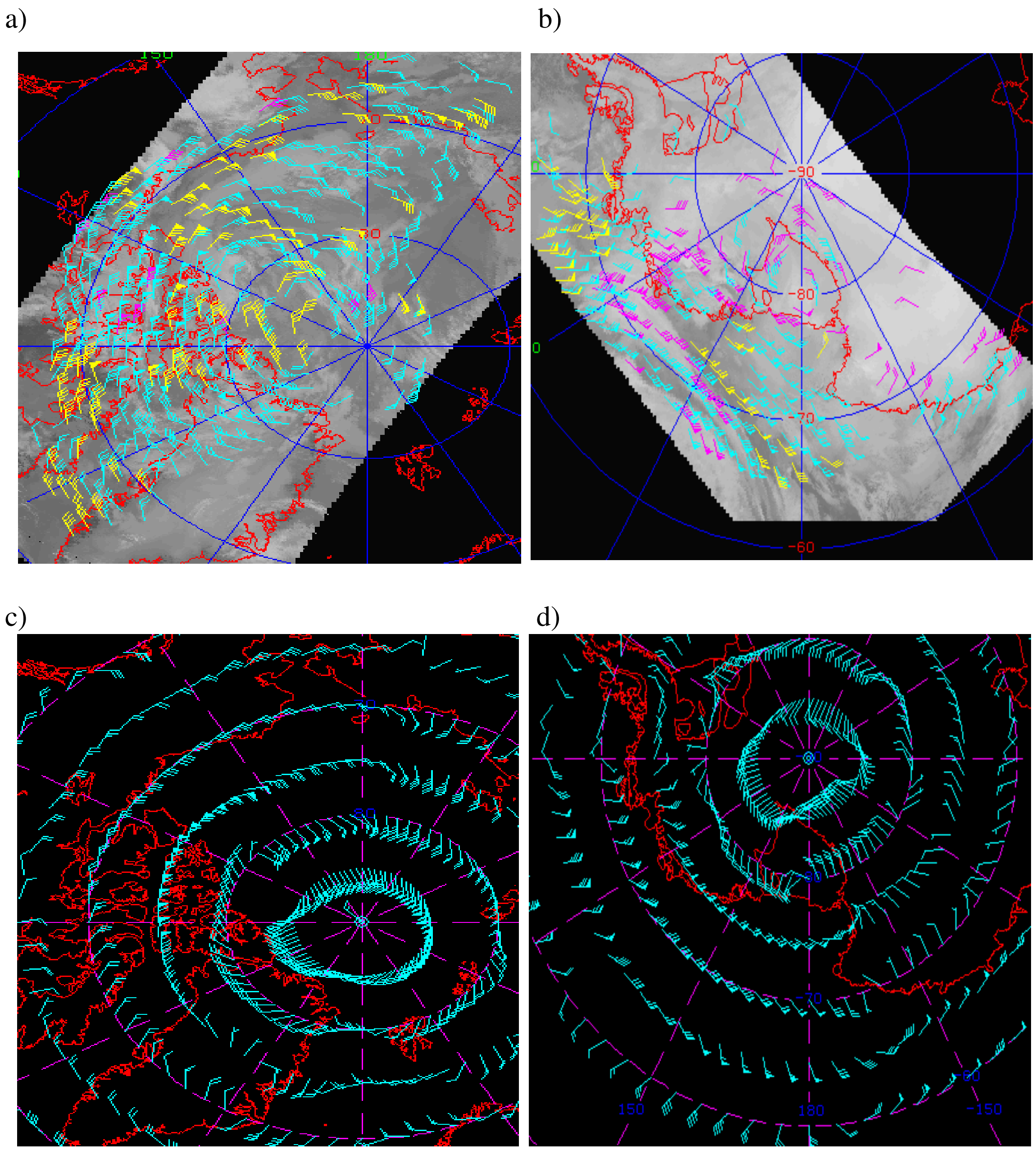

Figure 8. Examples of AVHRR cloud-drift winds over the Arctic and Antarctic in the upper panels. a) The Arctic example (upper left) was taken from 1800 UTC on August 5, 1993 from NOAA-11. b) The Antarctic example (upper right) was taken on 0600 UTC on April 25, 2001 from NOAA-16. Yellow indicates winds below 700 hPa. Blue indicates winds between 400 to 700 hPa. Magenta indicates winds above 400 hPa. Lower panels show the associated ERA-40 plots of wind speed and direction at 500 hPa for the same dates and times as the AVHRR winds above c) ERA-40 Arctic winds associated with AVHRR winds in a d) ERA-40 Antarctic winds associated with AVHRR winds in b.

a)

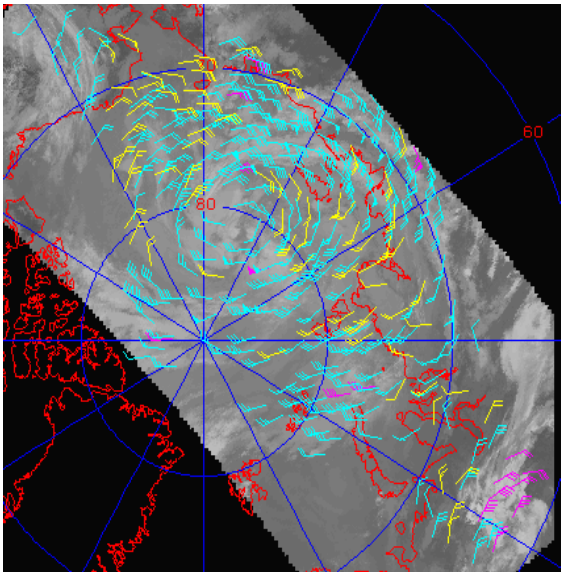

b)

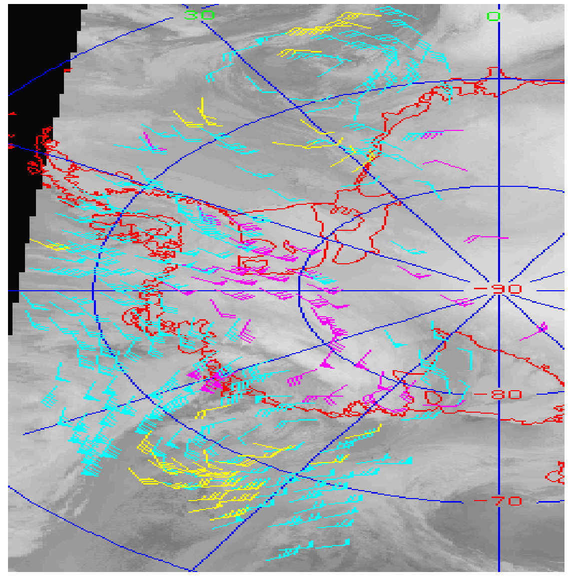

c)

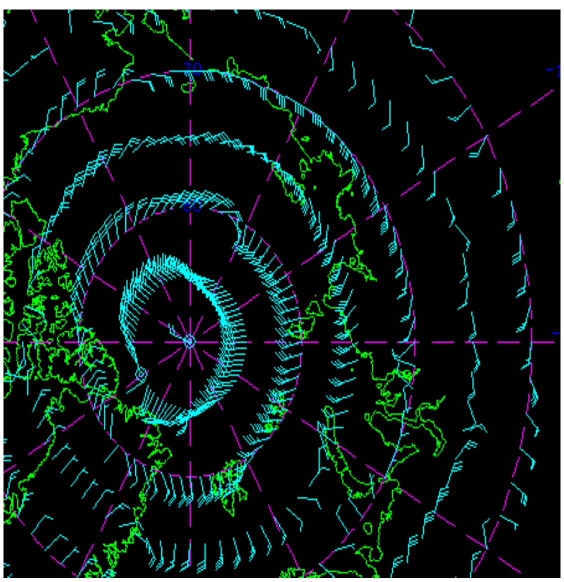

d)

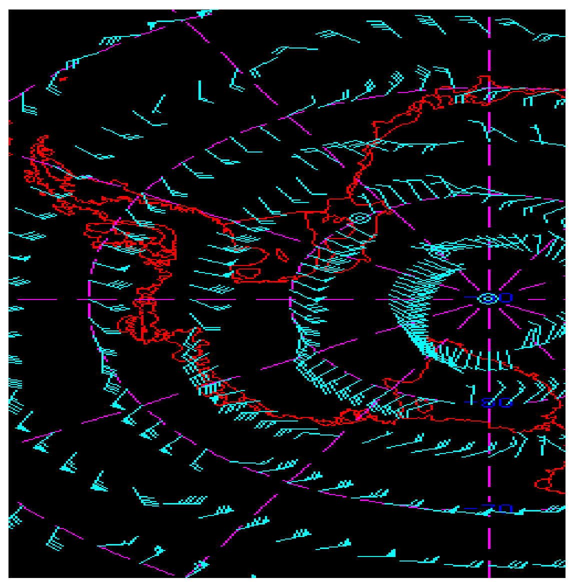

Figure 9. Another examples of AVHRR cloud-drift winds over the Arctic and Antarctic in the upper panels. a) The Arctic example (upper left) was taken from 2300 UTC on August 14, 1995 from NOAA-14. b) The Antarctic example (upper right) was taken on 0200 UTC on August 29, 1991 from NOAA-11. Yellow indicates winds below 700 hPa. Blue indicates winds between 400 to 700 hPa. Magenta indicates winds above 400 hPa. Lower panels show the associated ERA-40 plots of wind speed and direction at 500 hPa for the same dates and times as the AVHRR winds above c) ERA-40 Arctic winds associated with AVHRR winds in a d) ERA-40 Antarctic winds associated with AVHRR winds in b.

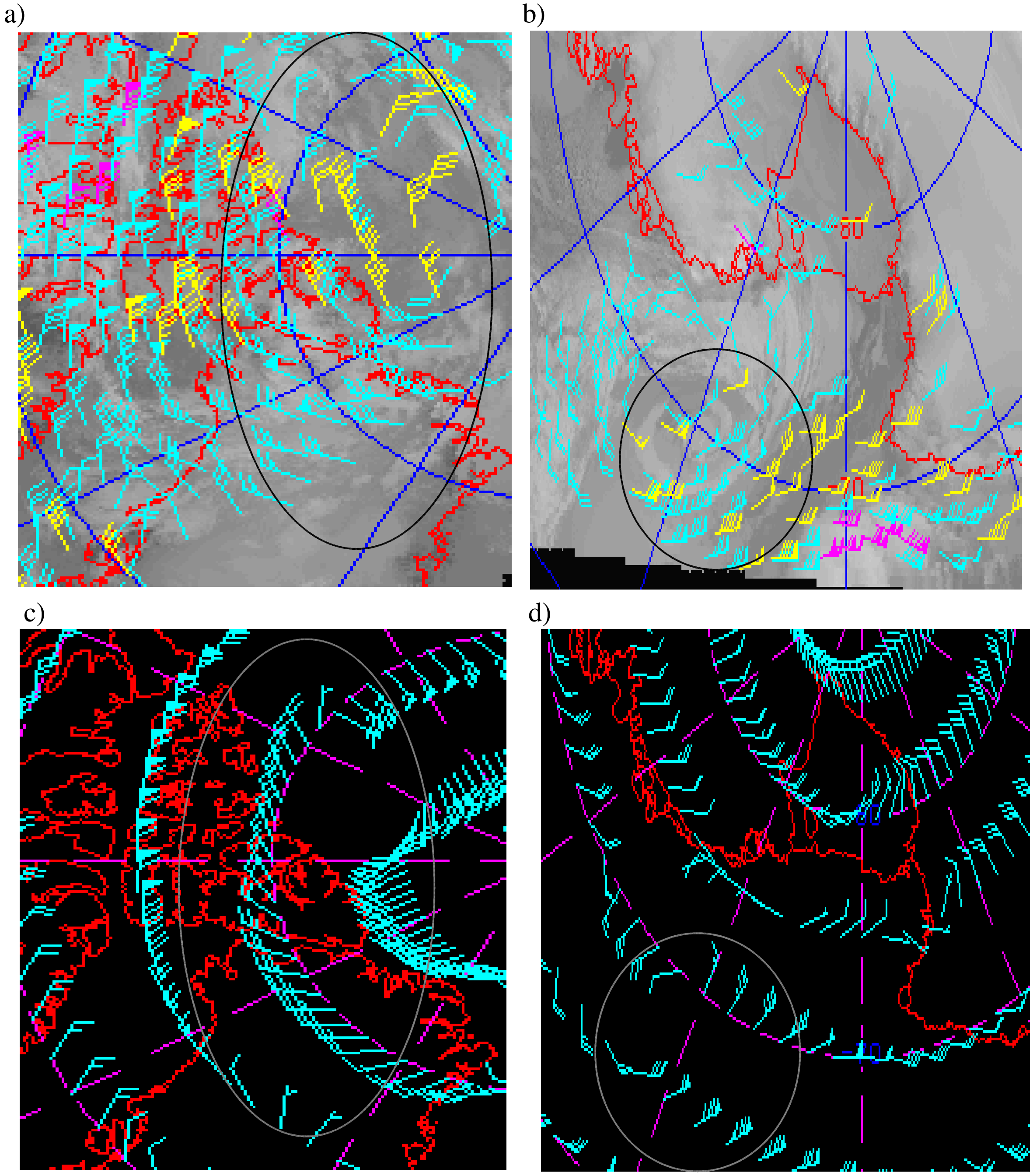

Figure 10. Examples of AVHRR cloud-drift winds differing from the ERA-40 wind field. The Arctic example on the left occurs at 1800 UTC on August 5, 1993. The Antarctic example on the right occurs at 0900 UTC on November 30, 2001 a) AVHRR image and CMVs from NOAA-11 over the Arctic. b) AVHRR image and CMVs from NOAA-16 over the Antarctic. c) Associated ERA-40 wind field over the Arctic at specified time given above. d) Associated ERA-40 wind field over the Antarctic at specified time given above.

A long term statistical comparison of AVHRR and ERA-40 winds (Table 5) over the Arctic and Antarctic for random cases from 1992 through 2000 is given for three layers in terms of the wind speed and direction root mean squared difference (RMS), the average difference, and the mean wind speeds. The statistical comparisons between AVHRR and ERA-40 indicate that the average speed differences change sign from negative (AVHRR being slower than ERA-40) in the lower and mid-levels to positive (AVHRR being faster than ERA-40) in the upper-levels over the Antarctic, with the sign change occurring at mid-levels over the Arctic. The smallest speed differences occur at mid-levels (400-700 hPa) over both the Arctic and Antarctic. The average direction differences, on the other hand, are negative (AVHRR counter-clockwise of ERA-40) for all layers over the Antarctic, and positive (AVHRR clockwise of ERA-40) for mid to upper levels and negative at low levels over the Arctic. The direction RMS decreases from 17.66 degrees at low levels to 11.54 degrees at upper levels over the Arctic, while over the Antarctic decreases from 16.23 degrees at low levels to 14.99 degrees at mid levels and increases to 15.51 degrees at upper levels. For both the Arctic and Antarctic the average directional differences are greatest at upper levels and smallest at mid levels.

The normalized speed RMS difference over the Antarctic is 16 to 18% of the mean ERA-40 wind speed at mid and upper levels and 21% of the mean ERA-40 wind speeds at low levels. The normalized speed RMS difference over the Arctic is 14% of the mean ERA-40 wind speed at upper levels and increases to 18% at mid levels and 23% at low levels. The speed RMS increases from 2.87 m/s at low levels to 3.63 m/s at upper levels over the

Antarctic. However, over the Arctic the speed RMS remains fairly constant over low to mid-levels, and then increases by 0.5 m/s at upper levels.

A comparison of statistics from MODIS cloud-track winds with ECMWF first guess analysis winds used in assimilation into the forecast model without cloud-track or water vapor winds, indicate that unlike AVHRR cloud-track winds over the Antarctic, the average speed differences (speed bias in MODIS comparisons) are positive at low levels and negative at upper levels (Tables 5 and 6). However, over the Arctic at mid-levels both MODIS and AVHRR have a positive speed difference. The overall magnitude of the speed differences are smaller in AVHRR by about 0.5 to 1 m/s over the Antarctic and by a couple tenths of a meter per second at low to mid-levels over the Arctic. However, MODIS has a lower average speed difference at upper levels by 0.14 m/s. In Francis (2002) the ERA-40 winds were found to have significant positive speed biases, being too strong by 25 to 65 percent relative to rawinsondes (Francis, 2002). The AVHRR negative average speed differences at low and mid levels over the Antarctic and low levels over the Arctic is a preliminary indication that the AVHRR winds have the potential to improve the ERA-40 product by reducing the intrinsic positive biases that are seen in the ERA-40 wind speeds.

Table 5. Statistics for AVHRR IR winds over the Arctic and Antarctic compared to ERA-40.

Low-level (below 700 hPa)	**Arctic**	**Antarctic**
Number of case	48382	29407
Speed rms	2.94 m/s	2.87 m/s
Direction rms	17.66 deg	16.23 deg
Average speed difference	-0.32 m/s	-0.08 m/s
Average direction difference	-0.47 deg	-0.80 deg
Mean ERA-40 speed	12.67 m/s	13.52 m/s
Mean AVHRR speed	12.35 m/s	13.45 m/s
Mid-level (400-700 hPa)		
Number of cases	224952	208109
Speed rms	2.93 m/s	3.16 m/s
Direction rms	14.16 deg	14.99 deg
Average speed difference	0.11 m/s	-0.02 m/s
Average direction difference	0.13 deg	-0.51 deg
Mean ERA-40 speed	15.91 m/s	17.91 m/s
Mean AVHRR speed	16.02 m/s	17.89 m/s
High-level (above 400 hPa)		
Number of cases	27741	78855
Speed rms	3.45 m/s	3.63 m/s
Direction rms	11.54 deg	15.51 deg
Average speed difference	0.34 m/s	0.45 m/s
Average direction difference	0.51 deg	-1.04 deg
Mean ERA-40 speed	25.02 m/s	22.01 m/s
Mean AVHRR speed	25.36 m/s	22.46 m/s

Table 6. (TABLE I, Key, et al., 2003) Statistics for IR MODIS winds over the Arctic from the control experiment.

	Southern Hemisphere	Northern Hemisphere
Low-level (below 700 hPa)		
NRMSVD	0.64	0.41
Speed bias (Observation-FG)(m/s)	1.36	0.54
Mean model speed (m/s)	9.66	12.80
Number of cases	15,319	62,088
Mid-level (400-700 hPa)		
NRMSVD	0.49	0.38
Speed bias (Observation-FG)(m/s)	0.56	0.30
Mean model speed(m/s)	9.66	14.70
Number of cases	90,462	78,892
High-level (above 400 hPa)		
NRMSVD	0.40	0.37
Speed bias (Observation-FG)(m/s)	-1.38	0.31
Mean model speed (m/s)	21.47	19.49
Number of cases	19,037	3,490

6-2. Comparison with Radiosonde Winds

Next, the AVHRR winds are compared to rawinsonde winds to get a better sense of how close to reality are the cloud-drift winds from AVHRR. For the research community it is essential that the quality of the product be validated to determine its accuracy, so that it meets the needs of the user community (Velden et al., 2005). For the purposes of satellite-derived winds, observed winds from radiosondes are used by consensus to determine the quality of the product, as seen in research done by Francis et al. (2005), Holmlund(1998 and 2001), Nieman et al. (1997) and Velden et al. (1997).

Validation statistics of AVHRR winds compared to radiosonde winds from IGRA that are for the most part assimilated into the reanalyses of ERA-40, NCEP/NCAR and JMA over the Arctic north of 65 deg latitude over the periods of August 1, 1988 to May 21, 1989 and March 8 to July 22, 1992 are shown in Tables 7 and 8. In addition, validation of Antarctic AVHRR winds with the handful of radiosonde stations wind datasets available over the Antarctic for random periods from August 1, 1988 to October 18, 2000 are also shown in Tables 7 and 8. A collocation was determine to be when the radiosonde and AVHRR wind vector were within a radius of 100 km in the horizontal, 50 hPa in pressure difference in the vertical coordinate and within 2 hours of time difference.

For the Arctic, the overall speed RMS for these periods is 5.45 m/s (Table 7), but is lower than the 6 m/s RMS difference of the AVHRR cloud-drift winds determined by Herman (1993). The speed RMS of 5.45 m/s is indication that the winds over the Arctic are of good quality, becuase CMV winds with speed RMS of that value have RF quality indicators of between .65 and .70 given by Table 4, with a value of 0.5 and higher being the acceptance quality indicator threshold for CMV winds (Hayden and Purser, 1995). The overall speed bias over the periods was found to be a minuscule - 0.10 m/s (Table 7), indicating that on average the speed of AVHRR winds are slightly slower than the RAOB winds, which makes this product a very good tool to correct for any long term speed biases that occur in the reanalysis wind fields. The overall normalized root mean squared (NRMS, equation 17) of about .48, and a strong correlation coefficient of about .8 are additional indicators that the AVHRR winds over the Arctic are of good quality overall (Table 7). In addition, the direction bias is under one degree counter-clockwise (- .92 degrees) of ERA-40. Furthermore, the average pressure height of the cloud-drift wind targets was about 588 hPa over the Arctic and 542 hPa over the Antarctic, and that the greatest amount of wind cases over the Arctic and Antarctic came from the mid-levels (700 to 400 hPa) as seen in Tables 8a-c.

To get a better scope of how AVHRR winds compare to the radiosonde winds, a computation of layer statistics where made (Tables 8a-c) . First, over the Arctic it is obvious that with increasing height in the atmosphere the average absolute value and RMS speed differences increase (Tables 8a-c). The speed RMS increases from 5.02 m/s at low levels to 7.57 m/s at upper levels, and the average absolute speed difference increases from 3.7 m/s at low levels to 5.4 m/s at upper levels. The increase of speed RMS with height is also observed in the comparison with the ERA-40 over the Antarctic in table 5, and was found by Schmetz (1993) that the RMS vector difference has an almost linear relationship to the mean rawinsonde wind speed. Also seen is that the direction RMS and absolute value differences decrease in quantity, or improve in quality, with increased height in the atmosphere (Tables 8a-c). The direction RMS decreases from 66.29 degrees at low levels to 42.46 degrees at upper levels, and the average absolute direction difference decreases from 47.39 degrees at low levels to 25.07 degrees at upper levels. The direction bias is greatest at low levels at -1.67 degrees and decreases to - 0.99 degrees at mid-levels, and increases to + 1.48 degrees at upper levels. Overall, AVHRR is counter-clockwise of the RAOB winds at low and mid-levels and more clockwise at upper levels. The speed biases are slightly positive (AVHRR 0.16 m/s faster) at low levels, negative at mid-levels (AVHRR 0.29 m/s slower) and positive at upper levels (AVHRR 0.77 m/s faster). It is shown in Tables 8a-c that the NRMS (correlation coefficients) decreases (increases) from 0.7 (0.6) at low levels to .37 (.81) at upper levels. This shows along with decreasing RMS and average absolute direction differences from low to upper levels that the overall quality of the winds increase from low to upper levels.

Next, AVHRR winds over the Antarctic where compared to radiosonde winds from IGRA that are for the most part assimilated into the reanalysis field. The results in Tables 8a-c shows that overall, when compared to AVHRR winds over the Arctic, the AVHRR winds over the Antarctic at low and mid-levels are less accurate, but have similar accuracy at upper levels (Tables 8a-c). The AVHRR winds show significant speed biases of greater than one meter per second at all levels, with the most significant bias at over 4 m/s at low levels. At all levels the AVHRR winds are faster than rawinsondes and therefore have a overall positive speed bias of 3.01 m/s faster than ERA-40 (Table 7). The speed RMS for AVHRR winds are about 3 m/s higher at low levels, 2.4 m/s higher at mid levels, and only .15 m/s higher at upper levels. The NRMS value of low level winds over the Antarctic is over one and the correlation coefficient is 0.10, which indicates the very poor quality of low level AVHRR winds over the Antarctic.

One possible reason for the poor height assignments of low level winds are caused by ubiquitous and very strong temperature inversions that are seen over the Antarctic. The inversions are much stronger over the Antarctic than over the Arctic (Liu and Key, 2003), which would make height assignments of targets more difficult and therefore produce more erroneous height assignments of wind vectors at low levels over the Antarctic. Another possible reason is that the background field (ERA-40) is misplacing the top of the boundary layer, which is a vertically small structure that can be easily misplaced and is associated with strong wind speed and direction shear that could result in accurate height assignments of low level AVHRR wind vectors.

With increased altitude of the AVHRR wind vector, the quality becomes noticeably better (Tables 8a-c). This is shown by lowering NRMS values from 1.14 at low levels, to 0.56 at mid-levels, and to 0.35 at upper levels. In addition, increased correlation coefficients from 0.1 at low levels, to 0.62 at mid-levels, to 0.79 at upper levels. Furthermore, when compared to the Arctic, correlation coefficients are noticeably lower at mid-levels over the Antarctic and are about the same at upper-levels (Tables 8a-c). Comparing Arctic and Antarctic NRMS values (Tables 8a-c) show that they are noticeably lower over the Arctic at mid-levels, while they are similar at upper-levels.

In summary, The quality of the AVHRR winds over the Antarctic is very poor at low-levels, but better quality is seen at increasing altitude with decreasing positive speed bias, NRMS and direction RMS, and increasing correlation coefficients. Furthermore, the quality of AVHRR winds over the Antarctic is very good at upper levels, with quality at upper levels that is about equal to AVHRR winds over the Arctic.

Table 7. Statistical comparison of the AVHRR winds to rawinsondes over the Arctic and Antarctic for all levels in the atmosphere (speed in meters per second).

For All Levels	**Arctic**	**Antarctic**
Sample size	30413	2170
Speed RMS	5.45	7.67
Direction RMS	55.49	36.5
Speed bias	-0.1	3.01
Avg. abs. spd. diff.	3.98	5.8
Direction bias	-0.92	1.2
Avg. abs. dir. diff.	36.57	23.54
Mean AVHRR speed	11.2	18.11
Mean RAOB speed	11.3	15.1
NRMS	0.48	0.51
Correlation coefficient	0.8	0.71
Average target height	587.82	542.1

Table 8. Statistical comparison of the AVHRR winds to rawinsondes over the Arctic and Antarctic for individual layers in the atmosphere. a) Low levels: below 700 hPa b) Mid levels: 700 to 400 hPa c) Upper levels: above 400 hPa

a)

Low Levels: Below 700 hPa	**Arctic**	**Antarctic**
Sample size	6449	115
Speed RMS	5.02	8.12
Direction RMS	66.29	70.43
Speed bias	0.16	4.98
Avg. abs. spd. diff.	3.7	6.28
Direction bias	-1.67	-3.37
Avg. abs. dir. diff.	47.39	50.31
Mean AVHRR speed	7.37	12.11
Mean RAOB speed	7.21	7.14
NRMS	0.7	1.14
Correlation coefficient	0.6	0.1

b)

Mid Levels: 700 to 400 hPa	**Arctic**	**Antarctic**
Sample size	21375	1822
Speed RMS	5.26	7.69
Direction RMS	53.31	36.89
Speed bias	-0.29	3.11
Avg. abs. spd. diff.	3.89	5.78
Direction bias	-0.99	1.35
Avg. abs. dir. diff.	34.7	24.65
Mean AVHRR speed	11.17	16.95
Mean RAOB speed	11.46	13.83
NRMS	0.46	0.56
Correlation coefficient	0.79	0.62

c)

Upper Levels: 700 to 400 hPa	Arctic	Antarctic
Sample size	2589	369
Speed RMS	7.57	7.72
Direction RMS	42.46	20.61
Speed bias	0.77	2.12
Avg. abs. spd. diff.	5.4	5.91
Direction bias	1.48	2.3
Avg. abs. dir. diff.	25.07	14.31
Mean AVHRR speed	21.04	24.21
Mean RAOB speed	20.28	22.09
NRMS	0.37	0.35
Correlation coefficient	0.81	0.79

Table 9. A sample statistical comparison of the MODIS IR winds compared to radiosonde winds.

ARCTIC:

All Levels

Speed RMS 5.04
Direction bias -0.5510
Speed bias -0.6365
Sample size: 3,397

ANTARCTIC:

All Levels

Speed RMS 4.97
Direction bias 2.0326
Speed bias -0.4777
Sample size: 1,072

Finally, a sample statistical comparison of real-time MODIS IR winds to radiosonde winds is shown in Table 9. Compared to real-time MODIS IR winds, the overall RMS speed differences compared to radiosondes is slightly (0.41 m/s) smaller for MODIS than it is for AVHRR historical winds over the Arctic (Tables 7 and 9). However over the Antarctic, MODIS has a much noticeable lower speed RMS of 4.97 m/s compared to AVHRR historical winds 7.67 m/s, and MODIS speed bias that is - 0.48 m/s compared to 3.01 for AVHRR historical winds (Tables 7 and 9). This is likely the result of better height assignments for MODIS winds due to it having a water vapor and CO_2 channels that allow for additional height assignment techniques to be used (i.e., Water Vapor-IR intercept, and CO_2-IR ratio methods) for more accurate wind vector height determination. Like MODIS, AVHRR shows a negative speed bias over the Arctic, however, the value is smaller in magnitude for AVHRR Arctic winds (Tables 7 and 9) . However, on the other hand, MODIS has a noticeable smaller direction bias of - 0.55 degrees compared to AVHRR's - 0.92 degrees over the Arctic (Tables 7 and 9). However, AVHRR historical winds have a obvious smaller direction bias of 1.2 degrees compared to 2.04 degrees in MODIS over the Antarctic (Tables 7 and 9). However, it is important to mention that the MODIS winds use a different background field. The real-time MODIS winds use GFS (Global Forecast System), while the AVHRR historical winds use the ERA-40. Being that the GFS background is a six to twelve hour forecast, could make that background field less reliable than ERA-40, which is a reanalysis field that has gone through rigorous processing. Therefore, it cannot be asserted that AVHRR has better speed bias over the Arctic and direction bias over the Antarctic for any remote sensitivity reasons, however, it can be asserted that the AVHRR historical product would be better suited for the reanalysis fields than MODIS because AVHRR has a longer dataset and given serious consideration to be included in future reanalysis fields (excluding low-levels over the Antarctic) based on the statistics given above.

6-3. Comparison to Rawinsondes Not Assimilated into Reanalysis

It is imperative to compare the AVHRR and ERA-40 winds against each other to rawinsondes not assimilated into the reanalysis field. The reason is to determine whether the AVHRR winds outperform ERA-40, and therefore be useful for assimilation into future reanalysis to correct any errors that are in currently in the reanalysis wind fields. The CEAREX and LeadEx field experiments were two cases where the radiosonde wind data was not assimilated into the reanalysis products. Therefore, the data provided by these field experiments, which has been used in previous research (Francis, 2002) to validate reanalysis wind data values, is also used in this research project to determine the quality of AVHRR versus ERA-40 winds .

As is mentioned by Francis (2002)[9] and is indicated in Tables 10a-c, the ERA-40 has a significant positive speed bias in the Arctic regions void of assimilated radiosonde data. Table 10a also indicates that AVHRR has a positive speed bias overall, however, the magnitude of the speed bias is .22 m/s, which is much smaller than 1.36 m/s for ERA-40. In addition, the AVHRR winds have smaller average absolute and RMS speed difference than ERA-40 (Table 10a-c). Overall, the speed RMS and average absolute speed differences of

9 Table 2. in Geophysical Research Letters, **Validation of reanalysis upper-level winds in the Arctic with independent rawinsonde data** by Jennifer A. Francis Vol. 29 shows the significant speed positive in ERA40.

AVHRR is 6.6 m/s and 4.56 m/s compared to 6.86 m/s and 4.65 m/s for ERA-40. However, it is also observed that that ERA-40 has a slightly better direction bias and RMS difference overall (Tables 10a). AVHRR had a total direction RMS of 53.25º and bias of -2.46º compared to ERA-40 direction RMS of 51.91º and bias of 2.34º degrees. The direction bias is noticeably better in ERA-40 at low levels, with a direction bias of + 1.49 degrees compared to – 9.85 degrees in AVHRR (Table 10b). The smaller speed bias and RMS difference of AVHRR over ERA-40 shows that AVHRR has potential to be assimilated into future ERA reanalysis products to correct for the positive speed bias. Also, Francis (2002)[10] shows that the same positive speed bias is in NCEP/NCAR reanalysis over the Arctic. Therefore, in the future it could be shown that the AVHRR CMVs could be assimilated in NCEP/NCAR reanalysis products for the same reason.

10 Table 1. in Geophysical Research Letters, **Validation of reanalysis upper-level winds in the Arctic with independent rawinsonde data** by Jennifer A. Francis Vol. 29 shows the significant speed positive in ERA40.

Table 10. Statistical comparison of the AVHRR winds compared to radiosonde winds that are NOT assimilated into the reanalysis from the periods of CEAREX and LeadEx. Due to the sparsity of upper level (above 400 hPa) collocations (within a point difference of 100 km by 50 hPa) of AVHRR with ERA-40. The layer statistics of mid and upper levels are combined. a) Total statistics. b) Layer statistics for below 700 hPa. c) Layer statistics for above 700 hPa.

a)

Total Statistics	**AVHRR**	**ERA-40**
Collocations = 412		
Speed RMS	6.6	6.86
Direction RMS	53.25	51.91
Speed Bias	0.22	1.36
Direction Bias	-2.46	2.34
Avg. abs. spd. diff.	4.56	4.65
Mean spd (Raob = 6.57 m/s)	6.79	7.93

b)

Lower Levels: Below 700 hPa		
Collocations = 192	**AVHRR**	**ERA-40**
Speed RMS	6.06	6.26
Directions RMS	52.78	53.48
Speed Bias	-0.47	0.93
Direction Bias	-9.85	1.49
Avg. abs. spd. diff.	4.19	4.39
Mean Raob spd (RAOB = 5.80 m/s)	5.34	6.74

c)

Mid and Upper Levels, ABOVE 700 hPa

Collocations = 220	AVHRR	ERA-40
Speed RMSE	7.02	7.31
Directions RMSE	53.68	50.58
Speed Bias	0.89	1.79
Direction Bias	4.79	3.41
Avg. abs. spd. diff.	4.89	4.88
Mean Raob spd (RAOB = 7.17 m/s)	8.06	8.96

6-4. Comparison to TOVS

Herman and Nagle (1994) found that the AVHRR winds were comparable to gradient winds computed from High-Resolution Infrared Sounder (HIRS) with a RMS difference less than 5 m/s (Key et al., 2003). Comparisons of AVHRR over the Arctic with TOVS derived winds were also made, and it was found that the correlation coefficients for various samples was in the range of .7 to .8 indicating a moderately strong correlation.

Daily wind field comparisons of TOVS, ERA-40 and AVHRR given in Figure 11 shows that the wind fields at 600 hPa for these particular days are in general similar, however, there are certain distinct differences among the wind fields. For example, in Figure 11a, the AVHRR and ERA-40 U-component winds differ from TOVS over the Laptev and western Chukchi seas, where the U-component of the winds are weaker in magnitude in the ERA-40 and AVHRR fields. In addition, in Figure 11a, there is a noticeable offset of the local maximum in the V-component of TOVS over the central Arctic compared to ERA-40 and AVHRR, where the local maximum in the V-component is displaced farther west in TOVS and the magnitude is stronger in ERA-40. Another example of differences is in Figure 11b, where ERA-40 and AVHRR have a much stronger V-component wind speed over the western central Arctic compared to TOVS. Furthermore, TOVS and ERA-40 have a much broader and stronger easterly component of the total wind than AVHRR does over the Barents sea and Canadian Archipelago on that same day. Lastly, in Figure 11c, there are also distinct differences in the wind fields, for example, the magnitude of the V component over the northern Laptev sea in AVHRR is in-between the TOVS and ERA-40, and easterly wind components are stronger and more expansive across the Chukchi sea in the ERA40 and AVHRR than in TOVS.

a)

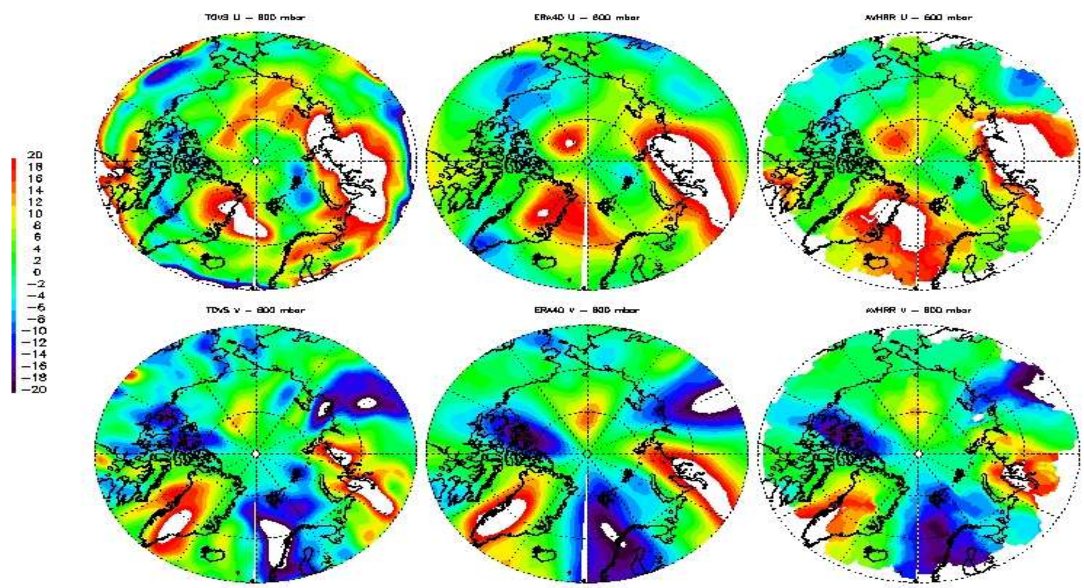
20
18
16
14
12
10
8
6
4
2
0
−2
−4
−6
−8
−10
−12
−14
−16
−18
−20

b)

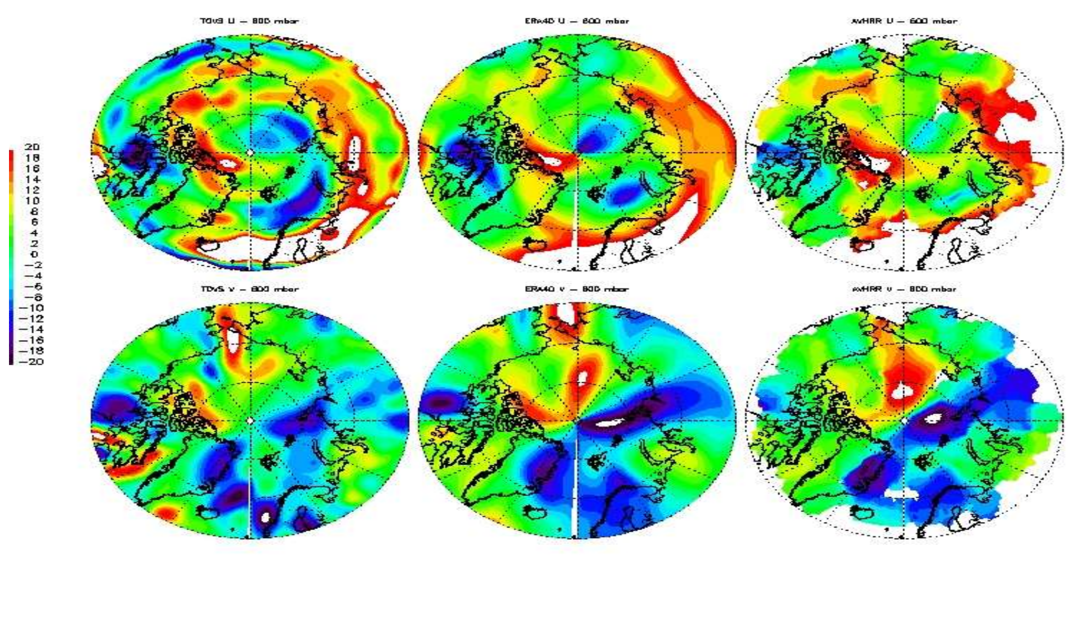
20
18
16
14
12
10
8
6
4
2
0
−2
−4
−6
−8
−10
−12
−14
−16
−18
−20

c)

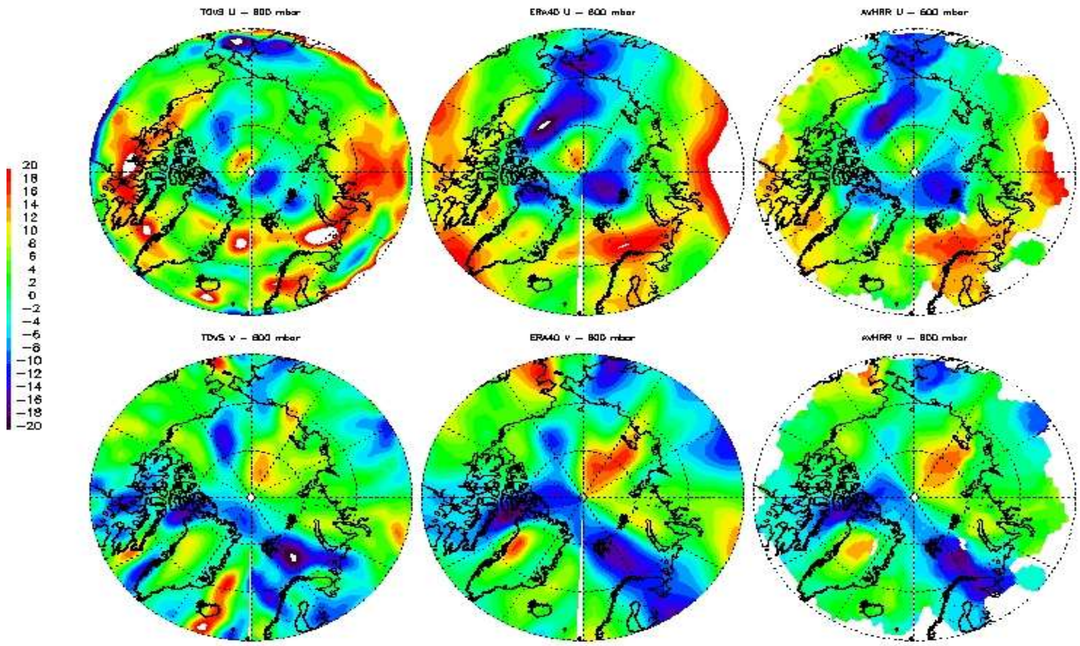

Figure 11. a) Daily wind fields on October 27th, 1997 for TOVS (left), ERA40 (middle) and AVHRR(right). Top is the the U-component of the wind and bottom is the V-component of the wind. b) Same as for a except for November 1st, 1997. c) Same as for a and b, but for November 5th, 1997.

6-5. Comparison of AVHRR and ERA-40 Between Data Rich and Data Void Regions

A long term inter-comparison of statistical differences between AVHRR and ERA-40 over the Arctic of 178,321 cases that are over one degree latitude and longitude from a RAOB observation station and 1,830 cases within a 100 km of a RAOB wind observation that should be assimilated into the reanalysis found that the larger differences in wind speeds were in areas outside the one degree latitude and longitude from a RAOB station that has data that is available to be assimilated into the reanalysis (Table 11). This is also found to be the case for direction differences at mid and upper levels. Moreover, it was found as to be expected that the speed RMS and average absolute speed differences are larger in the data void regions (outside one degree latitude and longitude from RAOB station). For example, the speed RMS at upper levels increased by .66 m/s in the data void regions. In addition, the frequency of larger speed (> 3 m/s) and vector differences (> 5 m/s) go up as well in data void regions. Furthermore, there is a noticeable increase in the average absolute direction difference and direction rms at upper levels (Table 11). For example, the direction RMS at upper levels increases by 3 degrees in the data void regions. However, the opposite is seen at low-levels, where the average absolute direction difference and RMS increased near RAOB observation locations (within 100 km). The reason for this could be that the direction quality of the AVHRR winds at low-levels are poor. This indicated by the comparison statistics with RAOB winds, as it is seen that the largest direction RMS values occur at low levels (Table 8a). However, with overall larger speed and direction RMS and average absolute differences being measured in regions void of radiosonde data is further indication that on average, the ERA-40 is probably missing atmospheric flow features that are being observed by AVHRR cloud motion vectors. With the ERA-40 missing atmospheric flow features in data void regions, the speed and direction differences compared to a more accurate field, such as AVHRR would overall be greater in those regions.

Table 11. Statistical comparison over the Arctic of the AVHRR to ERA-40 winds that are within one degree latitude and longitude of a RAOB station that has wind data available to be assimilated into the reanalysis (left column) and statistical comparison of AVHRR to ERA-40 winds that are NOT near (outside one degree latitude/longitude range) any RAOB station that has wind data assimilated into the reanalysis (right column). A comparison is made when the AVHRR and ERA-40 winds are within 25 km and 25 hPa of each other. larger speed differences are differences greater than 3 m/s and larger vector differences are differences greater than 5 m/s.

Inside 100 km distance of RAOB station with wind observations: cases: 1,830	**Outside one degree lat/lon of RAOB station: cases: 178,321**
Below 700 hPa	**Below 700 hPa**
speed RMS: 2.21 m/s direction RMS: 18.80° abs avg speed diff: 1.91 m/s abs avg direction diff: 13.87° % larger speed diff : 11 % % larger vector diff: 10 %	speed RMS: 2.94 m/s direction RMS: 17.76° abs avg speed diff: 2.37 m/s abs avg direction diff: 12.73° % larger speed diff : 17 % % larger vector diff: 10 %
700 to 400 hPa	**700 to 400 hPa**
speed RMS: 2.82 m/s direction RMS: 13.84° abs avg speed diff: 2.25 m/s abs avg direction diff: 10.06° % larger speed diff : 12 % % larger vector diff: 8 %	speed RMS: 2.93 m/s direction RMS: 14.18° abs avg speed diff: 2.35 m/s abs avg direction diff: .10.09° % larger speed diff : 17 % % larger vector diff: 10 %
Above 400 hPa	**Above 400 hPa**
speed RMS: 2.79 m/s direction RMS: 8.30° abs avg speed diff: 2.18 m/s abs avg direction diff: 6.38° % larger speed diff : 18 % % larger vector diff: 9 %	speed RMS: 3.45 m/s direction RMS: 11.56° abs avg speed diff: 2.73 m/s abs avg direction diff: 7.08° % larger speed diff : 23 % % larger vector diff: 17 %

VII. Results

To improve the overall quality of both AVHRR CMV and reanalysis wind products, it is important to determine the atmospheric conditions that produce the greatest differences between both products. For example, is there an atmospheric condition that causes ERA-40 to have a positive or negative bias in wind speed. or is there an atmospheric condition in which causes ERA-40 to have larger vector differences when compared to AVHRR derived winds? In finding the condition that produces errors in the the wind product, the product can be improved by diagnosing the cause of the errors and then making adjustment for the condition that cause errors in the product.

First, an investigation into where AVHRR cloud-drift wind vectors are most common in the atmospheric flow are identified. Second, case studies are shown to identify areas of significant differences between AVHRR and ERA-40 and any common characteristics between the individual case studies are discussed. Next, a longer term assessment of the relationship between the sign and magnitude of the differences between AVHRR and ERA-40 with an atmospheric flow pattern or type that reproduces similar differences is discussed. Finally, there is a discussion of possible reasoning behind any reoccurring difference pattern and causes of error in the reanalysis.

7-1. Where are the AVHRR Cloud-Drift Winds in the Atmospheric Flow?

The location of AVHRR cloud-drift winds provides insight to where in atmospheric flow will the AVHRR winds have the greatest potential impacts in the re-analysis field. During a four month case study of AVHRR wind vectors during March through May 1992 and May through July 1995, there were 35,243 wind vectors at upper levels above 500 hPa, 33,418 wind vectors at low-levels (below 700 hPa) and 109,472 wind vectors at upper levels above 300 hPa. Of the upper level winds, 64% occurred in regions of negative relative vorticity (anticyclonic curvature), and 36% occurred in positive relative vorticity (cyclonic curvature). At mid-levels 52% occurred in regions of negative relative vorticity and 48% occurred in positive relative vorticity. At low-levels 55% occurred in positive relative vorticity and 45% occurred in negative relative vorticity. Relative vorticity (equation 18) is negative in the Northern Hemisphere in regions of anticyclones.

$$\zeta = (\partial V/\partial x - \partial U/\partial y) \quad (18)$$

Anticyclones are characterized by downward vertical motion and clear sky conditions, therefore, cloud-drift winds would not be expected to occur frequently in these locations. However, when dealing with upper level cloud-drift winds (above 500 hPa) the targets being tracked, usually cold cloud tops, are associated with higher level or deep layer clouds.. The colder/higher cloud tops tend to occur downstream of trough into flow over the top of ridges (Figure 12), and explain the higher frequency of wind vectors observed in regions of negative vorticity. At mid-levels there is about an equal frequency of wind vectors occurring in regions of negative and positive relative vorticity. There is a higher frequency of low-level winds in areas of positive vorticity, associated with resultant vertical motions from cyclones and troughs that produce clouds.

The same frequency is observed when the wind vectors are assigned to ridges or troughs using the sign of the components of the geostrophic and ageostrophic wind. A wind vector is determined to occur in a ridge when the u,v components of the ageostrophic wind are the same sign as the geostrophic wind components, and in a trough when the u,v components of ageostrophic wind are in opposite sign of the geostrophic wind components (Figure 16a). The gradient wind is greater than the geostrophic wind in ridges and less than the geostrophic wind in troughs (equations 19 and 20).

$$\mathbf{V_{gr}}\mathbf{=}[1 + K\mathbf{V_{gr}} \,\mathbf{/}\, f_o\mathbf{]}^{-1}\,\mathbf{Vg} \quad (19)$$

$$\mathbf{V_a} = \mathbf{V_{gr}} \,\mathbf{-}\, \mathbf{Vg} = -\,\mathbf{[}\, K\mathbf{V_{gr}} \,\mathbf{/}\, f_o \mathbf{]}\, \mathbf{V_{gr}} \quad (20)$$

With this classification, 64% of wind vectors occur in ridges and 36% of wind vectors occur in troughs above 500 hPa, 54% of wind vectors occur in ridges and 46% in troughs from 700 hPa to 500 hPa, and 53% of wind vectors occur in troughs and 47% in ridges below 700 hPa. With a more restrictive definition of a trough (ridge) occurring in relative vorticity of + $4*10^{-5}$ (- $4*10^{-5}$) or greater (less), there is a more noticeable increase in the frequency of wind vectors that occur in troughs at mid and lower levels and in ridges at upper levels (Figure 13a-c). At lower levels 75% of the cloud motion vectors (CMVs) occurred in troughs and 25% occurred ridges. For mid-level CMVs, 61% occurred in trough and 39% occurred in ridges, and for upper-level CMVs, 70% occurred in ridges and 30% in troughs (Figures 12 and 13a-c) .

Above 500 hPa AVHRR cloud-drift winds are most common in regions of Positive Vorticity Advection (equation 21), which is upstream of the ridge axis and downstream of the trough axis (Figure 14c).

$$V \bullet \nabla(\zeta + f_o) = V \bullet \nabla[(\partial V/\partial x - \partial U/\partial y) + f_o] \quad (21)$$

Overall, AVHRR wind vectors that are upstream of the ridge axis and downstream of the trough axis occur in 65% of the cases. In only 35% of the cases do AVHHR wind vectors occur downstream of the ridge axis and upstream of the trough axis. This is expected, as vertical motion and cloud development would occur in regions of PVA downstream of the trough axis and upstream of the ridge, where divergence of the ageostrophic wind occurs (Figures 12, 14c and 16a) At mid and lower-levels, there is nearly equal amount of wind vectors that occur in regions of PVA and in NVA, with 53% (47%) of the CMVs being in a region of PVA (NVA) at mid-levels, and with 49% (51%) of the CMVs being in a region of PVA (NVA) at low-levels.

Of all the AVHRR winds produced above 500 hPa, nearly one quarter occur in either jet exit or entrance region (defined as region where the gradient of the wind speed parallel to geopotential heights greater than + .35 m/s per kilometer for jet entrance and - .35 m/s per kilometer for jet exit). There is a noticeable higher frequency of wind vectors in the jet exit region at upper levels (Figure 15b). Of the AVHRR winds that occur in either jet exit or entrance regions, 79% occur in a jet exit region, while 21% occur in a jet entrance region. Of all wind vector cases in the jet exit region, 70% occur in the left jet exit quadrant and 30% occur in the right jet exit quadrant. The left jet exit quadrant is define as where vorticity advection (equation 21) is positive and right jet exit quadrant is where vorticity advection is negative, while the left jet entrance quadrant is defined as where vorticity advection is negative and right jet entrance quadrant is where vorticity advection is positive. Of all wind vector cases in the jet entrance region, 64% occurred in the the right jet entrance quadrant, while 36% occur in the left jet entrance quadrant (Figure 15b). The reason for a greater percentage of wind vectors in the left jet exit than right jet exit, and in the right jet entrance than the left jet entrance , is that in those jet quadrants positive divergence and upward vertical motion typically occurs, leading to cloud formation and greater chances that cloud targets will be tracked and wind vectors generated. At mid-levels, there is also a noticeable higher frequency of CMVs that occur in the left jet exit region (Figure 15a), with 41% infer occurring the left jet exit quadrant, 18% in the right jet exit quadrant, 21% in the left jet entrance quadrant and 19% in the right jet entrance quadrant.

Overall, above 500 hPa, in the upper levels of the atmosphere over the Arctic, the majority of the AVHRR winds occur in regions where upper-level cloud tops are expected to occur, in regions of PVA downstream of the trough and upstream of the ridge axis, in flow over the top of ridges, and in the jet exit region (especially left quadrant, where there is upward vertical motion producing clouds) upstream of the ridge axis.

At mid-levels there is about an equal chance of getting a CMV in a region of positive or negative relative vorticity and in regions of PVA or NVA. However, there is a higher frequency of CMVs in troughs or cyclones, where the relative vorticity is greater than $4*10^{-5}$ s^{-1}, and in the left jet exit quadrant of mid-level jet streaks.

At low-levels there is a much higher frequency of CMVs in troughs or cyclones, where the relative vorticity is greater than $4*10^{-5}$ s^{-1}, and an equal chance of getting a wind vector in either a region of PVA or NVA. As would be expected, compared to regions of larger negative relative vorticity, there is a very noticeable larger frequency of CMVs that occur in regions of larger positive relative vorticity at low and mid levels, because of the higher frequency of clouds in such regions.

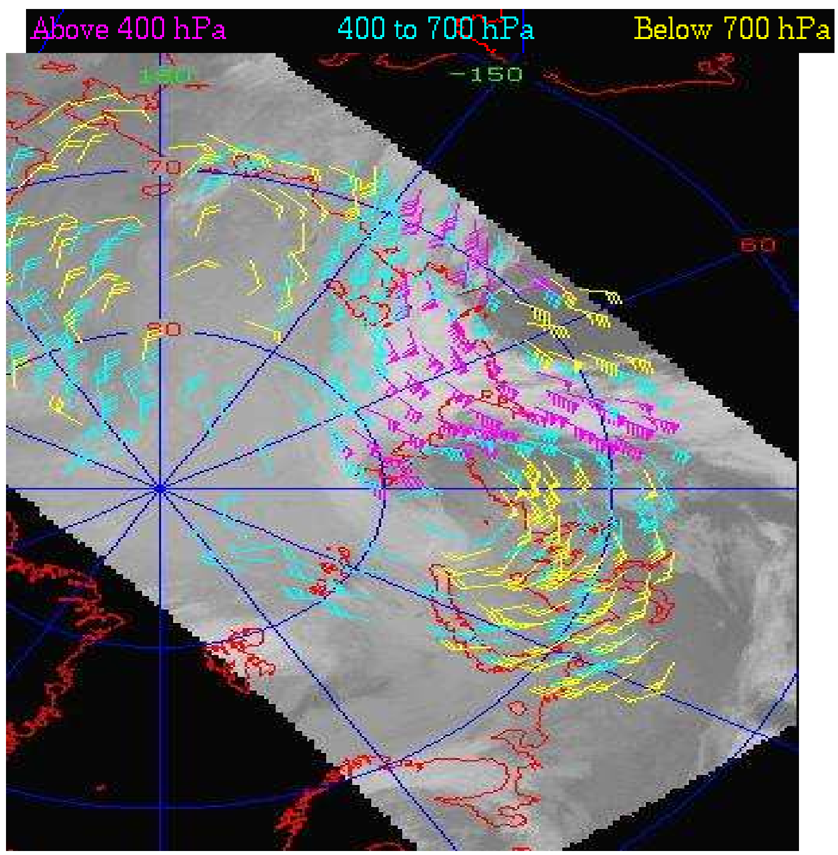

Figure 12. An example AVHRR image with the upper level wind vectors above 400 hPa are associated with flow over a ridge. Also, bright white IR returns are indication of higher (colder) cloud tops over North-Central Russian coast in flow over a ridge, downstream of the trough.

a)

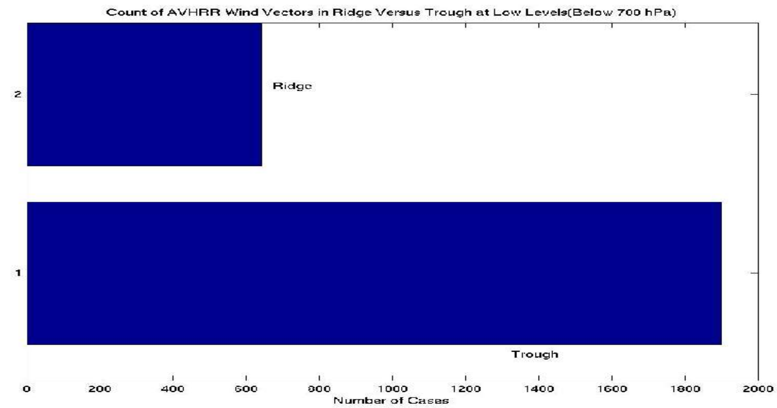

b)

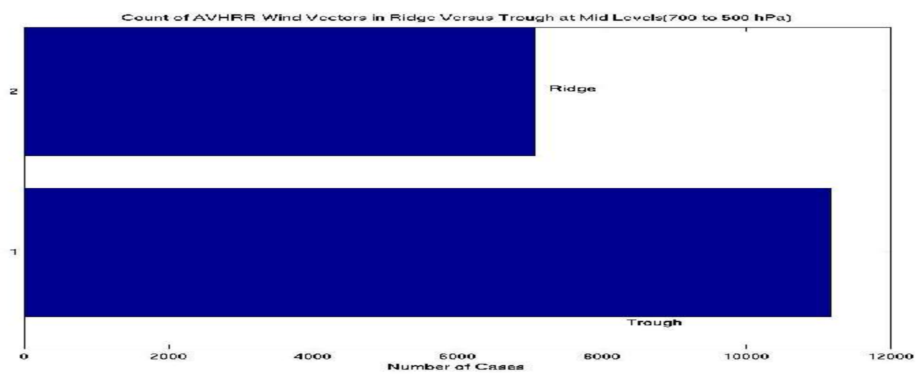

c)

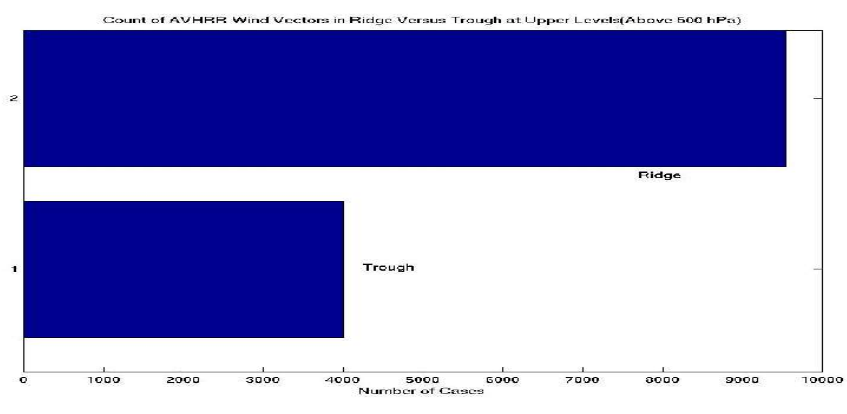

Figure 13. Histogram plot of the number of cases of AVHRR CMVs that occur in either a ridge or trough, with relative vorticity greater than + 4 x 10^{-5} denoting a trough and less than – 4 x 10^{-5} denoting a ridge. a) Below 700 hPa. b) 700 to 500 hPa. c) Above 500 hPa.

a)

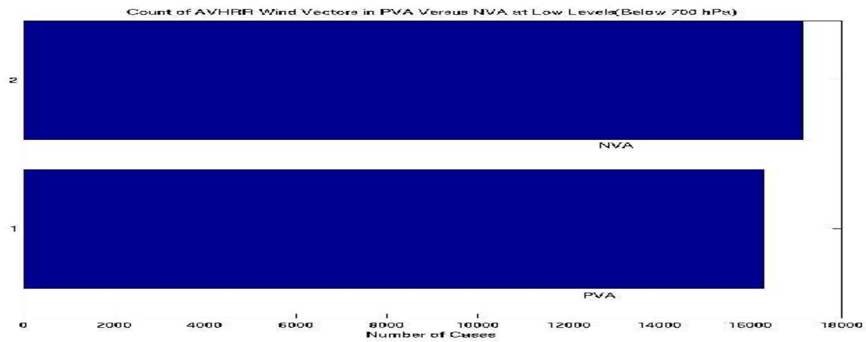

b)

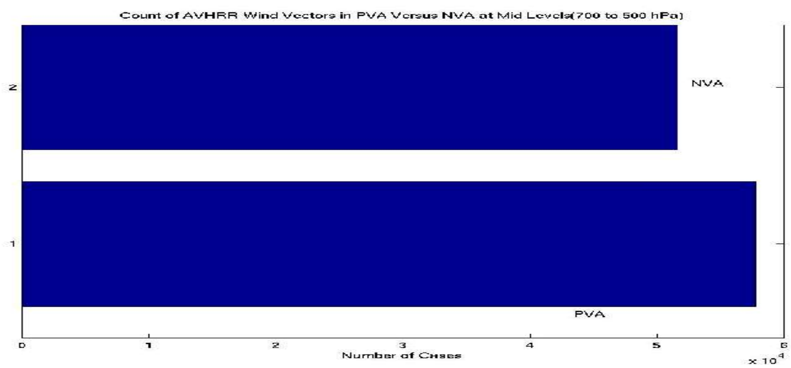

c)

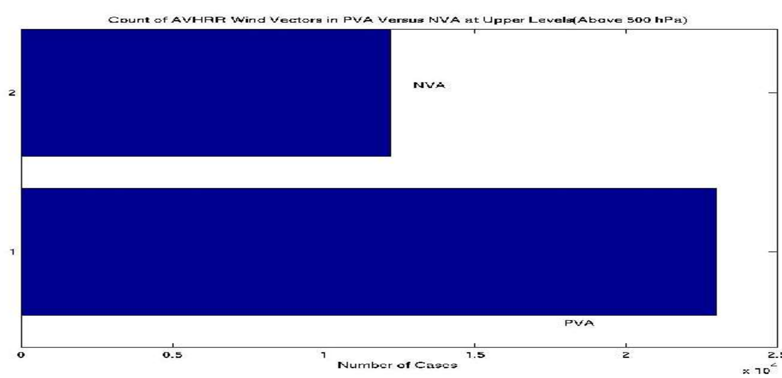

Figure 14. Histogram plot of the number of cases of AVHRR CMVs that occur in either Positive Vorticity Advection (downstream of trough axis and upstream of ridge axis) or Negative Vorticity Advection (downstream of ridge axis and upstream of trough axis) a) Below 700 hPa. b) 700 to 500 hPa. c) Above 500 hPa.

a)

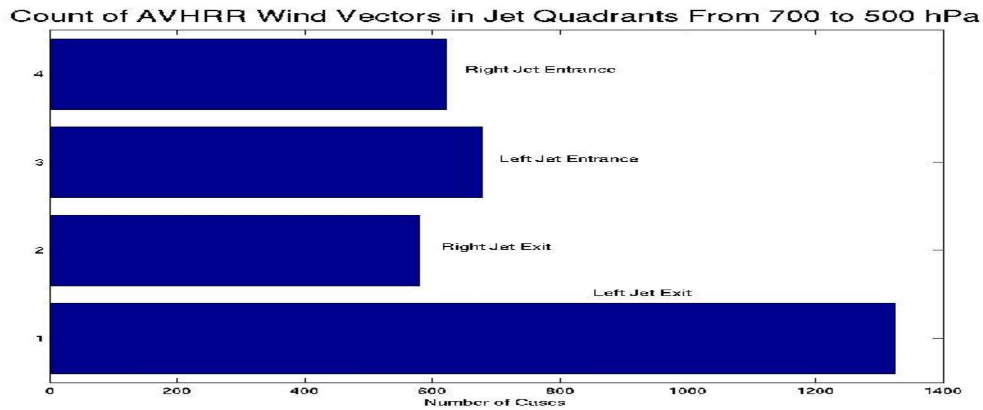

b)

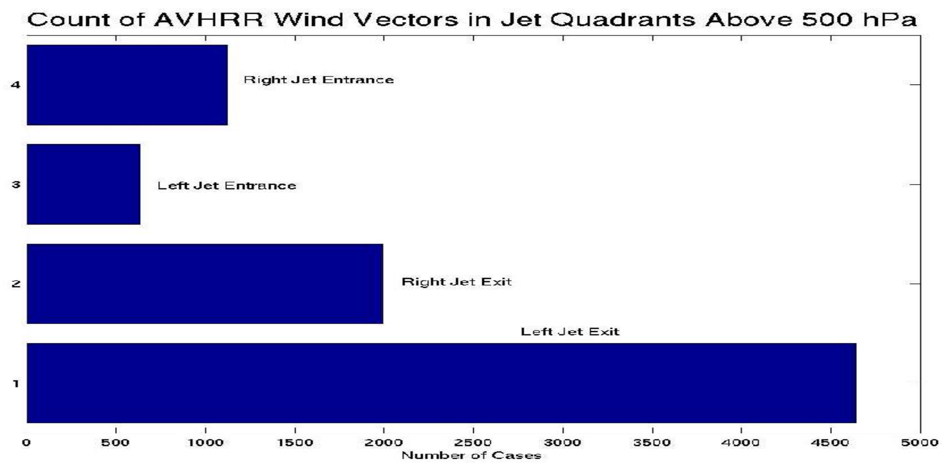

Figure 15. Histogram plot of the number of cases of AVHRR CMVs that occur in each of the four jet streak quadrants. The left jet exit (right jet exit) region is determined to be in areas where the gradient of the wind speed is less than -.35 m/s per km along the isoheight lines and in PVA (NVA). The left jet entrance (right jet entrance) is determined to be in areas where the gradient of the wind speed in greater than +.35 m/s per km along isoheight lines and in NVA (PVA). a) 700 to 500 hPa. b) Above 500 hPa.

a)

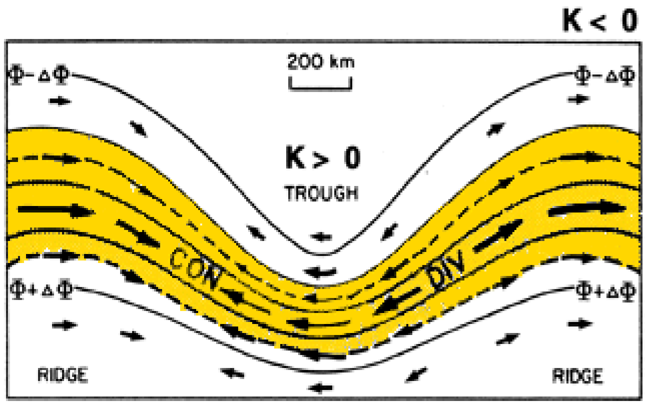

b)

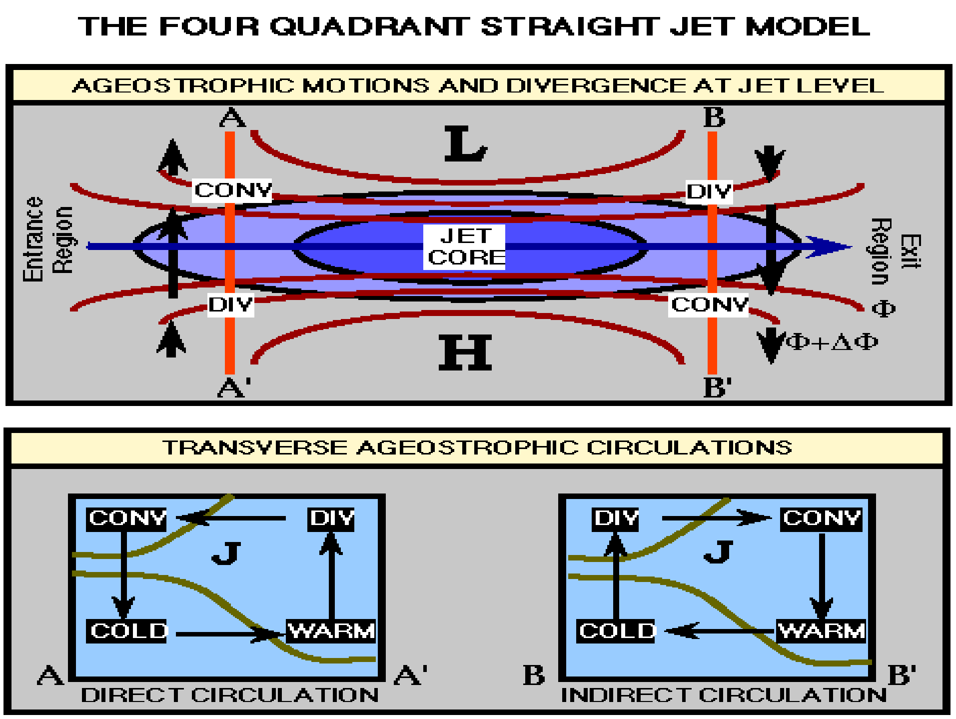

Figure 16. a) A typical flow pattern of the ageostrophic wind (black arrows) parallel to the geopotential height lines (black lines) in a curved westerly jet (yellow) embedded in a highly amplified atmospheric wave. b) A typical ageostrophic flow, divergence, convergence and vertical circulation patterns associated in the entrance and exit regions of jet streaks.

7-2. Individual Case Studies

Next, interesting case studies near synoptic analysis periods (00, 06 , 12 and 18 UTC) during a four month period (March through May 1992 and May through June 1995). Case studies are investigated to look at possible areas at which the ERA-40 re-analysis had inaccurate wind fields when compared to AVHRR and the inertial advective component of the ageostrophic wind. The inertial advective component of the ageostrophic wind is the right hand most term in brackets in equation 22, which represents the advection of geostrophic wind by itself.

$$\mathbf{V_a} = 1/f_o\, \mathbf{k} \times D\mathbf{Vg}/Dt = 1/f_o[\mathbf{k} \times \partial \mathbf{Vg}/\partial t + \mathbf{k} \times (\mathbf{Vg} \cdot \nabla)\mathbf{Vg}] \quad (22)$$

For the most part, it is the dominant term in the ageostrophic wind equation derived from quasi-geostrophic momentum equation in the vicinity of jets and regions of sharply curved flow (Holton 92, Bluestein 92). However, the isallobaric term (left most term in brackets in equation 22), which is the wind velocity resulting from changes of pressure or geopotential height over time (isobaric or geopotential tendency) and is proportional to the isallobaric gradient, can have a significant contribution across the continental polar front, where the isallobaric gradient is large (Wexler, 1937) and at lower levels where both terms are of nearly equal magnitude (Holton, 1992). The figures 17-24 (below) show point measurements of the speed, direction, or vector difference above 500 hPa within 3 hours of the analysis time, and an overlay of geopotential height (solid black lines) and inertial advective term of ageostrophic wind (colored dashed lines) at 400 hPa. Speed or vector differences are calculated by temporal and vertical interpolation of ERA40 wind vectors to the time and vertical pressure level of AVHRR wind vector, if they are within 25 km and 50 hPa of each other.

The first case occurs on June 8th and 9th, 1995 over north-central Russia, a region void of rawinsonde data (Figure 2). Over this region at 18 UTC June 8th, there is a relatively larger vector difference between AVHRR and ERA-40 wind fields (circled in Figure 17), in a significant diffluence zone coming out of a jet exit region, downstream of a negatively tilted trough, associated with highly curved flow and large values of Inertial Advective Term (IAT) of the ageostrophic wind (13 to 25 m/s). The mesoscale larger differences between the fields is in a highly ageostrophic flow and is particularly in a region of larger gradient of IAT along the geopotential height lines downstream of the trough. The speed differences on average with overall variability (-1 to -7 m/s speed differences) are slower (Figures 17c and d). The direction differences are positive (AVHRR wind direction clockwise of ERA-40) by 20 to 40 degrees (Figures 17e and f). This implies that AVHRR has a more clockwise flow and is on average slower compared to ERA-40 in the region of noticeably higher vector differences. In addition, AVHRR is faster than ERA-40 near the downstream ridge axis at both times and faster downstream of the trough axis at 00 UTC on June 9th where IAT values are also quite large (Figures 17c and d).

The second case study occurred on 00 and 06 UTC on May 10th, 1992 over the Barents Sea, another region void of rawinsonde data. During these times, there is a negative tilted shortwave trough that is moving northward and a jet stream south of the shortwave trough along the northwest Russian coast pushing into a ridge over central Russia and Kara

Sea. During the two time periods AVHRR is slower (up to -6 m/s difference in spots) than ERA-40 in a diffluence zone southeast of Novaya Zemlya in the Kara Sea and in the shortwave trough north of Novaya Zemlya in the Barents Sea at 06 UTC and upstream of the ridge axis and downstream of the jet exit region in the eastern Nansen Basin (Figures 18c and d). There is a counter-clockwise direction difference of 10 to 20 degrees at 06 UTC, south of the northeast end of Novaya Zemlya. This means that AVHRR has more cyclonic curvature and diffluence in that particular region (Figure 18f). Overall, AVHRR wind vector differences are locally larger in magnitude near and along the shortwave trough axis at 06 UTC (Figure 18b). A slower AVHRR wind in comparison to the ERA-40 in the diffluence zone, implies that AVHRR has a greater deceleration of the wind speed. In addition, the slower AVHRR wind speeds compared ERA-40 at 0600 UTC in the shortwave trough implies that either geopotential height gradient is too strong or is under-estimating the ageostrophic component of wind (Figure 16a).

The third case study occurs on 00 and 06 UTC May 16th and 00 UTC May 17th, 1992 (Figures 19a-e). On these dates and times NOAA-11 made overpasses over a progressive shortwave trough that was amplifying during the period over central-northeast Russia. The upstream ridge was deamplifying, while the downstream ridge amplified during the period. AVHRR upper level wind vectors occurred in the upstream and downstream ridges and in association with the jet exit regions. Notably, is the dominant opposing signs of speed difference in each jet exit into shortwave ridge regions (Figure 19a). In the downstream shortwave ridge and associated jet exit region, the AVHRR wind speeds are primarily faster than the ERA-40 wind speeds. However, near the upstream ridge in the associated jet exit region, the AVHRR wind speeds are primarily slower than ERA-40, with the exception of the diffluent zone in the left jet exit region just downstream of a shortwave trough. In this case, AVHRR has on average more deceleration of the wind field upstream of the trough while slower deceleration downstream of the trough. Nothing of significance appears in the vector differences upstream of the trough. However, downstream of the trough the vector differences are primarily are of larger magnitude (Figure 19b). With respect to the direction difference analysis, nothing seems to be significant until 00 UTC on May 18th, when there are significant direction differences in the vicinity of the shortwave trough (Figure 19e) and AVHRR is on average faster downstream of the trough (Figure 19d). While AVHRR is significantly more clockwise in the trough, it is more counter-clockwise farther to the north and east (Figure 19e). This could be indication of the ERA-40 misplacing the shortwave trough farther west.

The fourth case study occurs over 18 and 00 UTC periods of April 4th and 5th, 1992 over the Chukchi sea into Alaska (Figures 20a-d). During this time, a highly amplified ridge over the the Chukchi sea goes through an unusual deamplification, or wave breaking, over a 12 hour period. On April 4th, a jet is wrapping around a negatively tilted trough over the northeast Russian coast with rapid deformation, or diffluence, into a highly amplified ridge over the Chukchi Sea. In the curved jet exit region, AVHRR wind speeds are relatively slower than ERA-40. However, in the diffluent zone north of the negative tilted trough, the AVHRR winds are much faster and more clockwise, while farther south, near the negative tilted trough the AVHRR vector directions are more counter-clockwise than the ERA-40 (Figures 20a and c). This could mean that in the encircled regions in Figures 20c and a, that the deformation or diffluence is underestimated in the ERA-40 wind field and that the deceleration of the wind speed is underestimated by the ERA-40 in the jet exit region flow into the amplified ridge and overestimated in the diffluence zone north of the trough. The next time NOAA-11 makes an overpass of the same region, the wave has finished a 12 hour wave breaking process. The result is a shortwave trough embedded in the jet flow over the Bering Strait with relatively large IAT of greater than 12 m/s in the shortwave trough and greater than 9 m/s in the jet exit region. Plots of speed and direction difference show a bullseye mesoscale region of significantly faster AVHRR winds speeds (4 to 5 m/s) and counter-clockwise direction difference (up to 40 degrees) compared to ERA-40 (Figures 20b and d). This could be indication of an unresolved shortwave trough, or the ERA40 not having the shortwave trough north of the Bering strait extending farther south and east. In addition, there is some underestimation of the speed shear across the jet exit region, as there is a noticeable slower speed difference in the right jet exit region (Figure 20d).

The fifth case study occurs over the Laptev Sea coast on 1800 UTC June 20th and 00 UTC on June 21st, 1995 (Figures 21a-d). A jet exit region is moving over the area with IAT values in the 3 to 10 m/s. The AVHRR winds are for the most part faster than ERA-40 in the flow around the ridge by 2 to 6 m/s and slower than ERA-40 in the jet exit region by -2 to -6 m/s (Figures 21a and b). The slower speeds in the jet exit could be the result of the ERA-40 underestimating the deceleration of the wind coming out of the jet. In addition, at 18 UTC especially, the AVHRR wind vectors are predominantly more clockwise in direction than the ERA-40 in the right jet exit region (Figures 21c and d), and the AVHRR wind have more cyclonic shear (Figures 20c and d) in the the far left jet exit region. More anticyclonic shear in the right jet exit region and cyclonic shear in the far left jet exit region could be due to the sharpness of flow on the northeastern side of the shortwave trough over the Laptev Sea and in the ridge along the coast being analyzed incorrectly by the ERA-40 wind field. In addition, there is a noticeable counter-clockwise next to clockwise difference in the flow over the New Siberian Islands on 18 UTC June 20th, that is probably an indication that ERA-40 could be under-analyzing the sharpness of the flow over ridge at that location (Figure 21c) .

The sixth case study occurs on May 13th, 1995 from 1200 to 1800 UTC over the Canadian Archipelago, Baffin Bay and Greenland. As seen in Figures 22a-c, there is a well defined upper level cyclone over the Canadian Archipelago and downstream ridge over Greenland. On the cyclonic shear side of the jet and east of the cyclone is significant curvature of the flow that is resulting in the large IAT values up to 27 m/s. There are noticeable mesoscale speed difference patterns in Figures 22a and b. First, is a region of faster wind speeds for the AVHRR over Baffin bay on the negative vorticity advection side of the jet. Second, small scale areas of primarily slower wind speeds observed by AVHRR (4 to 6 m/s slower) on the northeast side of the cyclone center, with an area of faster speed differences (2 to 4 m/s faster) in the region of diffluent flow farther to the north and east of the low, and downstream of the jet. Third, there is a region of faster and slower wind speeds (+/- 5m/s) downstream of the local maximum in IAT, over Baffin Island at 12 and 18 UTC.

Fourth, there is a higher frequency of slower wind speeds observed by AVHRR along the ridge and downstream of the ridge axis over western Greenland Coast into northern Baffin Bay. Less observable patterns are in the direction difference field, except near the ridge over west-central Greenland coast, where AVHRR is much more clockwise in direction than ERA-40 (Figure 22c). This could be due to the ERA-40 locally misplacing the ridge axis. For the most part the direction differences are relatively small and variable in sign near the cyclone, with the AVHRR minus ERA-40 direction differences under + or – 20 degrees, as seen in Figures 22c and d. This case study reinforces the mesoscale nature of the differences between the AVHRR and ERA-40 wind fields. Possible reasons behind the mesoscale nature of the differences are small scale features observed by AVHRR that are being filtered out due to smoothing of the wind field by the re-analysis, or mesoscale features in the geopotential height field being inaccurately represented by the re-analysis that result in mesoscale inaccuracies in the wind field, or possible deficiencies in the AVHRR wind derivation techniques that are a result of erroneous tracking of features in the infrared channel or errors in height assignments of the wind vectors. However, it has been shown through collocation comparison of winds from rawinsondes not assimilated into the reanalysis, that AVHRR does have smaller mean errors of wind speed compared to ERA-40.

The seventh case study occurs on June 18th, 1995 at 12 and 18 UTC over the Beaufort Sea (Figures 23a-d). In this case study there is an amplified ridge over the eastern Beaufort Sea with IAT speeds of over 9 m/s at and near the ridge axis. At 12 and 18 UTC on June 18th, 1995 there are noticeable slower speed differences at the local maximum in the IAT. The

AVHRR wind speeds near and at the ridge axis are slower than that analyzed by the ERA-40 (Figures 23a and b) . This is a case where the ERA-40 analysis could be over-estimating the ageostrophic component of the wind in a region of curved flow in an amplified ridge (Figure 16a). In addition, there are noticeable larger counter-clockwise direction differences north and west of the region of maximum IAT at 12 UTC, and very noticeable in a upstream shortwave trough at 18 UTC (Figures 23c and d). At 12 UTC, the larger counter-clockwise direction differences of 30 to 40 degrees near the ridge apex, is an indication that the ridge apex is displaced too far to the west in ERA-40 when compared to AVHRR. At 18 UTC the large direction differences in the upstream shortwave trough is likely an indication that the shortwave trough in ERA-40 is either misplaced or over-amplified when compared to the AVHRR wind field.

The final case occurs on May 4th, 1992 at 06 and 12 UTC (Figure 24a-d). On this day there is an amplifying negative tilted wave over Greenland into the GIN (Greenland/Iceland seas. The AVHRR cloud motion vectors occur downstream of the trough axis and upstream of the ridge axis. In this region, the IAT is for the most part less than 5 m/s, however, there are relatively large speed differences over the region. At both times, there are speed differences larger than 3 m/s, with AVHRR being predominantly slower than ERA-40 over east-central Greenland (Figures 24a and b). Interestingly, there is a RAOB station in the middle of the larger slower speed differences at Scoresbysund, Greenland, but according to IGRA there were no RAOB observations and therefore, no wind data to be assimilated into re-analysis at those times. Even though there are many significant speed differences that occur in regions of small IAT speeds, there are areas of larger speed differences that due occur in larger IAT speeds of greater than 5 m/s. For example, in the jet exit region over the GIN seas during both analysis times are larger faster speed differences in the jet exit, with a sign transition to predominantly slower speed differences in the left jet exit and along to just upstream of the negatively tilted ridge axis across central Greenland and the east-central coast. There is another noticeable transition at 12 UTC over central Greenland, downstream of the trough and upstream of the ridge, where AVHRR is predominantly faster than ERA-40. In addition, there are also some relatively larger (> 10 deg) direction differences over the same areas where large speed differences occur. AVHRR is predominantly more clockwise in direction in the jet exit regions and counter-clockwise over Greenland Sea and east-central coast, and mixture of larger clockwise and counter-clockwise differences over interior Greenland (Figures 24c and d).

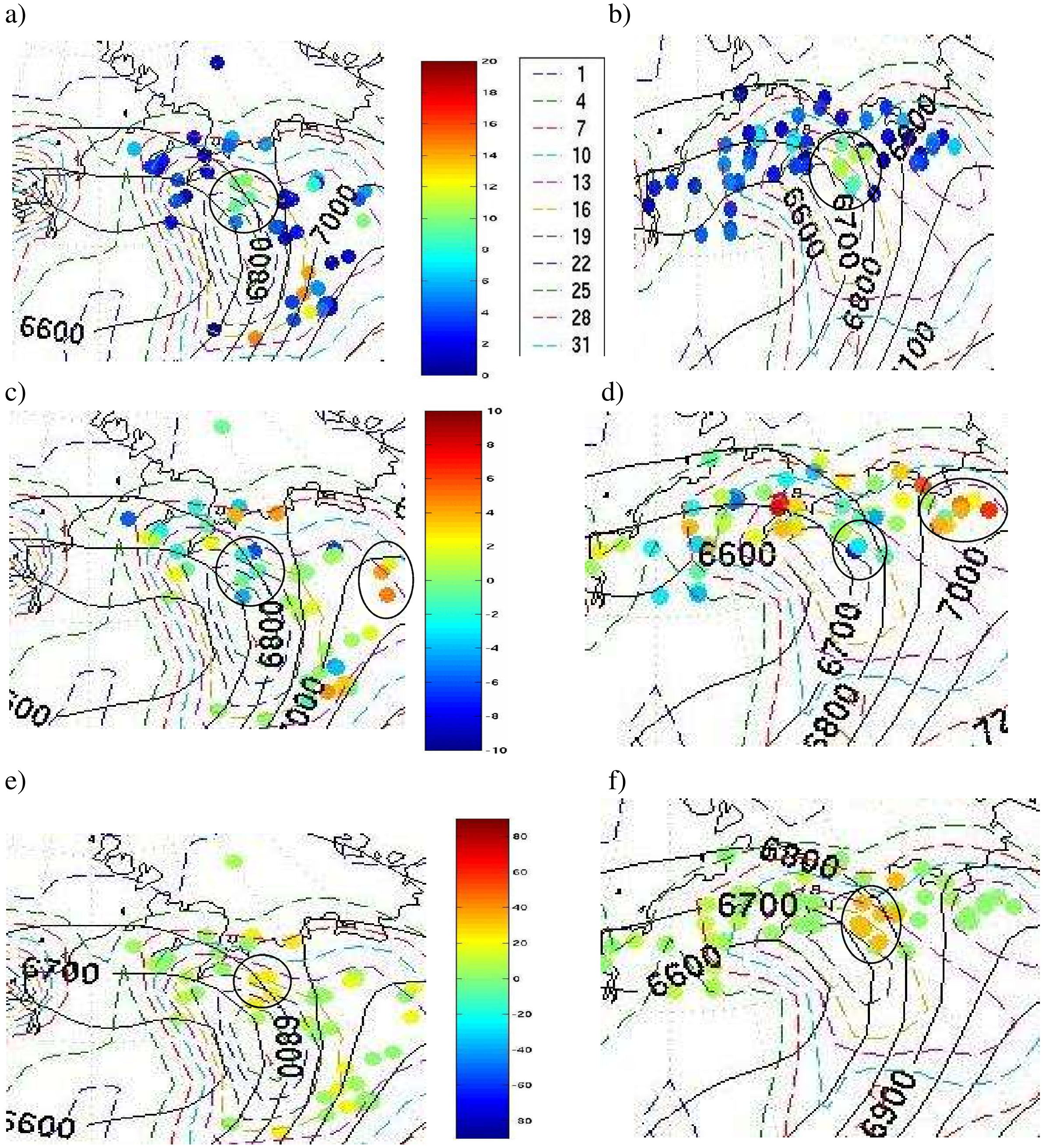

Figure 17. Case # 1, a) Plot on the left is at 1800 Z June 8, 1995. b) Plot on the right is at 0Z June 9, 1995. Plots of Geopotential height (solid lines) at 400 hPa, Inertial Advective Component of the ageostrophic wind ($1/f_o\mathbf{k} \times [\mathbf{k} \times (Vg\cdot\nabla)Vg]$) in dashed lines and vector difference (dots) in a and b. Speed difference (dots) in c and d. Direction differences (dots) in e and f. Legend on the top left is the absolute magnitude of the vector difference in m/s. The Legend on the right is the magnitude of the Inertial Advective term in m/s.

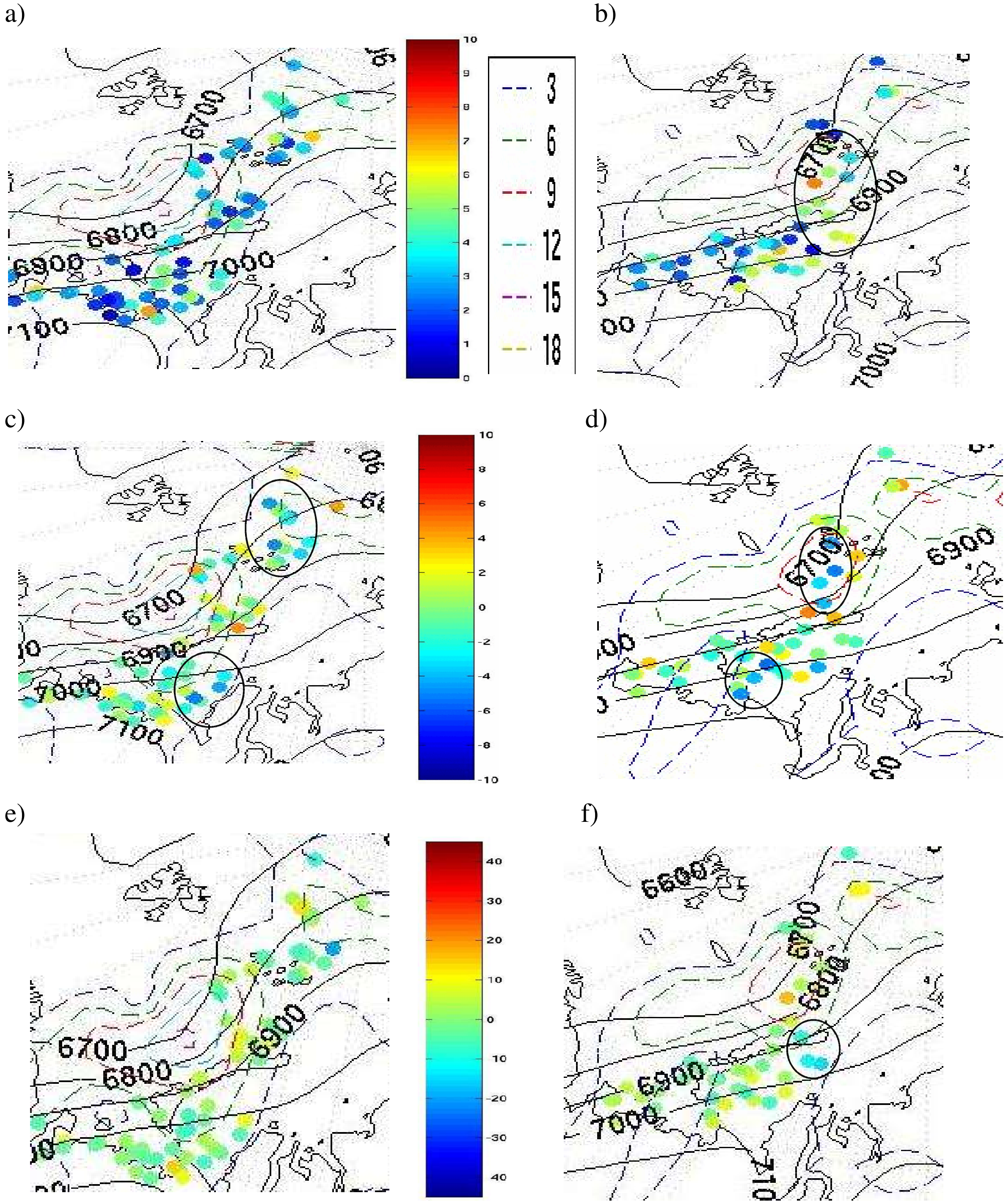

Figure 18. Case # 2, plots on the left are at 00 Z May 10, 1992. Plots on the right are at 06Z May 10, 1992. Again plots of geopotential height (solid lines) at 400 hPa and the Inertial Advective Component of the ageostrophic wind (dashed lines). Plots a and b are vector differences (dots). Plots c and d are speed differences Plots e and f are direction differences.

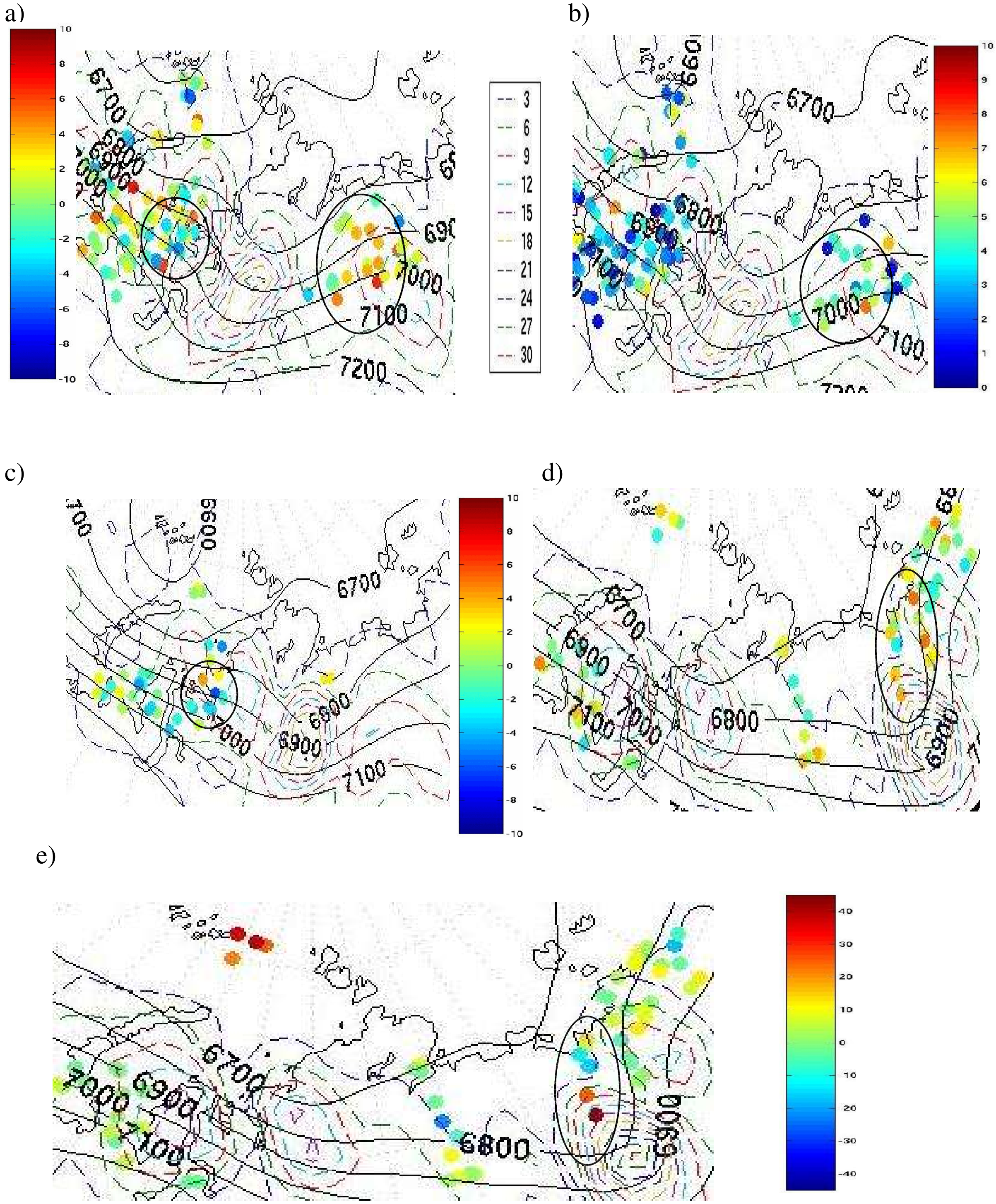

Figure 19. Plots for Case # 3. a) 00 Z May 16, 1992 speed differences. b) 00 Z May 16, 1992 vector differences. c) 06 Z May 16, 1992 speed differences. d) 00 Z May 17, 1992 speed differences. e) 00 Z May 17, 1992 direction differences .

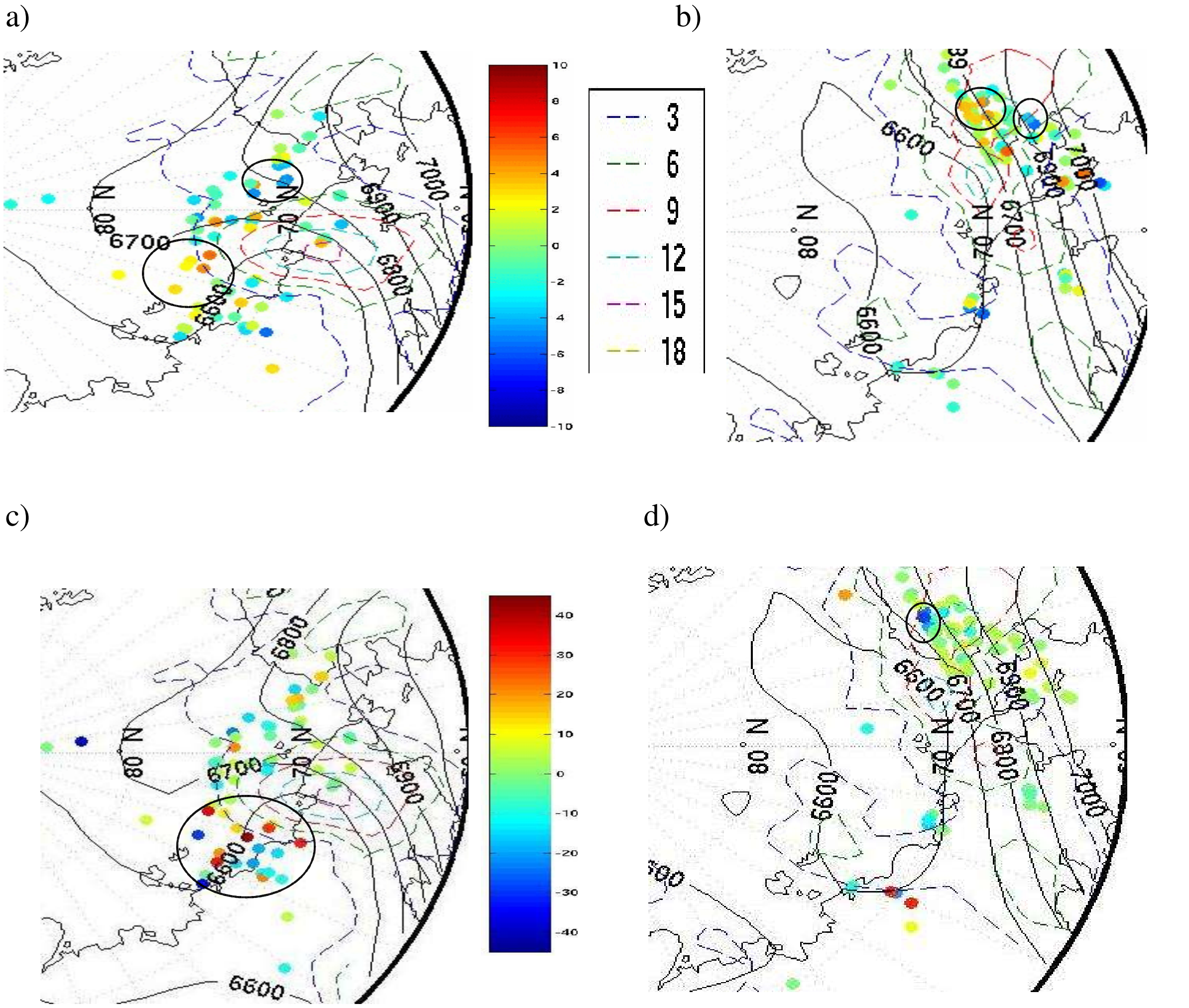

Figure 20. Plots for Case # 4. a) 18 Z April 4, 1992 speed differences. b) Speed differences at 18 Z April 5, 1992. c) Direction differences at 18 Z April 4, 1992. d) Direction differences at 18 Z April 5, 1992.

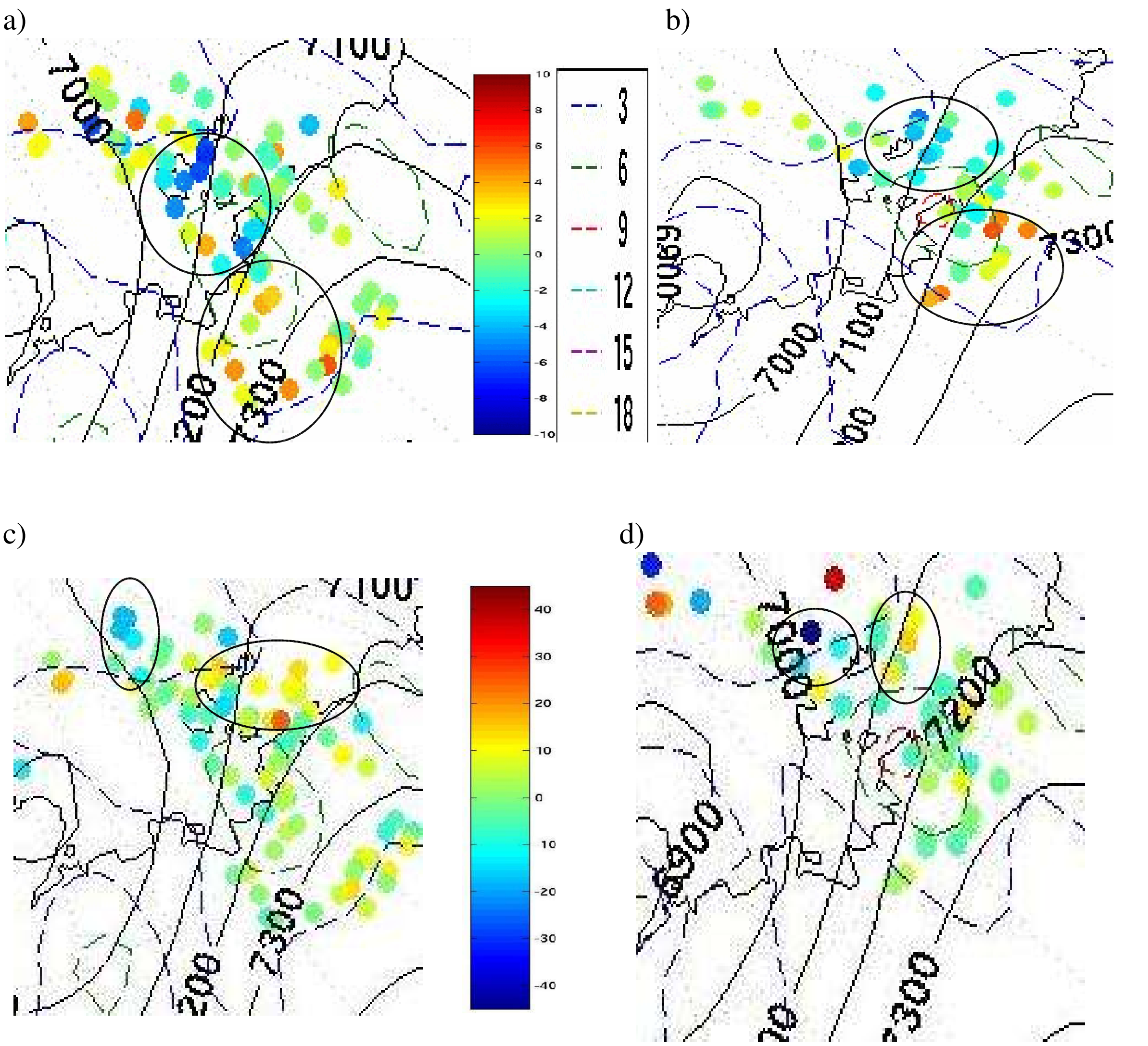

Figure 21. Plots for Case # 5. a) 18 Z June 20, 1995 speed differences. b) Speed differences at 00 Z June 21, 1995. c) Direction differences at 18 Z June 20, 1995. d) Direction differences at 00 Z June 21, 1995.

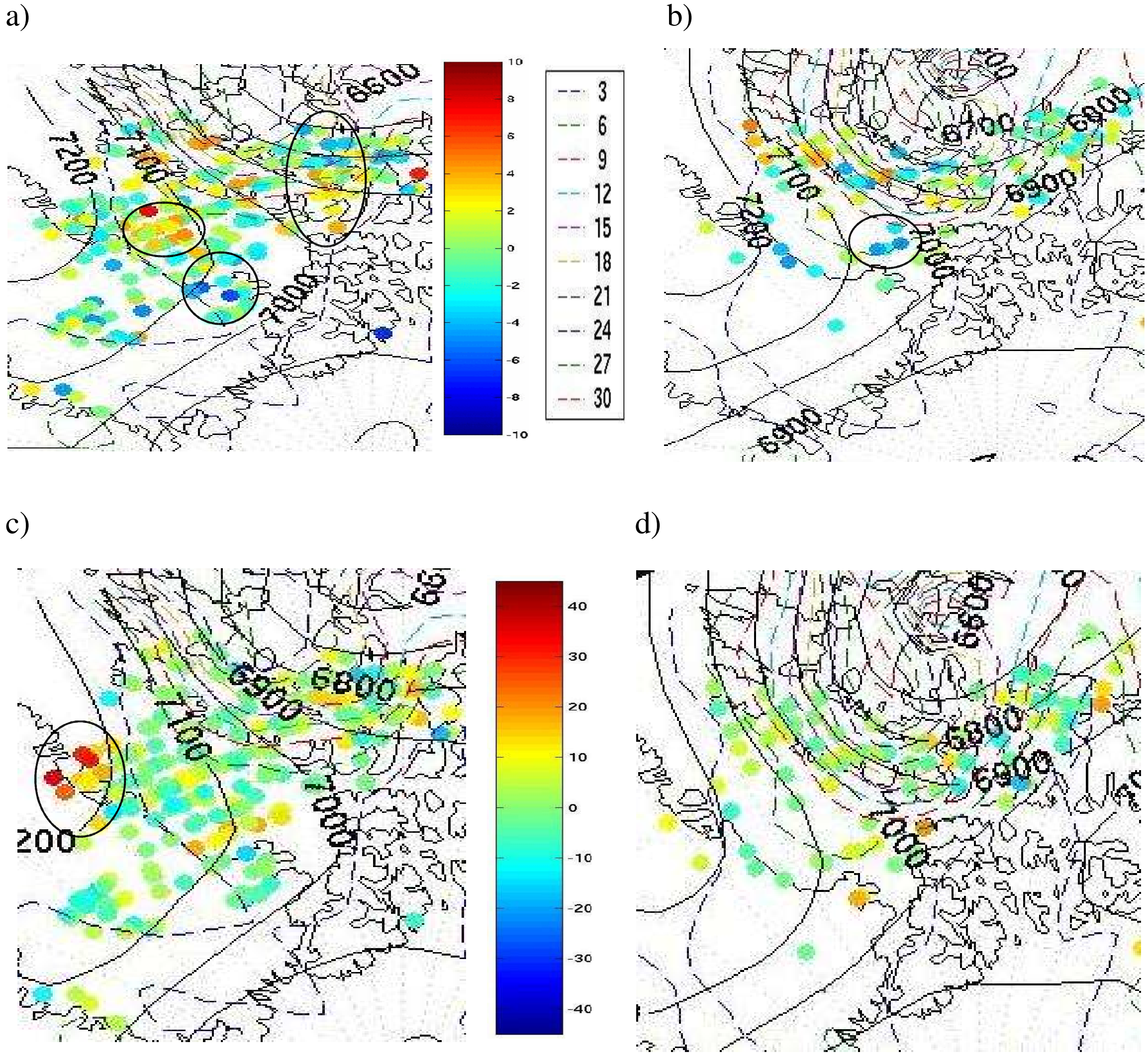

Figure 22. Plots for Case # 6. a) 12 Z May 13, 1995 speed differences. b) Speed differences at 18 Z May 13, 1995. c) Direction differences at 12 Z May 13, 1995. d) Direction differences at 18 Z May 13, 1995.

a) b)

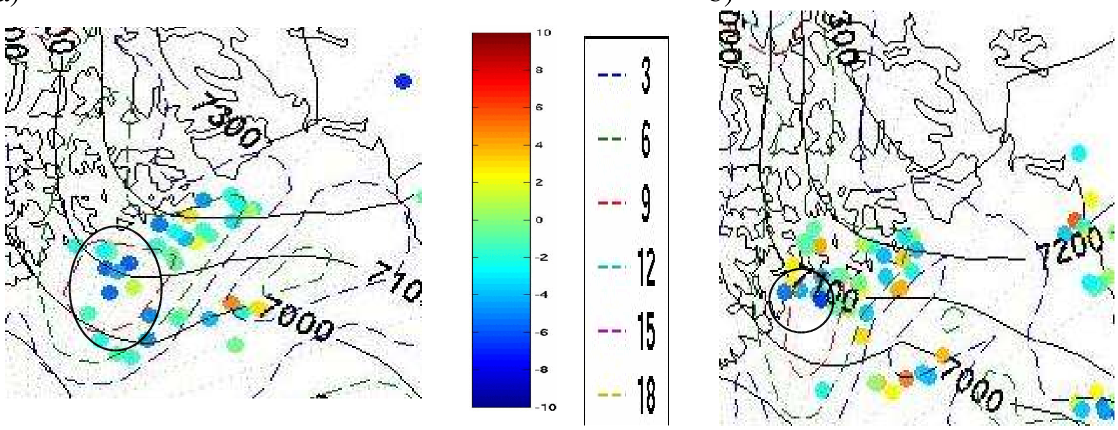

c) d)

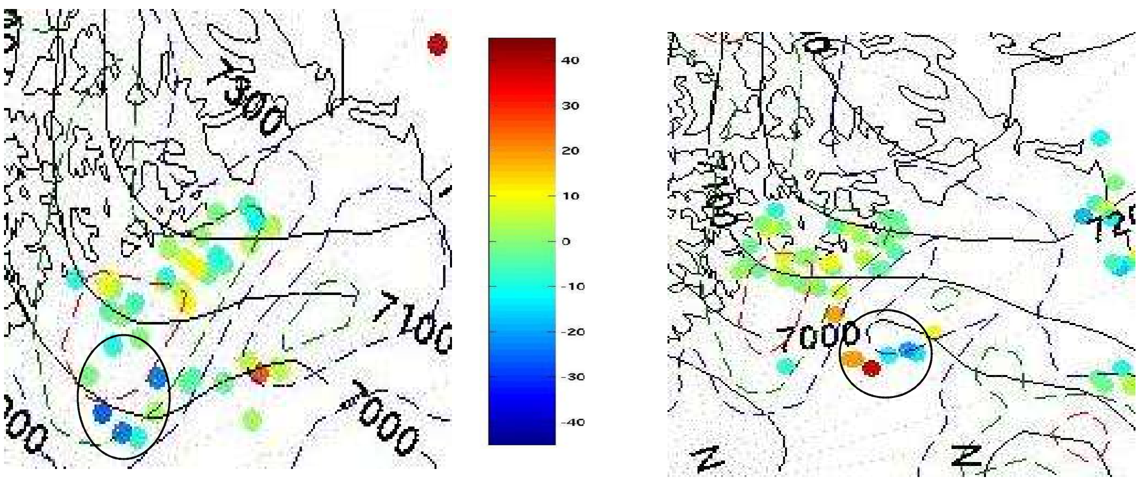

Figure 23. Plots for Case # 7. a) 12 Z June 18, 1995 speed differences. b) Speed differences at 18 Z June 18, 1995. c) Direction differences at 12 Z June 18 1995. d) Direction differences at 18 Z June 18, 1995.

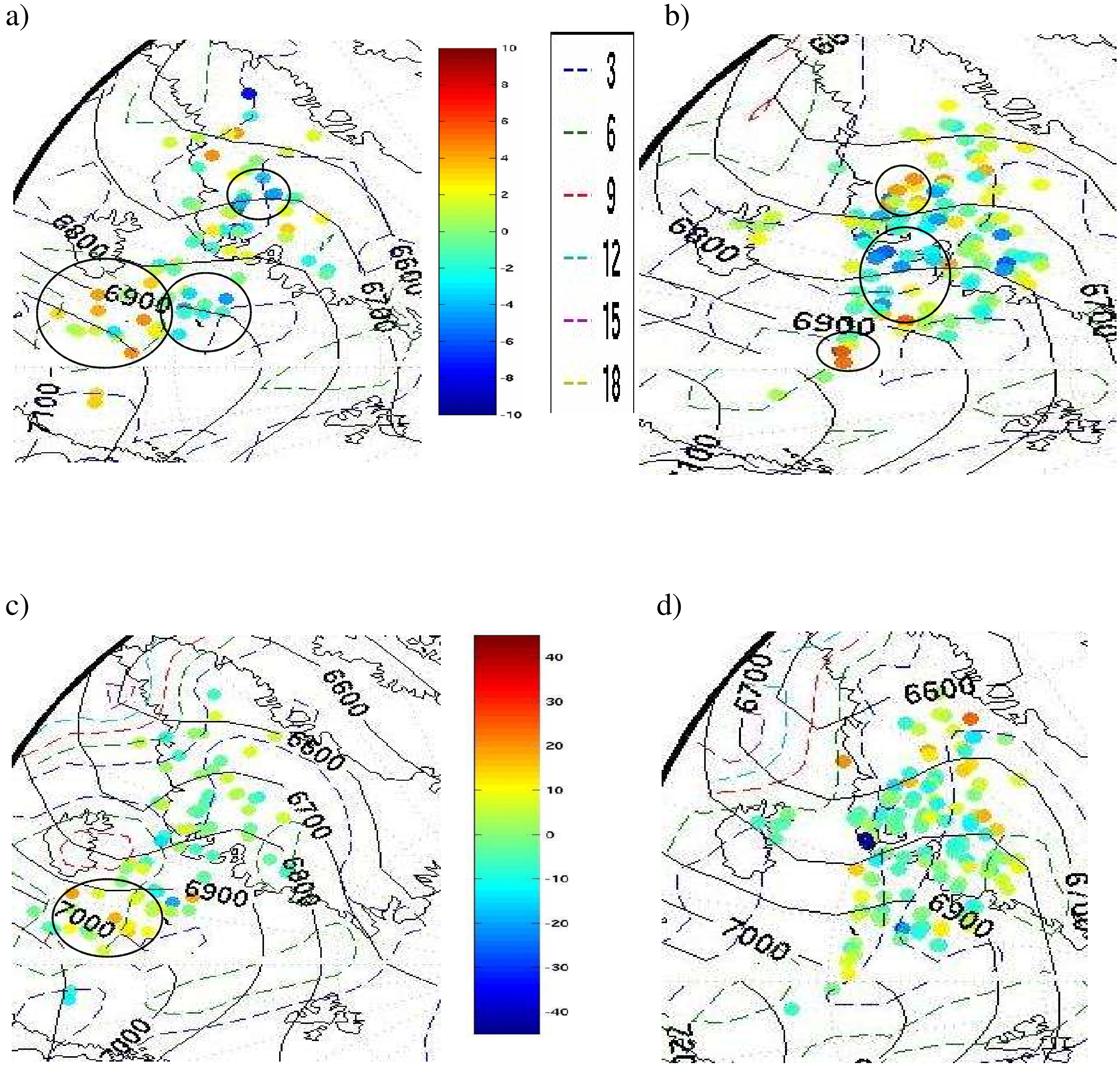

Figure 24. Plots for Case # 8. a) 06 Z May 4, 1992 speed differences. b) Speed differences at 12 Z May 4, 1992. c) Direction differences at 06 Z May 4, 1992. d) Direction differences at 06 Z May 4, 1992.

7-3. Similarities Between Cases

The cases studies shown above indicate common atmospheric flow patterns that tend to produce larger differences (i.e., 4 m/s or greater in speed difference) between AVHRR and ERA-40. The common atmospheric flow patterns at upper levels (400 hPa) that produces significant differences above the level of non-divergence (500 hPa) is in jet exit regions, in regions of flow curvature, and in amplified waves, with the larger differences sometimes located near regions of local maximum in the inertial advective term of the ageostrophic flow. A few examples of this given in the case studies above are 18 UTC June 8th to 0 UTC June 9th, 1995 (Figure 17) over north-central Russia in a left jet region into the base of a negatively tilted trough with cyclonic curvature, 06 UTC May 10th, 1992 (Figure 18) north of Novaya Zemlya over the Barents sea associated with a cyclonic curvature in a shortwave trough in the left jet exit region, June 18th, 1995 at 12 and 18 UTC (Figure 21) in strong anticyclonic curvature around a ridge axis associated with a maximum in the IAT speed and 18 UTC April 5, 1992 (Figure 20) over northwest Alaska in the left jet exit region also associated with a maximum in IAT speed. There are significant speed, direction or vector differences between ERA-40 and AVHRR in the left jet exit region or associated centripetal acceleration in a shortwave trough or ridge.

Shapiro and Kennedy (1981) discuss the importance of ageostrophic motions to atmospheric dynamics and caution the use of geostrophic momentum approximation to jet-streak systems in large-amplitude synoptic wave regimes. With numerous significant smaller scale differences being seen in regions of amplified waves (i.e., Figures 17a and b, Figures 22a-c, Figures 23a-c and Figures 24a-d), it is possible that the reanalysis is unable to correctly capture the ageostrophic motions involved in producing the actual wind. Therefore, the ageostrophic velocity parallel to lines of equal geopotential heights (isoheights) were calculated (equation 23), to determine whether there is any relationship between the magnitude of ageostrophic wind speed in the AVHRR AMVs and speed differences between ERA-40 and AVHRR.

$$\mathbf{V_a} = (\mathrm{VAVHRR} - \mathrm{Vg}) \quad (23)$$

The ageostrophic wind component parallel to isoheights was determined from the AVHRR wind vector value parallel to the height field minus the geostrophic wind (equation 23). However, results found no obvious relationship between the magnitude of the ageostrophic term parallel to isoheight lines and the magnitude of the speed or vector difference .

One possible reasoning to differences observed between AVHRR and ERA-40 is the underestimation of the ageostrophic motions in the vicinity of the jet exit and entrance regions. There could also be an underestimation of ageostrophic motions in the vicinity of significant flow curvature. In regions of significant flow curvature or jet entrance and exit regions, the inertial advection wind component, the advective term in (equation 22, second term in brackets) the total ageostrophic wind vector given by quasi-geostrophic momentum equation (equation 24) is significant.

$$\mathbf{Dvg/Dt} = -f_o\, \mathbf{k \times Va} - \beta y \mathbf{k \times Vg} \quad (24)$$

In the jet entrance regions, the geostrophic flow is accelerating due to rapidly increased pressure gradient forcing into the jet streak. In the jet exit region the geostrophic flow is significantly decelerating due to rapidly decreasing pressure gradient forcing. In areas of curvature, the atmospheric flow goes through increased centripetal acceleration that can lead to ageostrophic wind speeds in rare cases in excess of 80 m/s near the trough axis with very strong jet streaks that are embedded in the trough (Shapiro and Kennedy 81). Figure 16a shows a typical ageostrophic flow parallel to geopotential height lines in a jet moving through an amplified wave pattern. This indicates that the highest velocities of the ageostrophic winds are located near the ridge axes, where they are in the same direction as the geostrophic flow, and near the trough axis, where they are in opposition to the geostrophic flow (Figure 16a, from equations 24 and 25). Due to the limited temporal and spatial resolution of the observing network over the Arctic and Antarctic, there are likely to be mesoscale ageostrophic motions that are missed by the reanalysis. These mesoscale ageostrophic motions are unable to be accurately calculated through the assimilation process, because of simplifications made using quasi-geostrophic assumptions in data void regions that could result in small scale regions of the wind flow that underestimate or overestimate the ageostrophic component of the wind. In addition, there could be small scale regions where the geostrophic balance given by the geopotential height gradient is overestimated or underestimated. Moreover, over data void regions the geopotential height field could be inaccurate, leading to inaccurate geopotential height gradients that would cause the calculated geostrophic wind to be incorrect.

7-4. Comparison to the Kinematic Flow type

Speed and direction differences between AVHRR and ERA-40 were compared to where they were located in the atmospheric flow (i.e., trough versus ridge, jet entrance versus exit) to determine if there were any particular biases with respect to the atmospheric flow field. A wind vector was determined to occur in a ridge or anticyclone (cyclone or trough) if the relative vorticity was negative (positive), or if the u and v geostrophic wind components were in the same (opposite) sign as the u and v ageostrophic wind components (Figure 16a, from equations 24 and 25). A wind vector was determined to be in a jet streak if the wind speed was greater than 25 m/s, and in a jet exit (entrance) if the gradient of the wind speed was less (greater) than -.35 m/s per kilometer (+.35 m/s per kilometer). Moreover, speed and direction differences where compared among quadrants of the jet streak. A wind vector was determine to be in the left (right) jet exit if the gradient was below the given threshold (-.35 m/s per kilometer) and the sign of vorticity advection (equation 21) was positive (negative). A wind vector was determine to be in the left (right) jet entrance region when the gradient was above the given threshold (+.35 m/s per kilometer) and the sign of negative (positive).

Long term (4 months period March to May 1992 and May to July 1995) investigation between differences of the AVHRR and ERA-40 with higher level kinematic terms, such the isallobaric wind component (equation 22; left hand term in brackets) inertial advective wind component (equation 22; right hand term in brackets), divergence (equation 25) of the ERA-40 wind field and inertial wind component were done.

$$\nabla \bullet V = (\partial V/\partial y + \partial U/\partial x) \quad (25)$$

Results from the investigation showed no consistent relationship between the higher level terms mentioned and speed, direction or vector differences between the AVHRR and ERA-40 wind fields. However for vorticity, a slight sign difference in wind speed difference was noticed between ridges and troughs. In troughs the AVHRR wind speed was slower than ERA-40 and faster than ERA-40 in ridges at upper, middle and lower levels. However, the differences were not significant and on average small in magnitude, with AVHRR being .06 m/s slower in troughs and .11 m/s faster in ridges at upper levels, .09 m/s slower in troughs and .06 m/s faster in ridges at mid levels, and .18 m/s slower in troughs and .03 m/s faster in ridges at low levels. The distribution of the speed and direction differences in troughs and ridges were close to Gaussian. However, if the value of relative vorticity was taken to be less than $-4 * 10^{-5}$ for a ridge or anticyclone, and greater than $4*10^{-5}$ to be in a trough or cyclone, the magnitude of the sign difference increases for the most part, especially in mid-level troughs. At upper levels, the average wind speed difference is 0.12 m/s slower in troughs and 0.13 m/s faster in ridges. Above 500 hPa in ridges, the frequency of larger speed differences greater than 3 m/s and faster (positive) are 54% and slower (negative value) are 46% (Figures 28a and b). In ridges, the percentages are the same, but are reverse in sign, with 54% of the larger differences being slower (negative), while 46% are faster (positive) as shown in Figures 28a and b. The sign of the difference is what is expected at mid and upper levels, if the magnitude of the ageostrophic wind is underestimated due to centripetal acceleration around the base of the ridge or the trough (Figure 16a). On the other hand, the small magnitude of the difference and Gaussian distribution at upper-levels is indication that even though there is some underestimation by ERA-40 of the ageostrophic wind component in troughs and ridges, it is not a common trend in the reanalysis. However, at mid-levels the average speed difference is 0.37 m/s slower in troughs, with the frequency of the larger slower speed differences (< 3 m/s) are 62%, and only 38% for larger faster speed differences (> 3 m/s) (Figure 29a). Indicating that an underestimation of the ageostrophic wind component in the ERA-40 reanalysis is more common during this case study. However, in ridges at mid-levels the average speed becomes insignificantly slower by .05 m/s (Figure 29b). At low levels, the average speed difference in troughs or cyclones is .45 m/s slower and .20 m/s faster in ridges or anticyclones. The frequency of larger slower speed differences in troughs is 61% and larger faster speed differences in ridges is only 39 % (Figures 30a and b).

Slightly more noticeable is that on average AVHRR is faster and more counter-clockwise in direction (negative value) than ERA-40 in the jet entrance regions and slower and more clockwise in direction (positive value) observed by AVHRR in the jet exit regions (Figures 27a-d) at upper levels. The average speed difference is - 0.13 m/s and direction difference is + 0.53 degrees in the jet exit region, with an average + 0.17 m/s speed difference and - 0.54 degrees direction difference in the jet entrance region. In comparison to all wind vectors outside the jet exit or jet entrance regions, the average speed difference is + .09 m/s and direction difference of 0 degrees. More significant is the average speed difference in the jet entrance region, direction difference and especially speed difference in the jet exit region at mid-levels (Figure 26a-c). The average direction difference in the jet exit region is + 1.06

degrees and - 0.29 degrees in jet entrance region, while the average speed difference in the jet entrance region is - 0.44 m/s and - 0.60 m/s in the jet exit region (Figures 26a-d). Compared to all other wind vectors at mid-levels the average speed difference is + .02 m/s and direction difference is + 0.18 degrees. Most significant is the larger frequency (< -3 m/s) of slower AVHRR wind speeds have compared to ERA-40 in the jet entrance and exit regions (Figures 26a and c). For an absolute magnitude of the wind speed difference greater than 3 m/s in the jet entrance region, for 71% of cases the AVHRR winds were slower than ERA-40 while in the other 29% of the cases AVHRR winds were faster than ERA-40. For the jet exit region, in 76% of the cases greater than 3 m/s absolute speed difference, AVHRR was slower than ERA-40, while faster in the other 24% of the cases. Also noticeable was that for direction differences greater than 15 degrees, in 63% of the cases the sign was positive (clockwise), while 37% was negative (counter-clockwise) in the jet exit regions at mid-levels. Overall, AVHRR wind vectors in the jet exit regions, especially at mid-levels, have a more rapid deceleration of the wind coming out of the jet on average. The AVHRR winds has a slower acceleration of the winds in the jet entrance region at mid-levels. Less significant, but of notice is the faster acceleration of the wind speed in the jet entrance region and greater deceleration of the wind speed in the jet exit region at upper levels. The AVHRR wind vectors are clockwise of ERA-40 wind vector on average in the jet exit region, especially at mid-level, and counter-clockwise of the ERA-40 wind vector on average in the jet entrance region at middle and upper levels. The noticeably more clockwise wind direction on average observed by AVHRR in the jet exit region at mid-levels is possible under-estimation of the cross isoheight flow in the jet exit region by ERA-40 (Figure 16b).

Dividing the jet entrance and exit regions into four quadrants indicate the same pattern of slower speeds indicated by AVHRR winds in the jet exit regions at both mid and upper levels and in the jet entrance region at mid-levels, and faster wind speeds at the upper-level jet entrance regions. At both mid and upper-levels, the left jet exit region has a more slower difference than the right jet exit region. Similar frequencies of the speed differences slower than 3 m/s occur in the left and right jet exit regions at mid levels and a slightly larger frequency (5%) of speed differences less than -3 m/s in the left jet exit than right jet exit region at upper levels. The average speed difference and frequency of speed differences greater than 3 m/s are similar in both left and right jet entrance regions, but are of opposite sign and larger magnitude at mid levels. The AVHRR winds are clockwise of the ERA-40 wind vector on average in the left jet exit region than right jet exit region. This is observed at both mid and upper-level jet exit regions. On the entrance side of the jet, compared to the right jet entrance region, the left jet entrance region AVHRR wind vectors are on average more counter-clockwise in direction than ERA-40 wind vectors.

Finally, when dividing cases at which the AVHRR wind speed were equal to or greater than 25 m/s, to those that were less than 25 m/s, a noticeable speed difference bias was observed. For AVHRR wind speeds greater than 25 m/s that typically occur in jet streaks, AVHRR winds were noticeably faster (Figures 25 a and b). At upper-levels AVHRR was on average 0.65 m/s faster in jet speeds. with 70% of the speed differences greater than 3 m/s were of positive sign (AVHRR faster than ERA-40) and only 30% of the speed differences greater than 3 m/s were slower than ERA-40. Meanwhile for wind speeds less than 25 m/s, AVHRR was 0.20 m/s slower than ERA-40, with larger speed differences (> 3 m/s) being 57% positive and 43% negative sign (Figure 25 c). Overall, the slower speed tendency of the AVHRR winds slower than 25 m/s is not as significant as seen in the jet speeds. In jet streaks AVHRR winds are .95 m/s faster than ERA-40, with 81% of the speed differences greater than 3 m/s being faster, while only 19% being slower. Also, at mid-levels, it was found that AVHRR was slightly slower in wind speeds less than 25 m/s, with an average speed difference of only -0.08 m/s and 53% of the larger differences being negative in sign compared to 47% positive in sign (Figure 24d). Again, the slower speed tendency of AVHRR in the slower wind speed condition (< 25 m/s) is not as significant as the faster speed tendency seen in stronger winds, especially at mid-levels. Overall, the noticeable faster speed difference of AVHRR compared to ERA-40 in jet speeds is possible indication that ERA-40 wind speeds in jet streaks are on average too slow.

a)

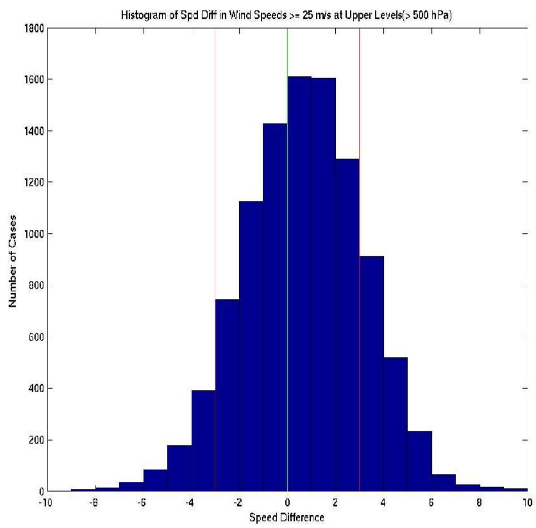

b)

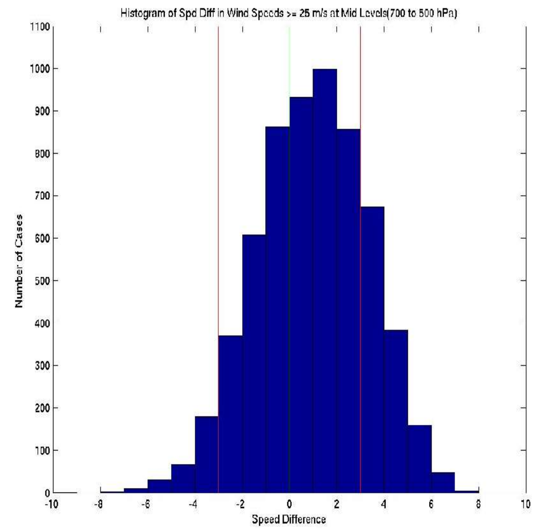

c)

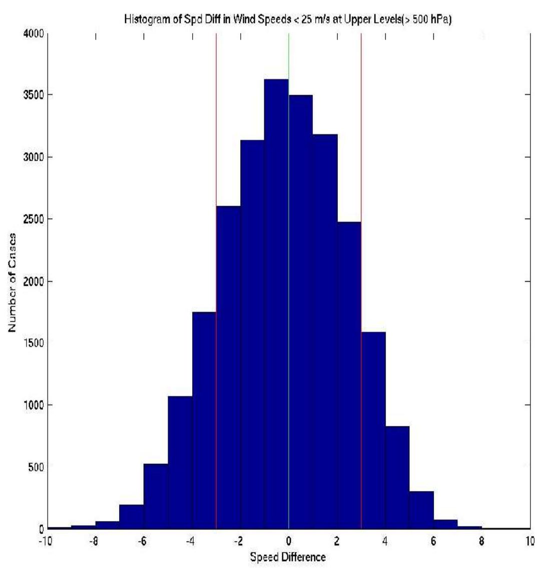

d)

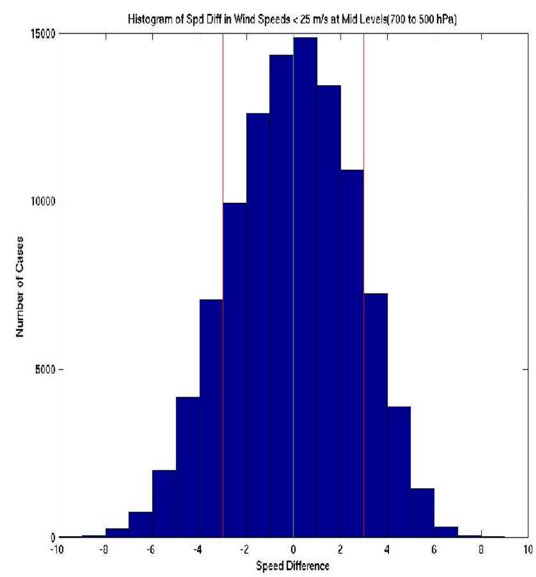

Figure 25. a) Histogram of the speed differences (AVHRR – ERA-40) at wind speeds >= 25 m/s at upper levels (above 500 hPa) . b) Histogram of the speed differences (AVHRR – ERA-40) in wind speeds >= 25 m/s at mid-levels (700 to 500 hPa). c) Histogram of speed differences (AVHRR – ERA-40) in speeds < 25 m/s at upper levels . d) Histogram plot of speed differences (AVHRR – ERA-40) in wind speeds < 25 m/s at mid-levels .

a)

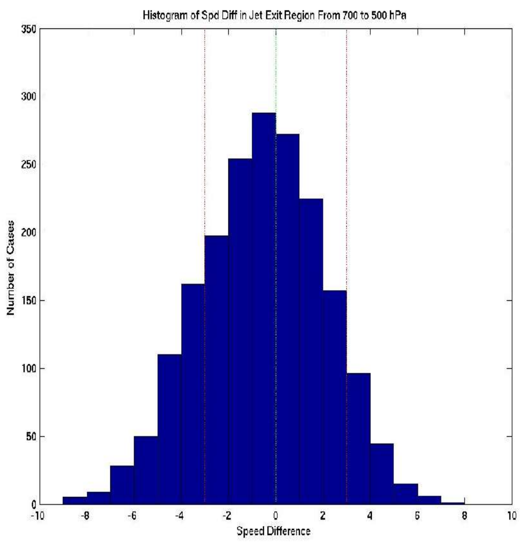

b)

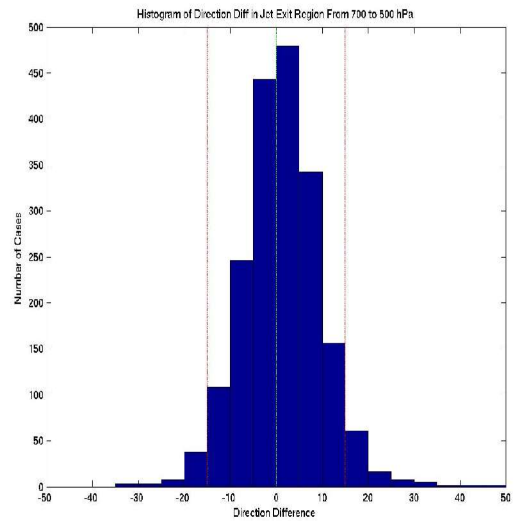

c)

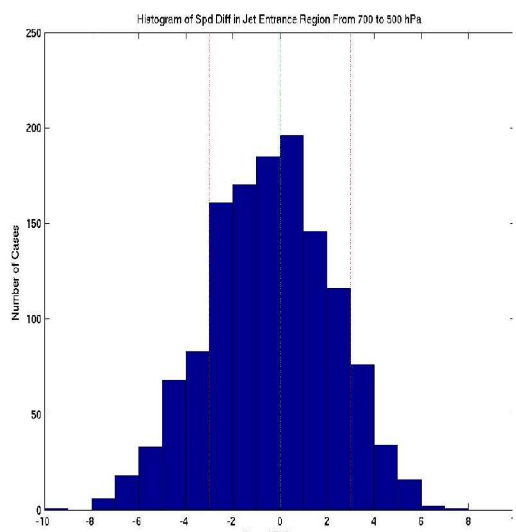

d)

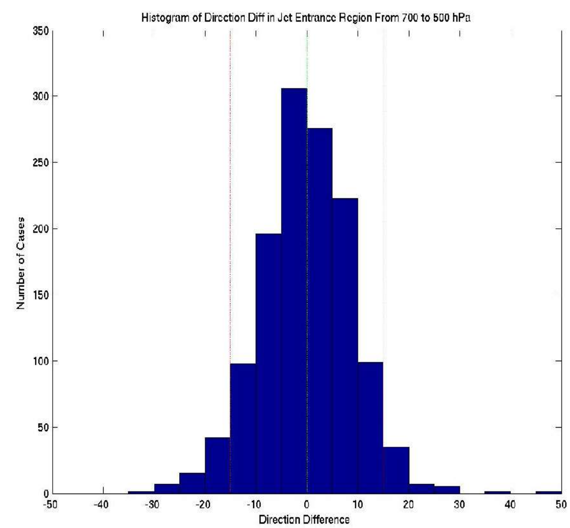

Figure 26. a) Histogram of speed differences (AVHRR – ERA-40) at mid-levels (700 to 500 hPa) in jet exit regions, defined as < -.35 m/s/km wind speed gradient along the isoheight. b) Histogram of direction differences (positive – clockwise of ERA-40 wind vector; negative – counter-clockwise of the ERA-40 wind vector) at mid-level jet exit regions. c) Histogram of speed differences at mid-level jet entrance regions, defined as > +.35 m/s/km wind speed gradient along the isoheight. d) Histogram plot of direction differences at mid-level jet entrance regions.

a)

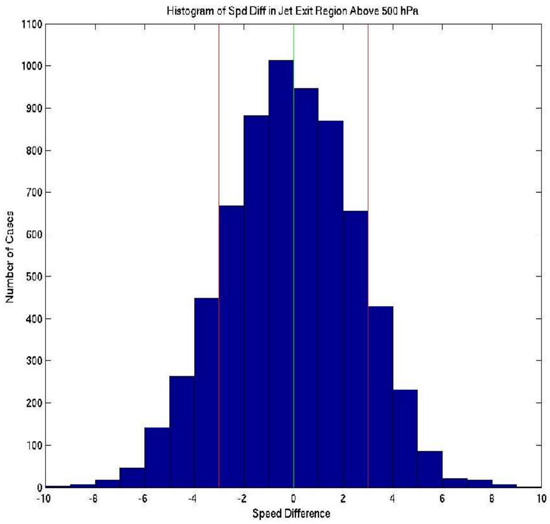

b)

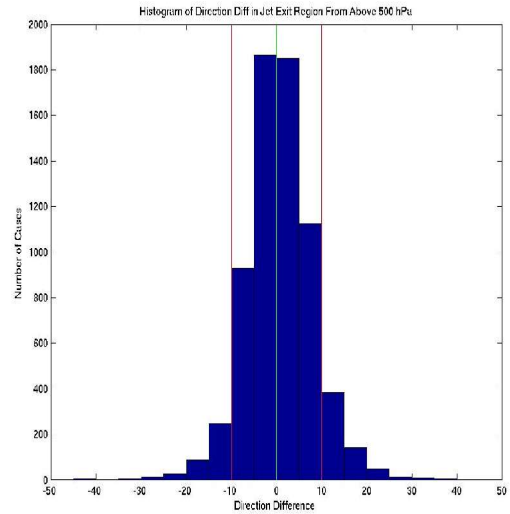

c)

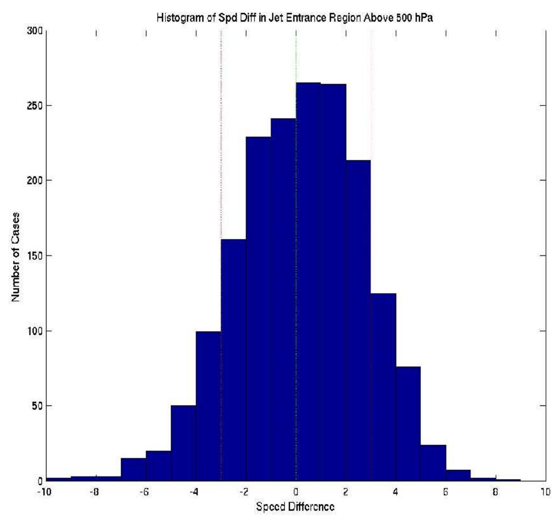

d)

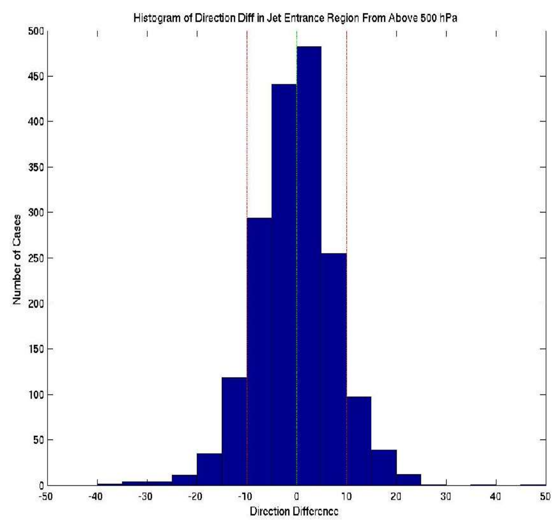

Figure 27. a) Histogram of speed differences (AVHRR-ERA-40) at upper levels (above 500 hPa) in jet exit regions, defined as < -.35 m/s/km wind speed gradient along the isoheight. b) Histogram of direction differences (positive – clockwise of the ERA-40 wind vector; negative – counter-clockwise of ERA-40 wind vector) at upper level jet exit regions. c) Histogram plot of speed difference at upper level jet entrance regions, defined as > +.35 m/s/km wind speed gradient along the isoheight. d) Histogram plot of direction difference at upper-level jet entrance regions.

a) b)

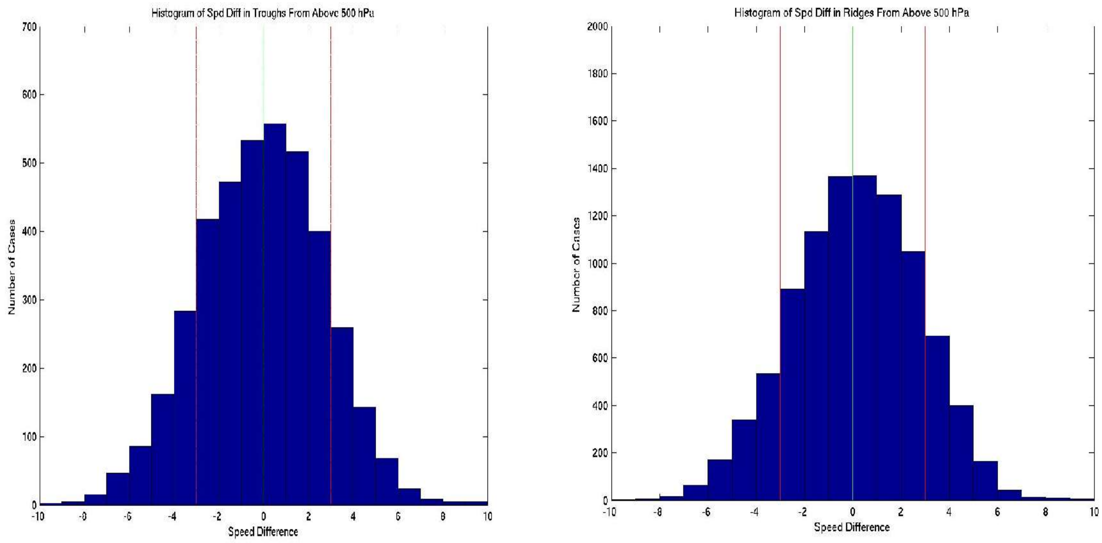

Figure 28. a) Histogram plot of speed differences (AVHRR – ERA-40) in troughs or cyclones (relative vorticity > + $4*10^{-5}$) at upper levels (above 500 hPa) b) Histogram plot of speed differences in ridges or anticyclones (relative vorticity < - $4*10^{-5}$) at upper levels.

a) b)

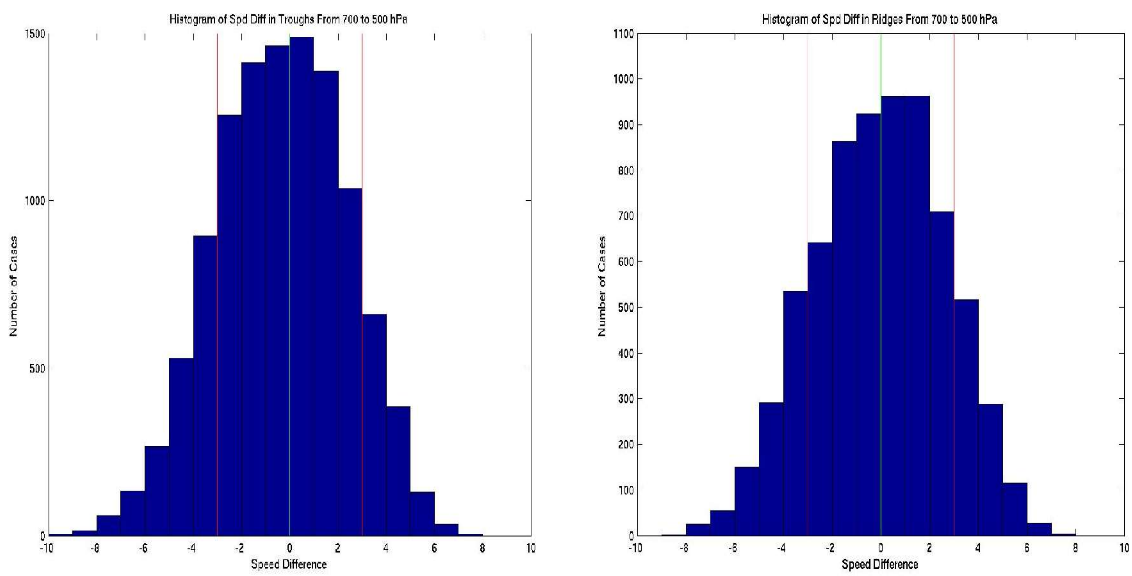

Figure 29. a) Histogram plot of speed differences (AVHRR – ERA-40) in troughs or cyclones (relative vorticity > $+4*10^{-5}$) at mid-levels (500 to 700 hPa) b) Histogram plot of speed differences in ridges or anticyclones (relative vorticity < $-4*10^{-5}$) at mid-levels.

a) b)

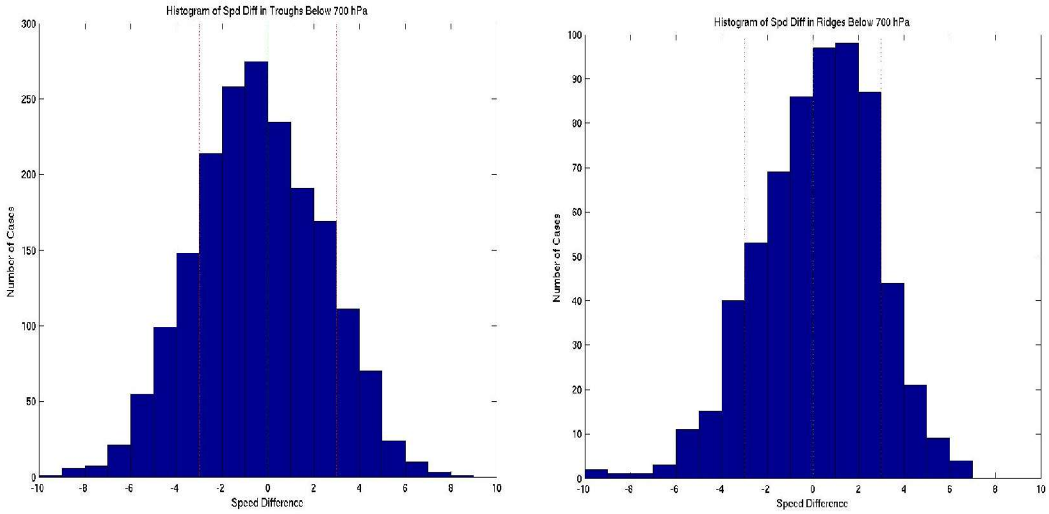

Figure 30. a) Histogram plot of speed differences (AVHRR – ERA-40) in troughs or cyclones (relative vorticity > $+4*10^{-5}$) at low-levels (Below 700 hPa) b) Histogram plot of speed differences in ridges or anticyclones (relative vorticity < $-4*10^{-5}$) at low-levels.

VIII. Summary and Conclusion

A forty-year history of tracking atmospheric motions using satellite imagery has led to the production of a 20 year dataset of winds over the polar regions. This dataset was derived by calculating the displacement of individual cloud features in the 11 μm infrared channel. Vigorous post-processing eliminates potentially bad wind vectors by checking the consistency of the satellite-derived wind vector in time, space and with the background wind field. This wind dataset was developed due to the observed errors in ERA-40 and NCEP/NCAR re-analysis products. Comparison of the ERA-40 and NCEP/NCAR wind vectors to winds data from rawinsonde not assimilated into the re-analysis indicates that there was a fast speed bias and a north and west direction bias in the re-analysis products. Errors in the wind field could cause jet streams to be overly intense due to gradients in the temperature and height field being too strong. Semi-permanent and fluctuating synoptic scale features in the re-analysis field could be misplaced and synoptic scale ageostrophic motions in the wind field could be underestimated. Moreover, studies that make use of re-analysis wind field could invalidate diagnostic conclusions drawn from it. For example, inaccurate values of advected quantities, such as moisture and energy, and inaccuracies in short-term and longer-term climate studies on circulation patterns over the Arctic and Antarctic.

The AVHRR sensor on board the NOAA polar orbiting satellites were used to develop the historical winds dataset. The dataset includes wind vectors over the Arctic and Antarctic from January 1, 1982 to August 31, 2002. Due to AVHRR lacking a water vapor and CO_2 channels, the only method used for determining the pressure height of wind vector is the Infrared Window Channel method. This method uses the brightness temperature of the cloud feature and compares it to the background field temperature sounding to come up with the pressure height where the temperature in the background sounding and brightness temperature are the same. The problem with this method is that it is prone to producing inaccurate height assignments in regions where there are temperature inversions or isothermal layers. The ERA-40 was used as the background field in post-processing checking and height determination of the CMV quality.

The ERA-40 is a collection of meteorological observations from 1957 to 2002, including the assimilation of atmospheric motion vectors derived from geostationary satellites. However, no polar winds from LEO satellites are assimilated into the re-analysis. With large regions of the Arctic and especially the Antarctic void of wind observations, the re-analysis is highly dependent on a assimilating model. If the assimilating model or other observations assimilated into the re-analysis that would be used to determine the wind (i.e., temperature and pressure) in data void regions had errors, any conclusions derived from them would be invalid.

Overall AVHRR and ERA-40 wind fields are on average similar with direction RMS values less than 20 degrees and speed RMS values less than 4 m/s. However, some individual case studies show distinct differences in speed and direction. On average, AVHRR is slower at low levels (below 700 hPa) and faster at upper levels (above 500 hPa). Validation of AVHRR winds compared to RAOBS show that the quality of the winds are better over the

Arctic than the Antarctic (Table 8a-c). However, AVHRR winds are of poor quality at low levels over the Antarctic, with large direction RMS of 70 degrees and fast speed bias of 8m/s, which maybe an indication of poor height assignments of the wind vectors due to low-level inversions that cause a higher level wind vector to be assigned too low a height, the background field (ERA-40) misplacing the top of the boundary layer or possibly tracking the wrong low-level cloud feature in consecutive images. On the other hand, of much better quality are the wind-vectors at mid and especially upper levels, where the speed bias and especially direction RMS are of lower magnitude (speed biases are 2 to 3 m/s smaller, and direction RMS that are 24 to 50 degrees smaller). Over the Arctic and Antarctic, the direction quality of the wind vector improves with height (Table 8a-c). In addition, the Normalized Root Mean Squared Error of the wind vectors decrease with height, indicating that the overall quality of the wind vectors increases with height (Table 8a-c). Over the Arctic the speed RMS increases with height, however, over the Antarctic the speed RMS decreases with height (Table 8a-c).

Validation of AVHRR and ERA-40 winds compared to rawinsondes not assimilated into the reanalysis from the LeadEx (1992) and CEAREX (1988-89) indicated that AVHRR had a smaller speed bias by over 1 m/s and RMS by 0.16 m/s, but larger direction bias by 0.12 degrees and RMS by 2 degrees. With the majority (99%) of the collocations coming below 400 hPa, it is indication that AVHRR has better quality in wind speed, but worse quality in wind direction at those experimental sites on average. Comparison of AVHRR to ERA-40 wind vectors near a RAOB launch location (within 1° X 1° lat/lon region) to those not located near a RAOB launch indicate that the RMSE and average absolute speed differences are larger when there are no RAOB data present (Table 11). This is also seen for RMSE and average absolute direction differences at middle and upper levels (Table 11). Thus, on average, larger speed and direction differences occur in areas void of radiosonde wind data, especially at upper levels, an indication that ERA-40 could be missing atmospheric flow data that AVHRR provides.

At low levels AVHRR wind vectors occur more frequently in flow around troughs. At mid-levels, there is a more of an equal chance to get wind vectors in a trough or ridge, however, in regions of larger relative vorticity ($> + 4 \times 10^{-5}$ or $< - 4 \times 10^{-5}$) there are more mid-level wind vectors that occur in troughs or cyclones (positive relative vorticity). In addition, AVHRR wind vectors occur more frequently in regions of Positive Vorticity Advection (PVA) or downstream of the trough and upstream of the ridge. This is expected as deeper and higher cloud tops tend to occur downstream of the trough in regions of PVA where upward vertical motion occurs and higher level clouds occur in flow over ridges out ahead of cyclones.

Most of the AVHRR wind vectors occur in the left jet exit region than right jet exit region. In addition, more AVHRR wind vectors occur in the right jet entrance than left jet entrance region at upper levels. In the left jet exit and right jet entrance regions, there is positive divergence and associated upward vertical motions that produces clouds for wind vectors to be generated.

In addition, individual case studies are investigated to look at possible re-occurring patterns in differences between AVHRR and ERA-40. The case studies show that larger differences occur in regions of flow curvature, and in amplified waves, with the larger differences sometimes located near regions of local maximum in the inertial advective term of the ageostrophic flow. A few examples of this are 18 Z June 8 to 0 Z June 9, 1995 (Figure 17) over north-central Russia in a left jet region into the base of a negatively tilted trough with cyclonic curvature, 06 Z May 10, 1992 (Figure 18) north of Novaya Zemlya over the Barents sea associated with a cyclonic curvature and June 18, 1995 at 12 and 18 UTC (Figure 21) in strong anticyclonic curvature around a ridge axis associated with a maximum in the IAT speed.

One possible explanation for differences between AVHRR and ERA-40 is an underestimation of the ageostrophic wind component in regions where strong or varying ageostrophic motions are expected. Unfortunately, comparison of the differences between AVHRR and ERA-40 with the magnitude of ageostrophic kinematic variables, such as the inertial advective term of the ageostrophic wind, the AVHRR ageostrophic component parallel to the geopotential height lines, the isallobaric term of the ageostrophic wind, divergence and vorticity of the ageostrophic wind component of wind field have not shown any significant relationship.

AVHRR is noticeably faster than ERA-40 in wind speeds greater than or equal to 25 m/s (jet streaks) with larger faster differences (> 3 m/s) being 40% more frequent at upper-levels (>500 hPa) and 62% more frequent at mid-levels (700 to 500 hPa). In addition, AVHRR derived winds are noticeably slower and more clockwise in the jet exit regions and slower in entrance regions at mid-levels. This could result from the ERA-40 underestimating the deceleration of the wind coming out of the jet streak and overestimating the acceleration of the wind coming into the jet at mid-levels, and possibly underestimated the ageostrophic flow across the isoheights in the mid-level jet exit region. At upper-levels, though not as significant as seen at mid-levels, the AVHRR wind vectors on average are slower and more clockwise of the ERA-40 wind vectors in the jet exit, however, are observed to be faster and counter-clockwise of the ERA-40 wind vectors in the jet entrance region. This could result from underestimation of the acceleration of the wind into the jet streak, deceleration of the wind out of the jet streak, and possible underestimation of the ageostrophic flow across the isoheights of the jet exit and entrance regions according to Figure 16b. However, excluding the underestimation of the deceleration of wind coming out of the jet exit at mid-levels, the biases in speed and direction are found to be relatively small.

When comparing regions of positive vorticity (troughs and cyclones) to regions of negative vorticity (ridges and anticyclones) it was found that AVHRR derived winds were slower on average by 0.06 to 0.18 m/s in regions of positive vorticity and faster in regions of negative vorticity by 0.03 to 0.11 m/s. This was found to be more noticeable when the relative vorticity threshold was increased to +/- 4 x 10^{-5}. However, with the slight exception of the slow bias of - 0.37 m/s in mid-level troughs, this is not found to be distinct. Furthermore, the obvious negative speed bias in troughs at mid-levels could be indication of underestimation by ERA-40 of the ageostrophic flow that opposes the geostrophic flow in troughs, slowing down the overall wind speed in flow around troughs. With opposing sign differences observed at upper-levels, with AVHRR derived winds being faster in anticyclonic flow and slower in cyclonic flow, is further indication of some underestimation of the ageostrophic flow in ridges and troughs, because unlike the ageostrophic flow in troughs, the ageostrophic component in anticyclones is in about the same direction as the geostrophic flow, increasing the overall wind speed in flow around ridges.

REFERENCES

Atlas, R., R. N. Hoffman, S. C. Bloom, J. C. Jusem, and J. Ardizzone. (1996) A Multiyear Global Surface Wind Velocity Dataset Using SSM/I Wind Observations. *Bulletin of the American Meteorological Society,* **77**, 5, 869-882.

Belchansky G. I., D. C. Douglas and N. G. Platonov. (2004) Duration of the Arctic Sea Ice Melt Season: Regional and Interannual Variability, 1979-2001. *Journal of Climate*, **17**, 1, 67-80.

Bluestein H. B. (1992) Synoptic-Dynamic Meteorology in Midlatitudes. 1st ed. Vol 1. New York, NY: Oxford University Press.

Comiso, J. C. (2002) A rapidly declining perennial sea ice cover in the Arctic. *Geophysical Research Letters*, **29**, 20, **17** 1-4.

Comiso, J. C. (2003) Warming Trends in the Arctic From Clear Sky Satellite Observations. *Journal of Climate,* **16** , 21, 3498-3510.

Deser, C., J. E. Walsh and M. S. Timlin. (2000) Arctic Sea Ice Variability in the Context of Recent Atmospheric Circulation Trends, **13**, 3, 617-633.

Dure, I., R. S. Vose and D. B. Wuertz. (2006) Overview of the Integrated Global Radiosonde Archive. *Journal of Climate,* **19,** 1, 53-68.

Francis, J. A. (2002) Validation of Reanalysis Upper-Level Winds in the Arctic with Independent Rawinsonde Data. *Geophysical Research Letters,* **29**, 9, 29-1-29-4.

Francis, J. A., E. Hunter, and C. Z. Zou. (2005) Arctic Tropospheric Winds Derived From TOVS Satellite Retrievals. *Journal of Climate,* **18,** 13, 2270-2285.

Fyfe, J. C. (2003) Extratropical Southern Hemisphere Cyclones: Harbingers of Climate Change? *Journal of Climate,* **16**, 17, 2802-2805.

Haimberger, L. (2005) Homogenization of radiosonde temperature time series using ERA-40 analysis feedback information, No. 23. *European Centre for Medium-Range Weather Forecasts*, Shinfield, Reading, UK (available from www.ecmwf.int/publications).

Hayden, C. M., and R. J. Purser. (1995) Recursive Filter Objective Analysis of Meteorological Fields: Applications to NESDIS Operational Processing. *Journal of Applied Meteorology,* **34**, 1, 3-15.

Herman, L. D., (1993) High Frequency Satellite Cloud Motion at high latitudes. *8th Symposium on Meteorological Observations and Instrumentation,* Anaheim, CA, Jan. 17-22, 1993, 465-468.

Herman, L. D. and F. W. Nagle. (1994) A comparison of POES satellite derived winds techniques in the Arctic at CIMSS. *7th Conference of Satellite Meteorology and Oceanography,* Monterey, CA, June 6-10, 1994, 444-447.

Holland, M. M. (2003) The North Atlantic Oscillation-Arctic Oscillation in the CCSM2 and Its Influence on Arctic Climate Variability. *Journal of Climate*, **16**, 16, 2767-2781.

Holmlund, K., (1998) The Utilization of Statistical Properties of Satellite-Derived Atmospheric Motion Vectors to Derive Quality Indicators. *Weather and Forecasting,* **13**, 4, 1093-1104.

Holmlund, K., C. S. Velden, and M. Rohn. (2001) Enhanced Automated Quality Control Applied to High-Density Satellite Winds. *Monthly Weather Review,* **129**, 3, 517-529.

Holton, James R. An Introduction to Dynamic Meteorology. 3rd ed. Vol. 48. San Diego, CA: Academic Press, 1992.

Jacobs, S. S., and J. C. Comiso. (1997) Climate Variability in the Amundsen and Bellinghausen Seas. *Journal of Climate,* **10**, 4, 697-709.

Kitchen, M., (1989) Representativeness errors for radiosonde observations. *Quarterly Journal Royal Meteorological Society,* **115**, 487 673-700.

Key, J. R., D. Santek, C. S. Velden, N. Bormann, J. Thepaut, L. P. Riishojgaard, Y. Zhu, and W. P. Menzel. (2003) Cloud-Drift and Water Vapor Winds in the Polar Regions From MODIS. *IEEE Transactions on Geoscience and Remote Sensing,* **41**, 2, 482-492.

Lindsay, R. W., and J. Zhang. (2005) The Thinning of Arctic Sea Ice, 1988-2003: Have We Passed a Tipping Point? *Journal of Climate,* **18**, 22 4879-4894.

Liu, Y., J. R. Key. (2003) Detection and Analysis of Clear-Sky, Low-Level Atmospheric Temperature Inversions with MODIS. *Journal of Atmospheric and Oceanic Technology,* **20**, 12 1727-1737.

Liu, Y., Key, J.R., A. Schweigler, and J. Francis. (2006) Characteristics of Satellite-Derived Clear Sky Atmospheric Temperature Inversion Strength in the Arctic, 1980-96. *Journal of Climate,* **19,** 19, 4902-4913.

Menzel, W. P. (2001) Cloud Tracking with Satellite Imagery: From the Pioneering Work of Ted Fujita to the Present. *Bulletin of the American Meteorological Society,* **82,** 1, 33-47.

Nieman, S. J., J. Schmetz, and W. P. Menzel. (1993) A Comparison of Several Techniques to Assign Heights to Cloud Tracers, *Journal of Applied Meteorology,* **32**, 9 1559-1568.

Nieman, S. J., W. P. Menzel, C. M. Hayden, D. Gray, S. T. Wanzong, C. S. Velden, and J. Daniels. (1997) Fully Automated Cloud-Drift Winds in NESDIS Operations. *Bulletin of the American Meteorological Society,* **78**, 6, 1121-1133.

Olander, Timothy L. UW-CIMSS Satellite-Derived Wind Algorithm User's Guide. (version 1.n) The Cooperative Institute for Meteorological Satellite Studies, Space Science and Engineering Center, University of Wisconsin-Madison, 1225 West Dayton Street, Madison, WI 53706. 2001.

Overland, J.E., M. Wang and N. A. Bond. (2002) Recent Temperature Changes in the Western Arctic during Spring. *Journal of Climate,* **15**, 13, 1702-1716.

Overpeck J., K. Hughen, D. Hardy, R. Bradley, R. Case, M. Douglas, B. Finney, K. Gajewski, G. Jacoby, A. Jennings, S. Lamoureux, A. Lasca, G. MacDonald, J. Moore, M. Retelle, S. Smith, A. Wolfe, G. Zielinski. (1997) Arctic Environment Change of the Last Four Centuries. *Science*, **278**, 5341, 1251-1256.

Parkinson C. L. and D. J. Cavalieri. (2002) A 21 year record of Arctic sea-ice extents and their regional, seasonal and monthly variability and trends. *Annals of Glaciology,* **34**, 441-446.

Polyakov, I. V., R. V. Bekryaev, G. V. Alekseev and U. S. Bhatt. (2003) Variability and Trends of Air Temperature and Pressure in the Maritime Arctic, 1875-2000. *Journal of Climate,* **16**, 12 2067-2077.

Rigor, I. G., J. M. Wallace, and R. L. Colony. (2002) Response of Sea Ice to the Arctic Oscilation. *Journal of Climate,* **15**, 18, 2648-2663.

Rigor, I. G., R. L. Colony, and S. Martin. (2000) Variations in Surface Air Temperature Observations in the Arctic, 1979-97. *Journal of Climate,* **13**, 5, 896-914.

Schmetz, J., K. Holmlund, J. Hoffman, B. Strauss, B. Mason, V. Geartner, A. Koch, L. Van De Berg. (1993) Operational Cloud-Motion Winds from Meteosat Infrared Images. *Journal of Applied Meteorology,* **32**, 7, 1206-1225.

Serreze, M. C., J. E. Walsh, F. S. Chapin III, T. Osterkamp , M. Dyurgerov, V. Romanovsky, W. C. Oechel, J. Morison, T. Zhang, and R. G. Barry. (2000) Observational Evidence of Recent Change in the Northern High-Latitude Environment. 1st ed. Vol. 46. The Netherlands: Kluwer Academic, 159-207.

Shapiro, M. A., P. J. Kennedy. (1981) Research Aircraft Measurements of Jet Stream Geostrophic and Ageostrophic Winds. *Journal of the Atmospheric Sciences,* **38**, 12, 2642-2652.

Thompson, D. W. J., and S. Solomon. (2002) Interpretation of Recent Southern Hemisphere Climate Change. *Science,* **296,** 5569, 895-899.

Tomassini, M., G. Kelly and R. Saunders. (1999) Use and Impact of Satellite Atmospheric Motion Winds on ECMWF Analyses and Forecasts. *Monthly Weather Review*, **127**, 6, 971-986.

Turner, J., and D. E. Warren. (1989) Cloud Track Winds in the Polar Regions From Sequences of AVHRR Images. *International Journal of Remote Sensing,* **10,** 4-5, 695-703.

Turner, J., T. A. Lachlan-Cope., S. Colwell, G. J. Marshall, and W. M. Connolley. (2006) Significant Warming of the Antarctic Winter Troposphere. *Science,* **311**, 5769, 1914-1917.

Uppala, S.M., Kållberg, P.W., Simmons, A.J., Andrae, U., da Costa Bechtold, V., Fiorino, M., Gibson, J.K., Haseler, J., Hernandez, A., Kelly, G.A., Li, X., Onogi, K., Saarinen, S., Sokka, N., Allan, R.P., Andersson, E., Arpe, K., Balmaseda, M.A., Beljaars, A.C.M., van de Berg, L., Bidlot, J., Bormann, N., Caires, S., Chevallier, F., Dethof, A., Dragosavac, M., Fisher, M., Fuentes, M., Hagemann, S., Hólm, E., Hoskins, B.J., Isaksen, L., Janssen, P.A.E.M., Jenne, R., McNally, A.P., Mahfouf, J.-F., Morcrette, J.-J., Rayner, N.A., Saunders, R.W., Simon, P., Sterl, A., Trenberth, K.E., Untch, A., Vasiljevic, D., Viterbo, P., and Woollen, J. (2005) The ERA-40 re-analysis. *Quarterly Journal of the Royal Meteorological Society*, **131**, 612, 2961-3012.

Vaughan, D. G., G. J. Marshall, W. M. Connolley, J. C. King, and R. Mulvaney. (2001) Devil in the Detail. *Science,* **293**, 5536, 1777-1779.

Velden, C. S., C. M. Hayden, S. J. Nieman, W. P. Menzel, S. Wanzong, and J. S. Goerss. (1997) Upper-Tropospheric Winds Derived From Geostationary Satellite Water Vapor Observations. *Bulletin of the American Meteorological Society,* **78**, 2, 173-195.

Velden, C., J. Daniels, D. Settner, D. Santek, J. Key, J. Dunion, K. Holmlund, G. Dengel, W. Bresky, and P. Menzel. (2005) Recent Innovations in Deriving Tropospheric Winds From Meteorological Satellites. *Bulletin of the American Meteorological Society,* **86**, 2, 205-223.

Walsh, J. E., W. L. Chapman, and T. L. Shy. (1996) Recent Decrease of Sea Level Pressure in the Central Arctic. *Journal of Climate,* **9**, 2, 480-486.

Wang, X. and J. R. Key. (2003) Recent Trends in Arctic Surface, Cloud, and Radiation Properties from Space. *Science,* **299**, 5613, 1725-1728.

Wang, X. and J. R. Key. (2005) Arctic Surface, Cloud and Radiation Properties Based on the AVHRR Polar Pathfinder Dataset Part I: Spatial and Temporal Characteristics. *Journal of Climate ,* **18,** 14, 2558-2574.

Wang, X. and J. R. Key. (2005) Arctic Surface, Cloud and Radiation Properties Based on the AVHRR Polar Pathfinder Dataset Part II: Recent Trends. *Journal of Climate ,* **18,** 14, 2575-2593.

Wexler, H. (1937) Formation of Polar Anticyclones. Monthly Weather Review, 64, 22, 229-235.

Zhang, X., J. E. Walsh, J. Zhang, U. S. Bhatt, and M. Ikeda. (2004) Climatology and Interannual Variability of Arctic Cyclone Activity: 1948-2002. *Journal of Climate* **17**, 12, 2300-2317.

Zou, C. Z., and M. L. Van Woert. (2002) Atmospheric Wind Retrievals from Satellite Soundings over the Middle- and High-Latitude Oceans. *Monthly Weather Review,* **130**, 7, 1771-1791.

Zou, C. Z. and M. L. Van Woert. (2001) The Role of Conservation of Mass in the Satellite-Derived Poleward Moisture Transport over the Southern Ocean. *Journal of Climate,* **14**, 6, 997-1015.